THEORETICAL ANALYSIS OF SOME CONTEMPORARY ISSUES ON WIRE-ARRAY Z-PINCH

by

Wilkin Tang

A dissertation submitted in partial fulfillment
of the requirements for the degree of
Doctor of Philosophy
(Nuclear Engineering and Radiological Sciences)
in The University of Michigan
2009

Doctoral Committee:

Professor Yue Ying Lau, Chairman
Professor Ronald M. Gilgenbach, Chairman
Associate Professor John E. Foster
Associate Professor Jamie D. Phillips
Adjunct Associate Professor John W. Luginsland

ACKNOWLEDGMENTS

First and foremost I would like to thank my advisor, Professor Y. Y. Lau. Without his guidance this thesis would not have been possible. Throughout my graduate studies, he has showed me how to attack difficult problems and get meaningful results. His insights and experiences are invaluable. He is also a great teacher from whom I learned a great deal from not just academically, but lessons in life as well. I am grateful to have him as my advisor.

I thank Professor Ronald Gilgenbach for his many useful classes on plasma physics, especially allowing me to teach the plasma laboratory course. The experience has allowed me to both learn how to run an experiment as well as acquire skills for teaching. His insights on how to conduct experiments are also invaluable, from my time spending with him, I learned how to interact and discuss problems with experimentalist. I thank all the professors who taught me throughout my college careers, from each of them I have obtained different skills that will help me succeed both professionally and personally.

I thank Dr. Edmund Yu from Sandia National Laboratories for his countless help on running the ALEGRA code, even though he was swamped with his own works, he still took time out of his busy schedule to help me out as much as he could. Without his help, the ALEGRA simulation part of the thesis would

not have seen the light of day. I would also like to thank all the people I worked with during the time I spent at Sandia National Laboratories. I especially like to thank Dr. Thomas Mehlhorn for all his support as well as giving me the opportunity to work at the Sandia National Laboratories throughout my graduate studies. The experiences allow me to see how top notch scientists conduct research at a professional setting. I would like to thank Dr. Carter Armstrong for giving me the opportunity to intern at L-3 Communications Electron Devices during the summer of 2004. I learned a great deal from that experiences as well as made some friends along the way. I would also like to thank Dr. Mark Kirshner, Dr. Craig Wilsen, Rosi Reed as well as all the people I have worked with at L-3 Communications Electron Devices for all their generous guidance, advices, and help.

To Dr. Phongphaeth Pengvanich (aka Duel), whose has been a great friend, it was a pleasure to have work with you throughout the years, and I hope all is well with you in Thailand. I would like to thank all the people I worked with at the Plasma Bay, I especially want to thank Dr. Trevor Strickler, Matt Gomez, Jacob Zier, David French and Brad Hoff for their experimental and Magic simulation help. It was a pleasure working with you all. I would like to thank all of the former students who have left Michigan who acted as my mentors. To Dr. Herman Bosman, Dr. Richard Kowalczyk and Dr. Fei He, thanks for all the guidance, you guys have taught me how to be a great theorist. I would also like to thank the current group of graduate students whom I have had the pleasure

to work with, I wish the best of luck to you all. I would like to thank Dr. John Luginsland, his delightful nature as well as insights and experiences on plasma physics have been invaluable. I hope to have the opportunity to work with you in the near future. I would like to thank all the administrative staff of the department for their support. Thanks for making the last six years a memorable joy.

I would especially like to thank Emily Luk (aka S.T.), my significant other. I am so lucky to have you in my life. I know the past two years have not been easy, but you still stick by my side, and never given up on me. I cannot ask for more than the love and patience that you have given me. Thanks for all your support throughout the years, without your encouragement and support, none of this would have been possible. Now the future awaits us, I hope we will journey it through together. I would finally like to thank all my friends and family. To mom, dad and my aunt, thanks for all the support throughout my life. To my big brother, Ricky, thanks for everything, and I wish you the best of luck in your thesis writing and defense in December. To my grandmother and grandfather, thanks for being there for me no matter what the circumstances are, I hope you guys can hear me in heaven. Without their support and understanding, I would not have made it through.

This research was supported by DOE/Sandia National Laboratories, AFOSR, AFOSR-MURI on Nanophysics of Cathodes and Breakdown, L-3 Communications, and Northrop Grumman.

TABLE OF CONTENTS

LIST OF TABLES

Table

LIST OF FIGURES

Figure

LIST OF APPENDICES

Appendix

ABSTRACT

The wire-array Z-pinch has generated the world's most intense X-ray pulses at Sandia National Laboratories. This thesis addresses two contemporary issues on wire-array Z-pinch: 1) Linear and nonlinear evolution of azimuthal clumping instabilities that exist in a discrete wire array, and 2) the problem of electrical contact resistance that strongly affects the current delivered to the Z-pinch load.

Presented first is the analytic theory on the linear and nonlinear evolution of the most unstable azimuthal clumping mode, known as the pi-mode, in a discrete wire array. In the pi-mode, neighboring wires of the array pair-up as a result of the mutual attraction of the wires which carry current in the same direction. The analytic solution displays two regimes, where the collective interactions of all wires dominate, versus where the interaction of the neighboring, single wire dominates. This solution was corroborated by two vastly different numerical codes which were used to simulate arrays with both high wire numbers (up to 600) and low wire number (8). All solutions show that azimuthal clumping of discrete wires occurs before appreciable radial motion of the wires. Thus, absence of azimuthal clumping of wires in comparison with the wires' radial motion may imply substantial lack of wire currents.

Another important recognition is that the complete account of the pi-mode, including the effects of corona may be expediently simulated by using only one single wire in an annular wedge with a reflection condition imposed on the wedge's boundary.

This thesis next presents a higher dimensional analytic theory on contact resistance. The electrical contact resistance is computed for a local constriction of finite length and finite transverse dimension in a conducting current channel. Conformal mapping is used for a rectangular current channel, and an electrostatic code is used for a cylindrical current channel. The connecting bridge, which models a local electrical contact, is assumed to be made of the same conducting material as the main current channel. Very simple analytic scaling laws for the contact resistance are constructed for a wide range of geometrical aspect ratios between the main current channel and its connecting bridge, which may assume rectangular shape (for Cartesian channel), and cylindrical or funnel shape (for cylindrical channel). These scaling laws have been confirmed by spot-checks with numerical code results within 1 percent. They are generalizations of the classical theory of Holm and Timsit on the contact resistance of the “a-spot”, defined as a small circular area of zero thickness through which current can flow.

CHAPTER 1

INTRODUCTION

The most intense X-ray pulses in the world, with X-ray yield in the MJ range and X-ray powers in the 100's of TW with energy conversion efficiency exceeding 15 percent, have been generated by wire Z-pinches and the Sandia Z-machine [Cun01, Cun05a, Cov01, Dee98, Mat05, Sin04, Spi98]. In virtually all Z-pinch experiments, ranging from low to high currents, and from low wire-number to high wire-number arrays, a host of hydromagnetic activities have been observed.

In this thesis we will examine some contemporary issues of Z-pinch. First, we will focus on the linear and nonlinear evolution of the azimuthal clumping instability in a wire array. This instability originates from the mutual attractions among wire filaments which carry currents in the same direction. The potential severity of this instability in discrete wire arrays was noted by Felber and Rostoker [Fel81], Samokhin [Sam88], and Hammer and Ryutov [Ham99b]. This instability was revealed in Strickler's simulations of a 300-wire array [Str03, Str05, Str06], where he randomly seeded perturbations in the wires' azimuthal positions and discovered that these random azimuthal perturbations indeed led to rapid clumping in the wire array. Strickler found that approximately after one e-fold time (the time interval in which the instability grow by a factor of e) these azimuthal perturbations grow essentially at the rate of the fastest growing mode, the π mode, in which two neighboring wires pair up (i.e., the azimuthal displacements of neighboring wires are 180 degrees out of phase with each). The azimuthal clumping

instability is the most violent and fastest growing instability in a discreet wire array. To focus on the azimuthal clumping instability, therefore, we concentrate in this thesis only on the π mode, the most unstable clumping mode in a discrete wire array.

This thesis will also address the important issue of electrical contact. This study is motivated by our ongoing studies of wire-array Z pinches [Gom08, Tan07, Zie08]. In the wire Z-pinch, the electrical contacts at the cathode end and the anode end of the wires affect the current delivered to the wire load [Dus07, Gom07, Gom08, San05, Zie08]. This in turn affects the Z-pinch plasma dynamics and has a significant influence on the X-ray yield for the Sandia Z-machine. In addition to wire-array Z pinches, electrical contact is also an important issue for wafer evaluation of manufactured integrated circuits [Car95], thin film resistors [Hall67], field emitters [Mil07], metal-insulator-vacuum junctions [Jor07], and high power microwave sources [Haw07, Lau07]. In cathodes that use carbon fibers [Shi05, Par06], how the fibers are bonded to the substrate has received increasing attention. Successful operation of high power microwave sources such as relativistic magnetrons depends crucially on good RF contacts [Haw07]. The problem of contact resistance is also important to terahertz sources, due to small circuit size [Boo07, Ppe07].

Section 1.1 gives the background and applications of Z-pinches. Brief summary of the novel results and the scope of this thesis are given in Section 1.2.

1.1 Introduction of Z-pinches

We will present a brief background and history of Z-pinch in Section 1.1.1. Section 1.1.2 will discuss a few scientific applications of Z-pinches.

1.1.1 Background and History of Z-pinch

A Z-pinch in its simplest form consists of a column of plasma with an electrical current running in the axial (z) direction. The axial electrical current produces an azimuthally directed magnetic field that results in a $\boldsymbol{J}\times\boldsymbol{B}$ Lorentz force that "pinches" the plasma radially inward, and thereby confining the plasma. Figure 1.1 illustrates one configuration of a Z-pinch.

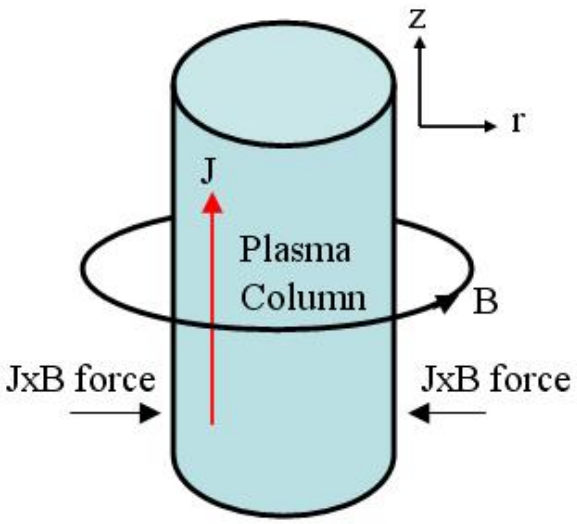

Fig. 1.1 **A schematic of Z-pinch showing the plasma column, the axial current, the azimuthally directed magnetic field, and the resulting $\boldsymbol{J}\times\boldsymbol{B}$ Lorentz force.**

W. H. Bennett attempted the first theoretical analysis of Z-pinch configuration in 1934 [Ben34]. Bennett considered a cylindrical column of fully ionized quasineutral plasma, with an axial current density, $\boldsymbol{J}$, produced by an axial electric field, and associated azimuthal magnetic field, $\boldsymbol{B}$. As the current flows through the plasma column, a magnetic field is created and the plasma column is pinched radially inward by the resulting $\boldsymbol{J}\times\boldsymbol{B}$ force. In the steady state with forces balancing,

$$\nabla p = \nabla\left(p_e + p_i\right) = \boldsymbol{J}\times\boldsymbol{B} \qquad \textbf{(1.1)}$$

where ∇p is the magnetic pressure gradient, p_e and p_i are the electron and ion pressures respectively. Using Ampere's Law $\nabla \times \boldsymbol{B} = \mu_0 \boldsymbol{J}$ and the ideal gas law $p = NkT$, the resulting equation is the well known Bennett relation [Ben34],

$$8\pi Nk\left(T_e + T_i\right) = \mu_0 I^2 \qquad \textbf{(1.2)}$$

where N is the number of electrons per unit length along the axis, T_e and T_i are the electron and ion temperatures, I is the total pinch current, and k is the Boltzmann constant.

Z-pinches may be divided into two classes, the highly dynamic z-pinches such as gas puff [Lev01, Lev02, Shi76] and cylindrical wire array [Cov01, Cun01, Cun02, Dee97, Dee98], and the other, includes the quasi-equilibrium self constricted plasma such as fiber pinches [Ham89]. For the fiber pinch [Ham89], Bennett-type pressure equilibrium [Ben34] was established by a deuterium plasma column at near solid density in a few nanoseconds, and to be maintained for a relatively long time. For a gas puff z pinch [Shi76], a plasma shell is formed from an annular gas puff and is compressed by the magnetic pressure. Bennett-type equilibrium is never reached. For a wire array z pinch, the whole array implodes toward the axis due to the global magnetic field, however, each wire itself also explodes.

High current pinches were studied in the 1950s which involved exploding wire that generated soft x-ray [Bur90]. Tens of kilovolts passed through a wire of 10-100μm in diameter. In the initial stage, the wire vaporizes, and the current decreases. As the electric field increases, breakdown takes place, and a plasma column with low resistance is created that is capable of carrying large amount of current, and the plasma pinches by

the resulting $\boldsymbol{J}\times\boldsymbol{B}$ force as discussed previously. The plasma electron density after pinching typically reaches $10^{21}\,cm^{-3}$, with plasma temperature reaching 10-100eV.

Early thermonuclear fusion research utilizes deuterium Z-pinch with high current in micro-seconds time scale. Equilibrium model of such Z-pinch plasmas suggested that fusion temperature and density can be reached with reasonable confinement time. Z-pinches of this type were greatly studied during 1952 to 1960 [Butt58, Tuc58]. However, it was found that such configuration of Z-pinch was inheritedly unstable. It was confirmed that the neutrons detected were not due to thermonuclear fusion but instead produced from violent instabilities [And58]. One of the first theoretical magnetohydrodynamic instabilities studies was done by Rosenbluth in 1956 [Ros56]. It was discovered that the instabilities could not be eliminated theoretically, or experimentally. As a result the fusion community lost interest in further investigation of Z-pinches, and for many years, the advancement of Z-pinches has stagnated. [Tokamak, also known as the toroidal Z-pinch operates in a very different regime, and the classical kink and sausage instability are far less severe for Tokamak.]

Due to the advancement of pulsed-power system, interest in Z-pinches revived during the mid-1970s. Very intense x-ray were observed by exploding a single wire in 1969 at the Naval Research Laboratory [Mos73, Spi01, Ste72, Vit71]. It was noted that the primary factor impeding a higher x-ray yield from exploding a single wire was due to the high initial impedance of the wire itself. This realization leads to the investigation and development of dynamic Z-pinch, and the result was the replacement of a single wire by a cylindrical array of wires, a cylindrical liner, or a cylindrical gas puff [Cov01, Cun05a, Dee97, Dee98, Lev02, San96, Shi76, Spi96, Spi98, Maz05, Meh03]. These configurations offer low initial impedance, and couple well with the low impedance,

high current generators, in experiments at Sandia National Laboratories [Spi89, Spi96, Spi97], Maxwell Laboratories [Mil81] and elsewhere, during the 1970s – 1980s.

Modern high density Z-pinch has been used as x-ray source in hohlraum, with x-ray energy in the MJ range. Recent experiments of cylindrical wire array using large number of wires (hundreds) have been performed at the Sandia National Laboratories [Dee97, Dee98, Maz05, San96, Spi 96, Spi98]. The experiments were performed on the Sandia's Z machine. Sandia has achieved dense, high temperature plasmas by firing fast, 100 nanosecond current pulses exceeding 20 million Amps. Studies by researchers at Sandia [Dee 97, San96, Spi89] suggest that modern cylindrical wire array Z-pinches with a large number of wires coupled with modern pulsed power technology are capable of much higher plasma compression, higher energy density, greater stability, higher plasma temperature and longer plasma confinement time as previously predicted. The relationship between the x-ray power generated and the number of wires used in the cylindrical array was studied extensive by T.W.L Sanford in 1996 as shown in Fig. 1.2 [San96], and more recently by M.G. Mazarakis [Maz05] as shown in Fig. 1.3.

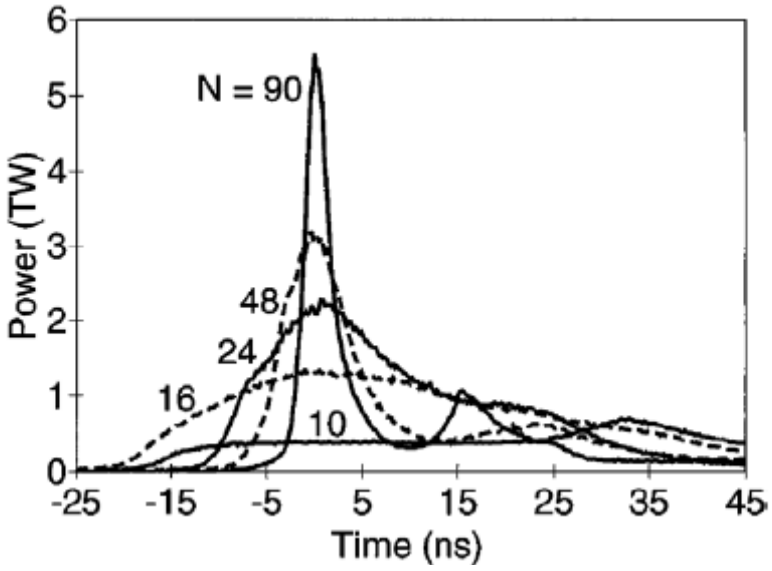

Fig. 1.2 **K-shell x-ray power versus time for different wire number (N) [from San96].**

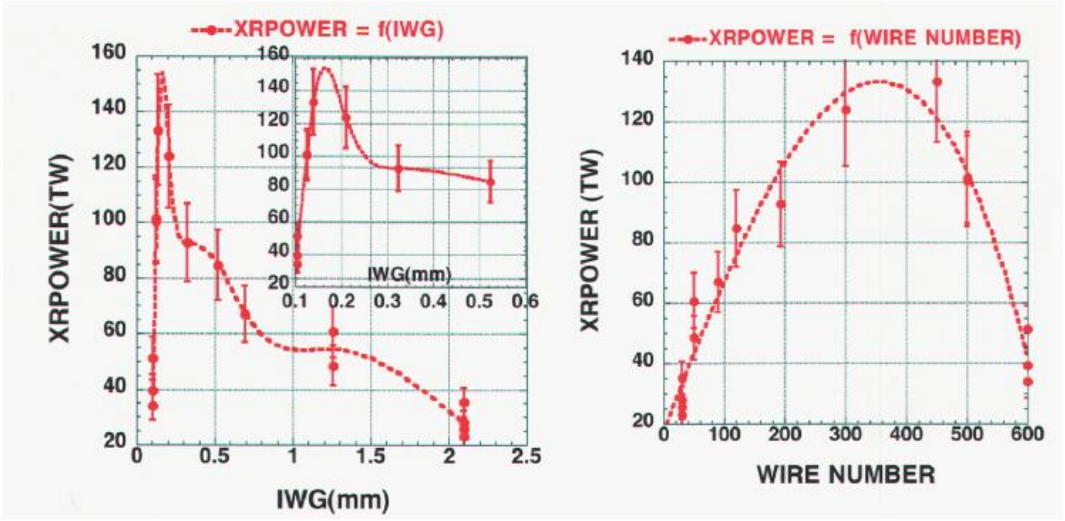

(a) (b)

Fig. 1.3 **(a) X-ray peak power as a function of Inter-Wire Gap. (b) X-ray peak power as a function of wire number in the array [from Maz05].**

In 1998, the Z machine produced a peak x-ray power of 280 TW in a 4ns (FWHM) pulse (x-ray energy of 1.8 MJ) by using a nested cylindrical wire array with 40mm outer array of 240 wires surrounding a 20mm inner array of 120 wires as shown in Fig. 1.4 [Dee98, Cun02]. The significant increase of x-ray power was thought to be due to the mitigation

of the Rayleigh- Taylor instability by the current switching from the outer to inner wire array, and the mass interpenetration between the outer and inner array [Bla03, Bra 96, Chi01, Cun05b, Cun06, Ter99].

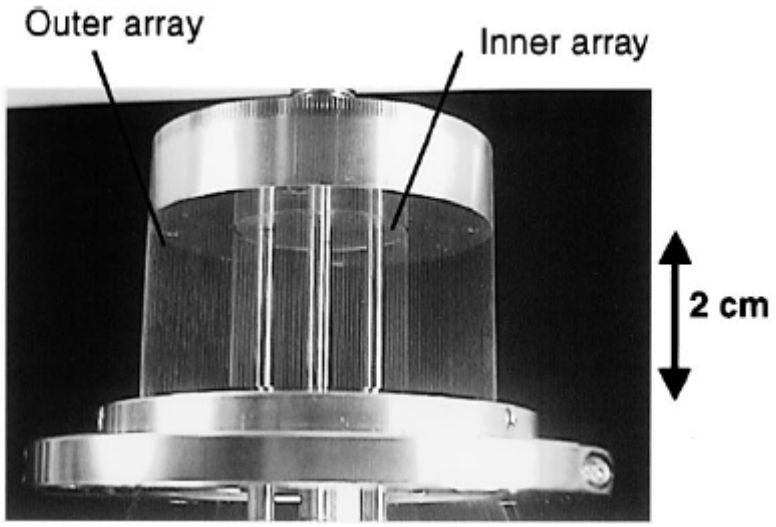

Fig. 1.4 A photograph shows a nested cylindrical wire array with 40mm outer array of 240 wires surrounding a 20mm inner array of 120 wires [from Dee98].

In order to increase the Z-pinch x-ray yield, the Z-machine at the Sandia National Laboratories has undergone an upgrade. The Z Refurbishment (ZR) project was completed in 2008 [Jon08, McD02, Wei07]. The new Z facility is capable of delivering 26 MA of current to produce a peak x-ray power of 350 TW, and peak x-ray energy of 2.7 MJ [Wei07, Jon08]. As a driver for the next generation of high power accelerator, Sandia National Laboratories is exploring the linear transformer driver (LTD) that was invented by researchers at the Institute of High Current Electronics in Tomsk, Russia; one such LTD was installed by R. Gilgenbach's group at U of Michigan [Gil08]. A LTD consists of an annular parallel connection of switches and capacitors designed to deliver rapid high power pulses. A photograph of LTD is shown in Fig. 1.5 [Gil08].

Fig. 1.5 A photography of UM 1-MA LTD with connection of switches and capacitors shown [from Gil08].

The LTD is capable of producing high current pulses, up to 1 MA, with a risetime of less than 100 ns. Traditional Marx generator requires pulse compression to achieve such fast risetimes. LTD is being seriously considered as a driver for z-pinch based inertial confinement fusion. A conceptual design by researchers at Sandia National Laboratories which employs a total of 210 LTD modules, is shown in Fig. 1.6 [Sty07].

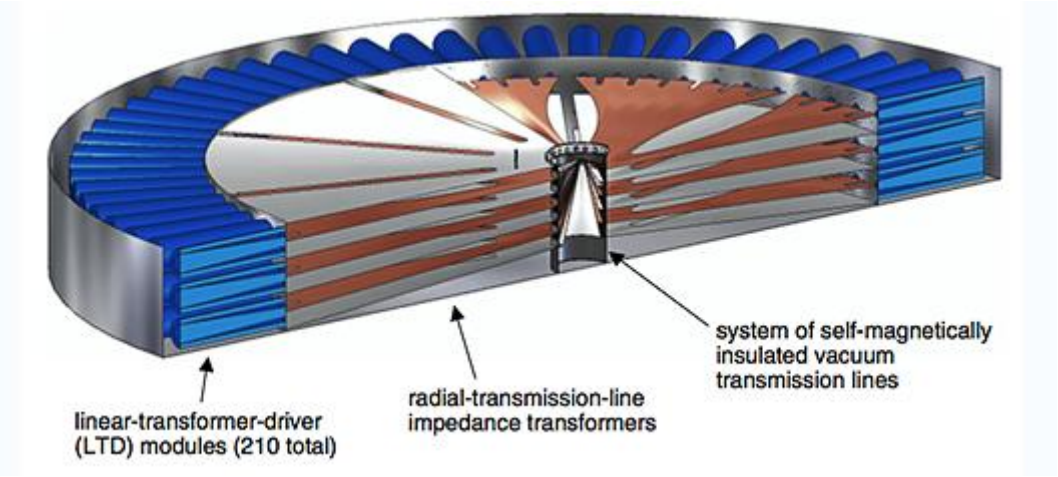

Fig. 1.6 A conceptual model of a 1 petawatt LTD-based z-pinch accelerator. The accelerator is 104 m in diameter and delivers a current of 70 MA. [from Sty07].

Currently, a 0.5MA LTD is being tested at Sandia at 10 Hz, and it has been fired 11, 000 times without flaw, according to a Sandia news release [Sin07]; a 1-MA LTD is constructed and operating at the University of Michigan [Gil08].

1.1.2 Applications of Z-pinch

In this section we will survey a few of the applications using Z-pinch as an x-ray source. This is not an exhaustive list. As the Z-pinch technologies advance, many more applications will become possible in the future [Mat97].

A. Controlled Thermonuclear Initial Confinement Fusion (ICF)

One application of Z-pinch is its use as an intense x-ray source for ICF application. X-ray yield in the MJ range and x-ray powers in the 100's of TW with energy conversion efficiency exceeding 15 percent, have been generated by wire Z-pinches at the Sandia National Laboratories. Two important concepts that use Z-pinch as an intense x-ray source to achieve fusion are the dynamic and double-ended hohlraum configuration.

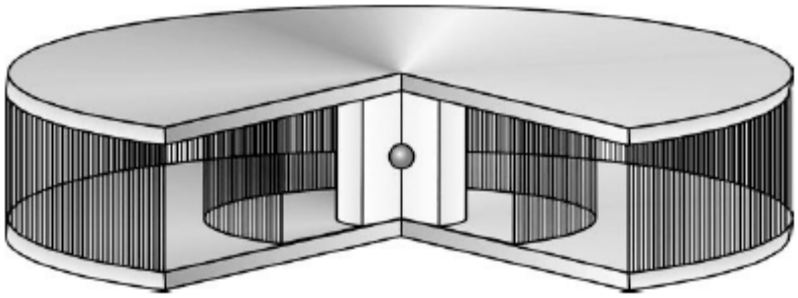

Figure 1.7 Dynamic hohlraum for fusion experiment. The figure shows a nested cylindrical wire array with a foam fusion target in the middle [from Meh03].

Figure 1.7 shows the configuration for a dynamic hohlraum fusion experiment. Two concentric wire arrays are used to form an imploding plasma shell. The impact of the imploding plasma with the low density foam launches a shock wave that heats the low density foam material, which then generates x-rays. The x-rays produced penetrate the low density material, and ablate the capsule within. The low density foam and the ablated material isolate the capsule surface from the hydrodynamics of the imploding plasma. As the wires ablate and implode, the resulting plasma shell also acts as a hohlraum that traps the x-ray generated. Hohlraum temperature as high as 220 eV, and thermonuclear D-D neutron yields of $2.6 \pm 1.3 \times 10^{10}$ have been observed [Bai04, Meh03, San02b]. This design is considered high risk, since the capsule symmetry is affected by both radiation asymmetries and the hydrodynamic coupling that can occur between the imploding Z-pinch plasma and the imploding capsule [Mat97].

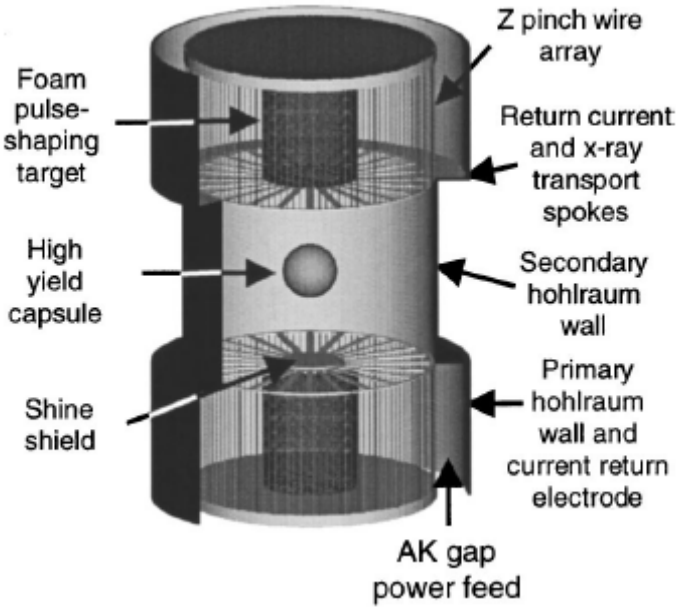

Figure 1.8 Configuration of a double-ended hohlraum for fusion experiment. Z-pinch wire arrays are located at the top and the bottom [from Meh03].

Figure 1.8 shows the configuration for a double hohlraum fusion experiment. In a double-ended hohlraum design, two Z-pinch loads are located at each end to provide x-ray flux to the ICF capsule located at the center [Fig. 1.8]. The Z-pinch can be imploded onto the foam shells, foam cylinders, or internal nested wire arrays to provide the necessary radiation pulse shaping [Cun01]. X-rays are transported into the secondary hohlraum through a beryllium radial spoke electrode and shine shield [Fig. 1.8]. The advantage of the double-ended hohlraum design is that it isolates the capsule from the pinch plasma, magnetic field, and direct x-ray shine [Cun01]. Capsule implosion with a hohlraum temperature of 70 ± 5 eV has been observed [Cun02]. Factors that limit the x-rays production include hydrodynamic Rayleigh-Taylor instabilities and cylindrical load asymmetry [Mat97], since even though the ICF capsule is isolated from the pinch plasma, the instabilities of the pinch plasma (e.g. Rayleigh-Taylor instabilities) can affect the system by preventing efficient radiation coupling into the ICF capsule hohlraum.

B. Materials' Equation of State Study

The intense thermal radiation generated in a dynamic Z-pinch hohlraum can be used to drive a shock wave through a sample. One such configuration is shown in Figure 1.9a,b.

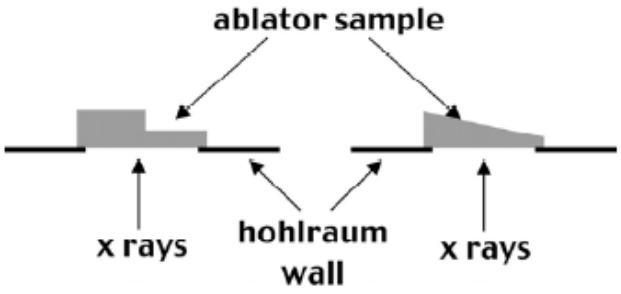

(a) **(b)**

Figure 1.9a,b Dynamic hohlraum configuration for Equation of State study. The x-rays of the hohlraum ablates the sample and sends a planar shock through the material. (a) Plane and (b) wedge shaped samples are shown in the figure [from Ryu00].

The x-rays generated by the dynamic hohlraum ablate the materials and drive a planar shock through the sample. A sample of ablator material is placed over a hole in the wall of a hohlraum [Fig. 1.9]. An x-ray flux inside the hohlraum is incident upon the sample. The ablator material will absorb most of the x-ray flux, and the resulting plasma will flow into the interior of the hohlraum [Ols97]. As a result, a strong shock will propagate in the opposite direction through the ablator material. If the sample is a step shape [Fig. 1.9a], the shock velocity can be determined by comparing the shock breakout times at the two step positions. If the sample is in the shape of a wedge [Fig. 1.9b], a time-resolved shock velocity can be obtained by measuring the shock breakout time as a function of position along the wedge.

The intense pressures built up by the shock wave in the sample can be used to study the equation of state of the sample material. Typical hohlraum temperature is at 100-150 eV, with shock pressure reaching as high as 10Mbar with 10 ns duration [Bai00, Ols97, Ryu00].

C. Production of Ultra High-Pulsed Magnetic Field

An external axial magnetic field can be compressed and entrained by radially imploding plasmas produced from gas-puff Z-pinches. Ultrahigh magnetic fields up to the order of 100 MG created by gas-puff Z-pinches has been proposed [Fel85, Fel88, Rud03]. Much higher repetition rate of high magnetic field pulses can be achieved by the gas-puff Z-pinch than by traditional chemical explosive flux compression technique [Her85, Rud03]. The interval between shots is determined only by the recovery time of the pulsed power system that is used to drive the Z-pinch. The production of ultrahigh magnetic fields of order of 100 MG or more could be important for studies of fundamental quantum electrodynamics effects that could not be observable otherwise. Other applications of ultrahigh magnetic fields include equation of state and material property studies, and conversion of high energy electrons to high energy gamma radiation [Fel85, Fel88, Rud03].

1.2 Novel Results and Scope of the Thesis

This thesis presents an analytic theory on the linear and nonlinear evolution of the most unstable azimuthal clumping mode, known as the pi-mode, in a discrete wire array. In the pi-mode, neighboring wires of the array pair-up as a result of the mutual attraction of the wires which carry current in the same direction. The analytic solution displays two regimes: (1) where the collective interaction involving all wires is important, and (2)

where the single wire interaction is dominant (i.e., one wire essentially experiences the attractive force due to its immediate neighbor).

In Chapter 2, the detailed analysis of the linear and nonlinear evolution of the most unstable azimuthal clumping mode is carried out. The theory is compared against the simulation results given by the ALEGRA code (for high wire number, e.g. 360 wires) that was developed by Sandia National Laboratories [Gar04]. In addition, the theory is also compared against the REIN code (for low wire number, e.g. 8 wires) developed by Strickler [Str03, Str05, Str06] for the impact time calculation. Impact time is defined as the time it takes the two wires to collide with one another. All solutions show that azimuthal clumping of discrete wires occurs before appreciable radial motion of the wires. Thus, absence of azimuthal clumping of wires in comparison with the wires' radial motion may imply substantial lack of wire currents [Str06].

This thesis also presents an analytic theory on the higher dimensional electrical contact resistance. The electrical contact resistance is computed for a local constriction of finite length and finite transverse dimension in a conducting current channel. Conformal mapping is used for the case of a rectangular channel. An analytic scaling law is constructed for the contact resistance over a wide range of aspect ratios between the constriction and the main current channel. The classical theory of Holm [Hol67] and Timsit [Tim99] is generalized for the first time in this thesis to include finite axial length effects of the "a-spot", defined as a small circular area of zero thickness through which current can flow.

In Chapter 3, we present the novel theory of higher dimensional (a small area of finite thickness through which current can flow between two contact members) electrical contact resistance. The detail of the conformal mapping, and the calculation for the zero-bridge length (ZBL) limit (a small area of zero thickness through which current can flow

between two contact members) is presented. When the bridge, or constriction, has a finite length, h, the analysis of contact resistance becomes significantly more complicated. The effect of finite h is found to increase the contact resistance linearly with h, by an amount that is expected from the increase in the current path length associated with finite h, and from the decrease in the cross-sectional area in the channel constriction. Scaling laws for various geometries of finite axial length, such as a cylindrical geometry or funnel shape geometry, are developed and compared with numerical simulations. A statistical theory of contact resistance, and a lumped element circuit model for electrical contact, are also presented.

The conclusion and suggestions for future work are given in Chapter 4.

CHAPTER 2

LINEAR AND NONLINEAR EVOLUTION OF AZIMUTHAL CLUMPING INSTABILITIES

In this chapter, we focus on the linear and nonlinear evolution of the azimuthal clumping instability [Tan07], which is the most violent instability in a discrete wire array. A cylindrical wire array is shown in Fig. 2.1.

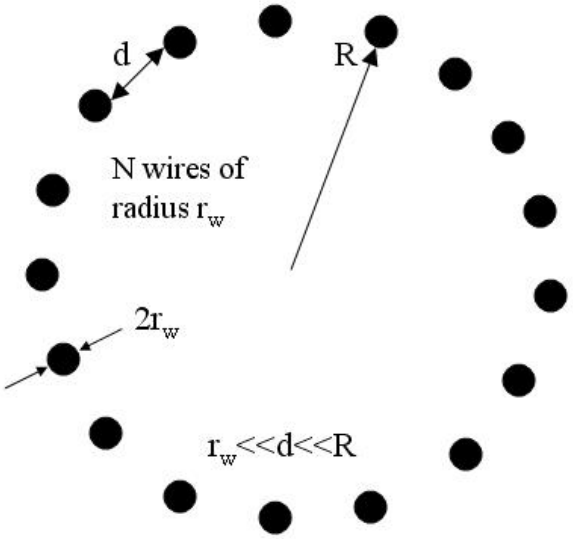

Fig. 2.1 A circular array of N wires. Each wire in the array carries a current in the z-direction, out of the plane of paper.

This instability originates from the mutual attractions among wire filaments which carry currents in the same direction. The potential severity of this instability in discrete wire arrays was noted by Felber and Rostoker [Fel81], Samokhin [Sam88], and Hammer and Ryutov [Ham99b] who found that the most unstable clumping mode is the π mode, in

which two neighboring wires pair up (i.e., the azimuthal displacements of neighboring wires are 180 degrees out of phase with each other in the π mode [Fig. 2.2]).

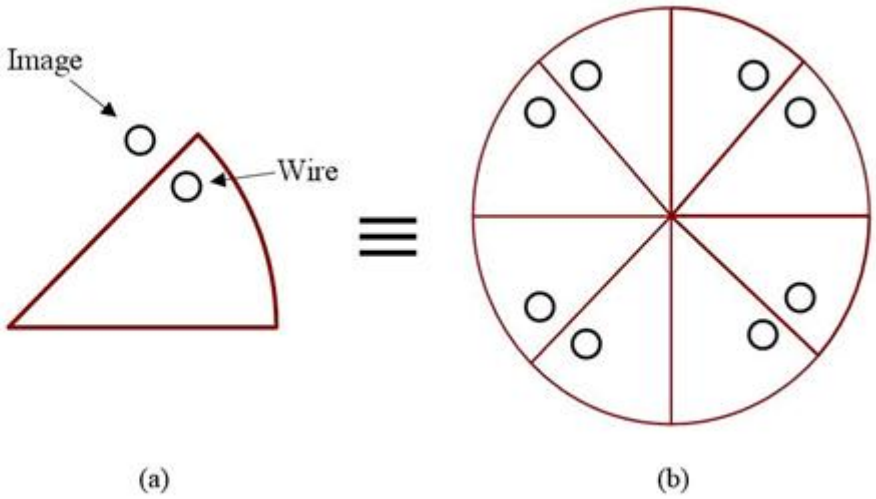

Fig.2 2. The one-sector wedge with reflection boundary condition (a), which replicates the π mode in an N-wire cylindrical array (b). Here, N=8.

This strong tendency toward clumping is entirely analogous to the Jeans instability of self-gravitating systems [Too64], with the gravitational attraction between matter being replaced by the mutual attraction of neighboring wires that carry currents in the same direction. This instability was revealed in Strickler's simulations of a 300-wire array [Str03, Str05, Str06], where random perturbations were seeded in the wires' azimuthal positions and he discovered that these random azimuthal perturbations indeed led to rapid clumping in the wire array. The analytic theory on the temporal evolution of the small signal growth in these randomly seeded perturbations was also presented [Str05]. It was found that approximately after one e-fold, these azimuthal perturbations grow essentially at the rate of the fastest growing mode, the π mode.

In contrast to the seeds of initial axial perturbations in wire arrays, there are natural candidates for the seeds of the initial azimuthal asymmetry. First, the azimuthal positions of the wires may have random variations, standard deviations of $\pm 21 \pm 4 \mu m$ have been reported [Cun01]. There is also azimuthal asymmetry caused by

the non-axisymmetric return current cans and viewing ports [San02]. Random azimuthal variations in the wire mass and in the current distribution among the wire currents have also been considered [Mos94]. These asymmetries may limit the compression ratio [Mos94], impose an optimal wire-number for x-ray yield [Cun05a, Gar04, Maz05, San01], and lead to the clumping instability that is the subject of this chapter [Fel81, Ham99b, Sam88, Str05].

To include random azimuthal perturbations in a 3-dimensional simulation of a high wire-number array is computationally prohibitive. To focus on the azimuthal clumping instability, therefore, we concentrate in this research only on the π mode, the most unstable clumping mode in a discrete wire array. The temporal evolution of the linear and nonlinear development of this mode is studied in detail analytically, and by simulation using two entirely different codes [Tan07].

2.1 Analytic Theory of Linear and Nonlinear Evolution of the π Mode

We shall construct the exact, closed form analytic solution for the linear and nonlinear development of the π mode up to the point where the wire pair coalesces for a Cartesian geometry. Consider first a circular array of N wires, each carrying a current I_w in the z-direction, arranged in a circle of radius R [Fig. 2.1]. We assume that the wire radius, r_w, is much smaller than the wire separation $d = 2\pi R/N$ and that the mass per unit length of the wire is m_L. In addition to $r_w << d << R$, we further assume that the backposts of the return current are sufficiently far away so that they have negligible effects on the dynamical evolution. Without any perturbation, this cylindrical array undergoes a radially inward acceleration g ($g > 0$) as a result of the global self magnetic field. For $N >> 1$,

$$g = \frac{\mu_0 I_w^2}{2dm_L}, \tag{2.1}$$

where μ_0 is the free space permeability, and m_L is the mass per unit length on a wire. In the Cartesian model, this array lies on the y-axis [Fig. 2.3]. (In the present analytic study, we prescribe the wire current, ignoring the changes due to the inductance effects. This assumption turns out to be adequate when compared with the results from the REIN code [Str03, Str05, Str06], which did include such inductive effects. See Table 2.1 below).

Since we are only considering the azimuthal clumping, we may consider a Cartesian array [Fig. 2.3]. There is a static equilibrium in such an infinite array [Fig. 2.3a].

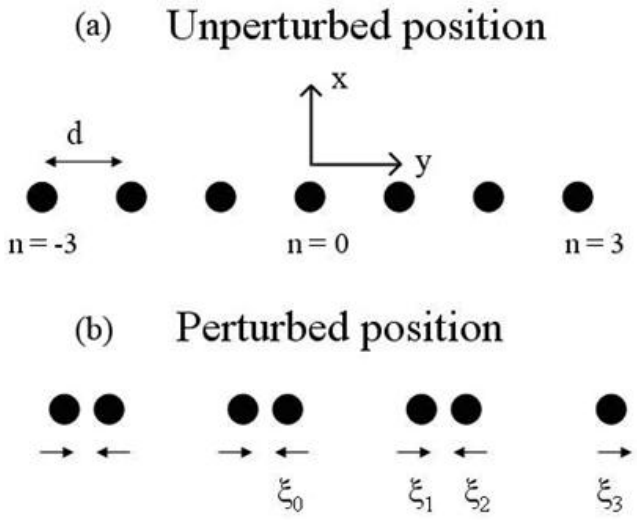

Fig. 2.3. (a) The unperturbed wire positions in a linear array, and (b) the perturbed wire positions in the presence of the π mode. Here, ξ_n is the displacement of the n-th wire from its unperturbed position.

In the unperturbed state, the wires have equal inter-wire separation. In a linear eigenmode formulation of perturbation, the azimuthal displacement (or y-directed displacement in the Cartesian model [Fig. 2.3]) from equilibrium of the n-th wire, $\xi_n(t)$, is related to that of the $(n+1)^{th}$ wire by the Floquet theorem,

$$\xi_{n+1} = \xi_n e^{-j\theta} \quad \Rightarrow \quad \xi_n = \xi_0 e^{-jn\theta} \tag{2.2}$$

Here, θ is an arbitrary constant for an infinite linear array. When $\theta = \pi$, the mode is called the π mode, and a pair of neighboring wire is displaced 180° out of phase with each [Fig. 2.3]. We shall focus on the π mode henceforth. We will show that the π mode is the most unstable mode in an infinite linear array in Appendix A. From Eq. (A9), we have $\frac{\gamma(\theta)}{\gamma(\pi)} = \sqrt{\frac{2\theta}{\pi}\left(1 - \frac{\theta}{2\pi}\right)}$, which is plotted in Fig. 2.4, where γ(θ) is the linear growth rate for the mode with a phase shift of θ between neighboring wires [c.f. Eq. (2.2)].

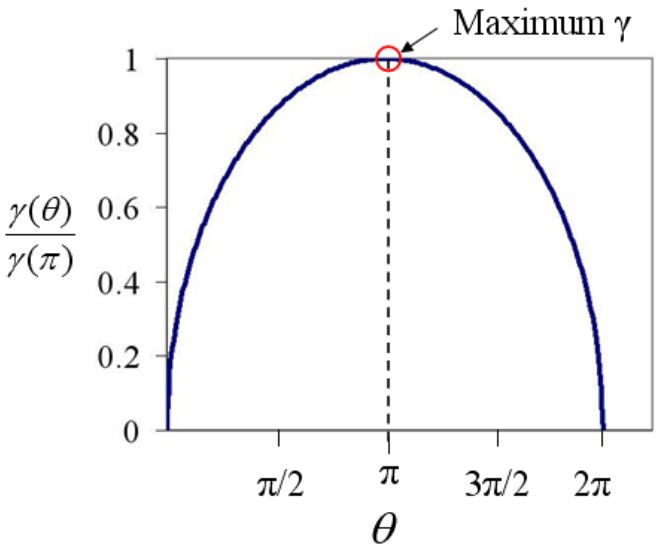

Fig. 2.4 Linear growth rate γ as a function of θ, normalized to that of the π-mode. The maximum linear growth rate occurs at $\theta = \pi$.

The linear and nonlinear evolution of the π mode is most conveniently carried out in an infinite linear array in which the y-direction represents the azimuthal direction [Fig. 2.3]. For convenience, we assume that there is no axial (z) variation nor axial displacement of the wires. Since in the Cartesian model, the x-directed (radial) motion is stable and is decoupled from the y-directed (azimuthal) motion, we assume that there is no radial (x) motion either. (The radial motion will be considered later in this Section).

Thus, we concentrate only on the y-directed (azimuthal) displacement of the zeroth wire, $\xi_0(t)$, of the π mode. The (x,y) coordinates of the n-th wire is (0, nd) in equilibrium, and is (0, nd+ξ_n) when the π mode is present [Fig. 2.3], where ξ_n is related to ξ_0 according to Eq. (2.3),

$$\xi_n = \xi_0 e^{-jn\pi} = (-1)^n \xi_0 \qquad \textbf{(2.3)}$$

This equation implies pairing up of neighboring wires for the π-mode perturbation [Fig. 2.3b].

The force on the zeroth wire is the sum of the attractive forces from all other wires, each carrying a current in the same direction. This resultant force leads to the following equation of motion for $\xi_0(t)$,

$$\ddot{\xi}_0 = \gamma_p^2 \left(\frac{d}{\pi}\right) \tan\left(\frac{\pi\xi_0}{d}\right) , \qquad \textbf{(2.4)}$$

$$\gamma_p = \gamma(\pi) = \sqrt{\frac{\pi g}{2d}} , \qquad \textbf{(2.5)}$$

where the dot denotes a time derivative and γ_p is the linear growth rate of the π mode [Str05]. Equation (2.4) is exact and its derivation is given in Appendix B [cf. Eq. (B2)].

Equation (2.4) displays the linear and nonlinear growth of the clumping instability. When the azimuthal displacement is small, ξ_0 approaches zero, and Eq. (2.4) may be approximated by

$$\ddot{\xi}_0 \cong \gamma_p^2 \xi_0, \quad (\xi_0 \to 0) , \qquad \textbf{(2.6)}$$

which is the governing equation for the small signal growth rate of the π mode [Ham99b, Sam88, Str05]. When ξ_0 approaches d/2, that is, when a pair of neighboring wires is about to touch each other [Fig. 2.3b], the mutual attraction between this wire pair becomes arbitrarily large in this idealized model, and the RHS of Eq. (2.4) tends to

infinity. In the latter limit, we may use the expression,

$\tan x = \sin x/\cos x = \cos(\pi/2 - x)/\sin(\pi/2 - x) \cong 1/(\pi/2 - x)$ as x approaches π/2, to approximate Eq. (2.4) as

$$\ddot{\xi}_0 \cong \gamma_p^2 \left(\frac{d}{\pi}\right)^2 \frac{1}{(d/2 - \xi_0)}, \qquad (\xi_0 \to d/2)\ , \tag{2.7}$$

which clearly shows strong mutual attraction between the two coalescing wires, to the exclusion of all others. The transition from Eq. (2.6) to Eq. (2.7) is shown in Fig. 2.5, which plots the RHS of Eq. (2.4), the wire's y-directed acceleration versus its displacement in the π mode.

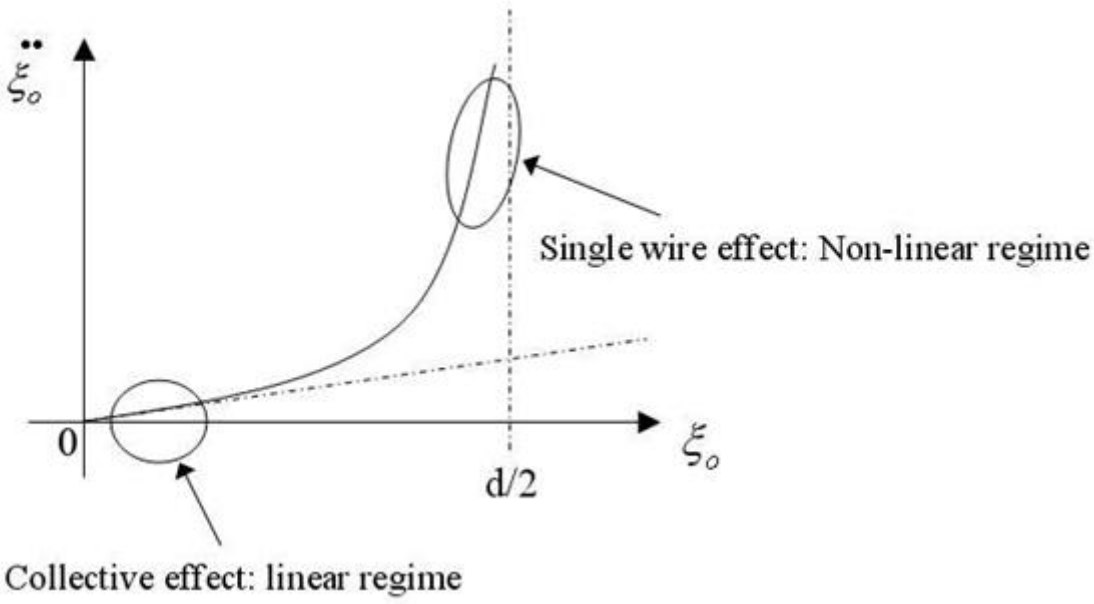

Fig. 2.5. Acceleration vs. displacement of the zeroth wire in the π mode.

Interestingly, the above idealized model of the π mode displays both the collective effects of many wires and the single wire effects [Fig. 2.5]. The collective effects are dominant when the azimuthal displacement is small, in which case the linear *eigenmode* equation [Eq. (2.6)] results from the collective interaction among *all* wires. The single

wire effect is dominant when the wire pair is about to touch, as is evident from Eq. (2.7). Equation (2.7) may in fact be derived under the assumption of only 2 wires in the system. Thus, the collective versus single wire effect may be studied by adjusting the wire displacements relative to the average wire separation. Roughly speaking, the single wire effect becomes dominant when ξ_0 moves beyond about 50% of the half wire-spacing (d/2), when the tangent factor in Eq. (2.4) becomes unity. For a cylindrical array, this may be studied by varying the wire number, which can be equivalently studied in the one-sector simulation by varying the wedge angle in Fig. 2.2a; and by varying the initial perturbation in the π mode.

The general initial conditions are imposed: $\xi_0(0) = \xi_i, \dot{\xi}_0(0) = \upsilon_i$, where ξ_i and v_i are respectively the zeroth wire's initial azimuthal displacement and azimuthal velocity. The solution to Eq. (2.4) is then most conveniently represented in terms of the dimensionless variables, $\tau = \gamma_p t$, $f(\tau) = \pi\xi_0/d$. In these normalized variables, the governing equation (2.4) and the associated initial conditions then read,

$$\frac{d^2 f(\tau)}{d\tau^2} = \tan f(\tau) \ , \tag{2.8}$$

$$f(0) \equiv f_i = \pi\xi_i / d, \qquad df / d\tau\big|_{\tau=0} \equiv u_i = \pi v_i /(d\gamma_p) \ . \tag{2.9}$$

It is shown in Appendix B that the solution to Eqs. (2.8) and (2.9), $f = f(\tau)$, whose inverse, $\tau = \tau(f)$, may be written as [cf. Eq. (B7)],

$$\tau(f) = \int_{f_i}^{f} dy \left[u_i^2 - 2\ell n\left(\frac{\cos y}{\cos f_i} \right) \right]^{-1/2} . \tag{2.10}$$

Equation (2.10) is the exact solution to Eq. (2.8). It governs the linear and nonlinear evolution of the π mode in an infinite linear array of infinitesimally thin wires. It

depends on the initial wire displacement (f_i) in the π mode, as well as the initial velocity (u_i), which may be taken to be zero in most cases. It is also the approximate solution even if the wire current (I_w) is time-varying, in which case τ is given by Eq.(B4) of Appendix B.

The linear, collective regime corresponds to f approaching zero, in which case the solution Eq. (2.10) is approximately given by

$$f(\tau) \cong f_i \cosh\tau + u_i \sinh\tau, \qquad (f << 1). \tag{2.11}$$

Equation (2.11) is more readily deduced from Eq. (2.8), under the assumption f << 1, along with the initial condition Eq. (2.9). The nonlinear, single wire regime corresponds to f approaching $\pi/2$.

Merging of a pair of wires occurs when $f = \pi/2$ from the RHS of Eq. (2.8), or equivalently, $\xi_0 = d/2$ in Fig. 2.5. Thus, from Eq. (2.10), the normalized time, τ_m, it takes for a pair of wire to merge in this π mode is simply

$$\tau_m = \tau(\pi/2) = \int_{f_i}^{\pi/2} dy \left[u_i^2 - 2\ell n\left(\frac{\cos y}{\cos f_i}\right)\right]^{-1/2}, \tag{2.12}$$

whose values depend only on the initial conditions, u_i and f_i. Figure 2.6 shows τ_m as a function of f_i for the usual case $u_i = 0$. Also shown in Fig. 2.6 are the asymptotic expansions for τ_m for the limiting case $f_i << 1$ and $f_i \sim \pi/2$,

$$\tau_m \cong \ell n(1/f_i) + 1.04, \qquad f_i << 1, \tag{2.13}$$

$$\tau_m \cong \sqrt{\frac{\pi}{2}}\left(\frac{\pi}{2} - f_i\right), \qquad f_i \to \frac{\pi}{2}. \tag{2.14}$$

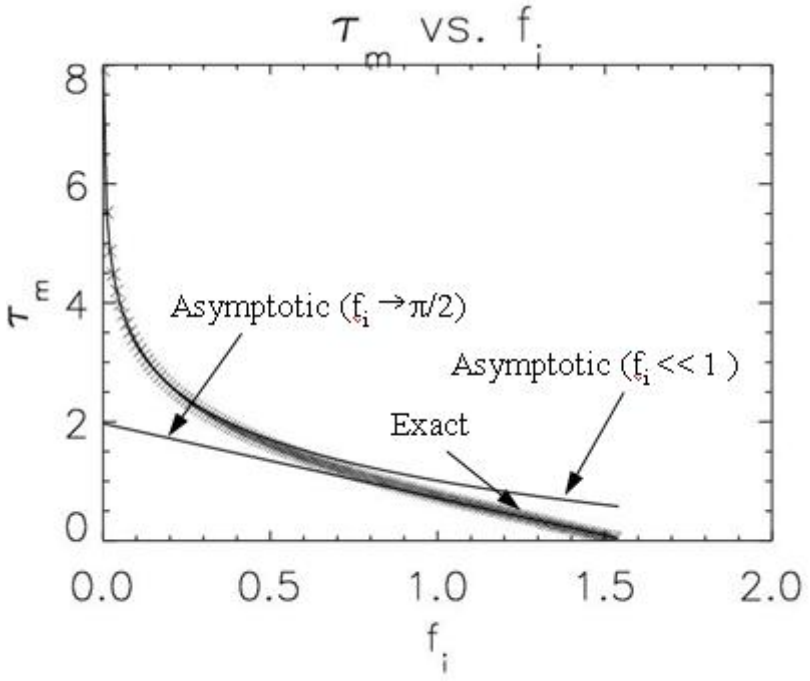

Fig. 2.6. Normalized impact time (τ_m) vs. initial azimuthal displacement (f_i) of the zeroth wire in the π mode. Also shown are the asymptotic formulas for $f_i << 1$ [Eq. (2.13)] and f_i approaching π/2 [Eq. (2.14)].

The derivation of Eqs. (2.13) and (2.14) is given in Appendix C [cf. Eqs. (C6), (C11)]. Equation (2.13) shows that if the initial perturbation displacement is small (f_i approaches zero), it takes a logarithmically long time for the wire pair to clump together. Equation (2.14) gives quantitatively the short time scale for wire merging if the wire pair is already close to each other in the π mode [Fig. 2.2b].

In the cylindrical geometry [Fig. 2.1], the wires would move radially inward as they clump azimuthally, as a result of the global magnetic field of the array. The radial displacement of the zeroth wire from its initial radius, denoted by Δr, is related to its azimuthal displacement on the wire trajectory. In terms of the normalized azimuthal and radial displacements, $f = \pi\xi_0/d$ and Δρ = πΔr/d, this trajectory takes the simple form,

$$\Delta\rho = -\tau^2(f) \ . \qquad \textbf{(2.15)}$$

where $\tau(f)$ is given by Eq. (2.10). The negative sign in Eq. (2.15) accounts for the wire's inward radial motion. The derivation of Eqs. (2.15) is given in Appendix C [cf. Eq. (C3)]. The total normalized inward radial displacement, from the initial position up to the time (τ_m) when the wire pair merges, is then given by $\Delta\rho_m = -\tau_m^2$ according to Eqs. (2.15) and (2.12). Note that this expression, and Eq. (2.15) in general, is independent of the current, and the current pulse shape.

The analytic theory, Eqs. (2.10), (2.12), and (2.15), will be compared with the ALEGRA simulations [Gar04] and with the REIN circuit model simulations [Str03, Str06] in the next section.

2.2 Simulations

The analytic solution given in Section 2.1 was corroborated by the two vastly different simulation codes, ALEGRA, developed at the Sandia National Laboratories [Gar04], and the resistive-inductive wire circuit code (REIN), developed at the University of Michigan [Str03, Str06]. These two codes were respectively used to analyze both the high wire-number (up to N = 600) and the low wire-number arrays (N = 8) where N is the number of wires in the array. In this section, we show simulation results using the ALEGRA code [Gar04] for high wire-number arrays (N in the hundreds), and using the REIN code for a low wire-number array (N = 8). Both codes treat a cylindrical array. We find good agreement between both code results and the analytic theory developed in the previous section.

2.2.1. ALEGRA Simulation Results

ALEGRA-HEDP is a multi-physics simulations code developed at the Sandia National Laboratories [Gar04]. It uses an Arbitrary-Lagrangian-Eulerian (ALE) operator split algorithm to solve the resistive magneto-hydrodynamic equations, as well as radiation and thermal transport. Material motions can be tracked through a Lagrangian or an Eulerian mesh. For the simulations of the π mode clumping instability, we use an Eulerian mesh. A Lagrangian tracer particle is used to track the wire position as a function of time. A wedge shape domain is used with reflective boundary conditions in the azimuthal direction [Fig. 2.2a]. The reflective boundary condition automatically filters out all other modes except the π mode. Changing the angle of the wedge is equivalent to changing the number of wires in the array. We run a 2D-xy simulation, without coronal plasmas, ignoring joule heating, radiation transport, and thermal conduction for a fair comparison with the theory. Aluminum wires of 10 μm radius in a 1 cm radius cylindrical array are simulated with an initial perturbation of 30 μm off the bisector of the wedge, i.e., $\xi_0(0) = \xi_i = 30$ μm [Fig. 2.7].

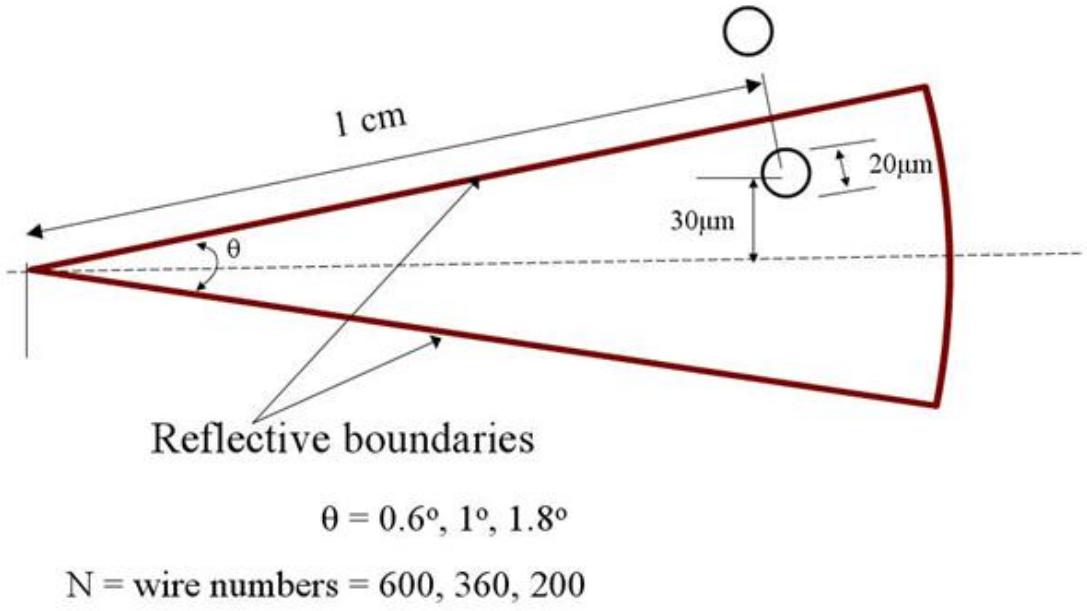

Fig. 2.7. ALEGRA simulation geometry.

The simulations are run with different sector angle θ, (1.8^o, 1^o, 0.6^o) which represents different wire numbers in the wire arrays (200 wires, 360 wires, and 600 wires). The total line mass is 1.69 mg/cm for the 200-wire array, 3.05 mg/cm for the 360-wire array, and 5.09 mg/cm for the 600-wire array. The total current is 3.8 MA (200 wires), 6.84 MA (360 wires) and 11.4 MA (600 wires), which corresponds to 19 kA of current per wire for all three cases, the rise time for the current pulse is 1ns. The material models used for this study are as follows: equations of state - SESAME 3700 [Ker87]; conductivities - Lee-Moore-Desjarlias Model [Des01, Lee84] for Aluminum; material strength - Elastic Plastic. The input decks for the simulations are given in Appendix D.

In Fig. 2.8, we show the amplitude gain versus time (in e-folding time of the π mode small-signal growth) for 200, 360, and 600 wire arrays.

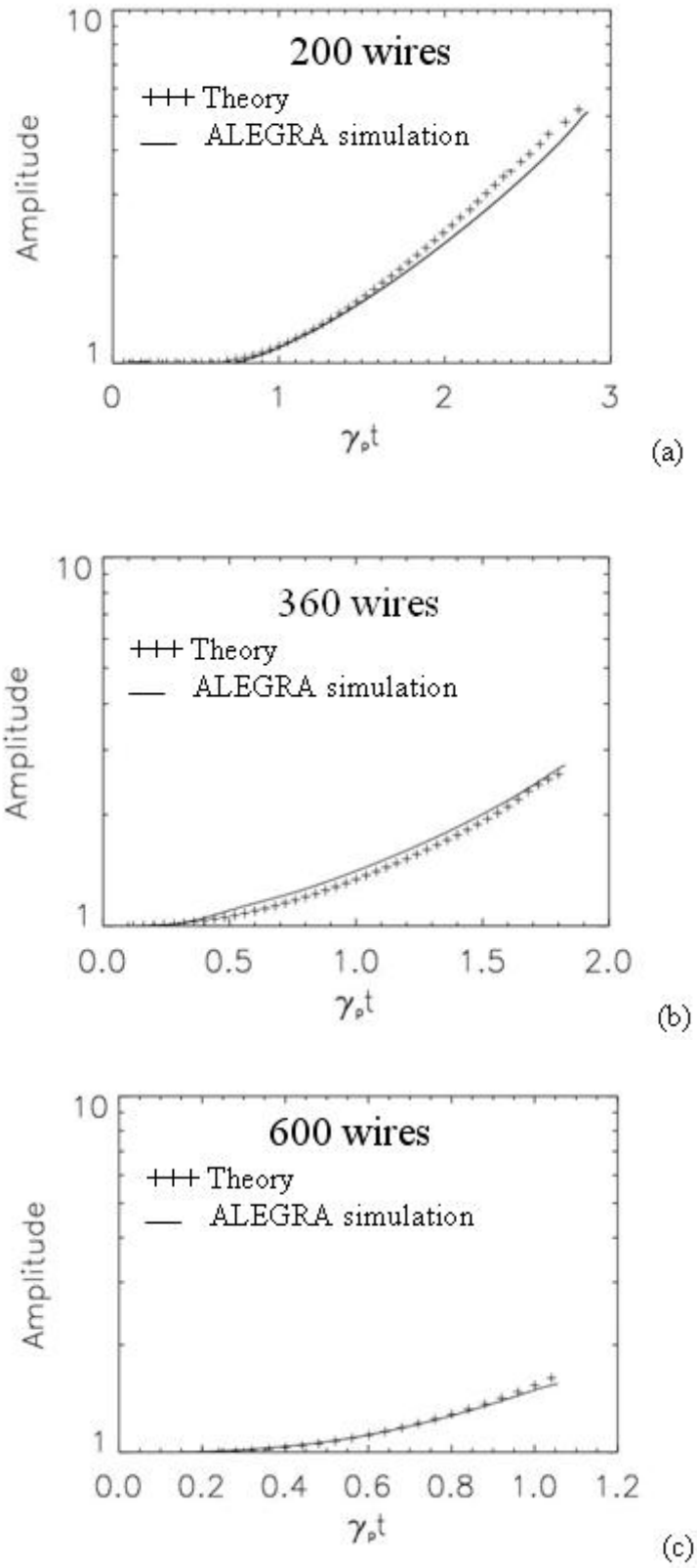

Fig. 2.8. Amplitude gain as a function of time for the π mode, with (a) N = 200, (b) N=360, and (C) N = 600.

The time intervals of simulation are ~45 ns for the 200-wire array, ~17 ns for the 360-wire array, and ~5 ns for the 600-wire array. The simulations were stopped when the wire touches the boundary of the wedge. The theoretical impact time, when the theory data terminate in Fig. 2.8, was calculated by using Eq. (2.12). It is evident from Fig. 2.8 that the ALEGRA simulations closely match the theory even though the theory model was an infinite linear wire array with vanishingly small wire diameter, while the simulation model was a cylindrical wire array whose wire diameter is finite.

In Fig. 2.9, we show the r-θ trajectory (radial position vs azimuthal displacement of the zeroth wire) for the π mode clumping in 200, 360, and 600 wires, ξ_0 is the displacement of the 0-th wire from its unperturbed position. The simulations were stopped when the wire touches the boundary of the wedge. Once more, these figures show good agreement between ALEGRA simulation results and the analytic theory, Eq. (2.15), in these high wire-number arrays.

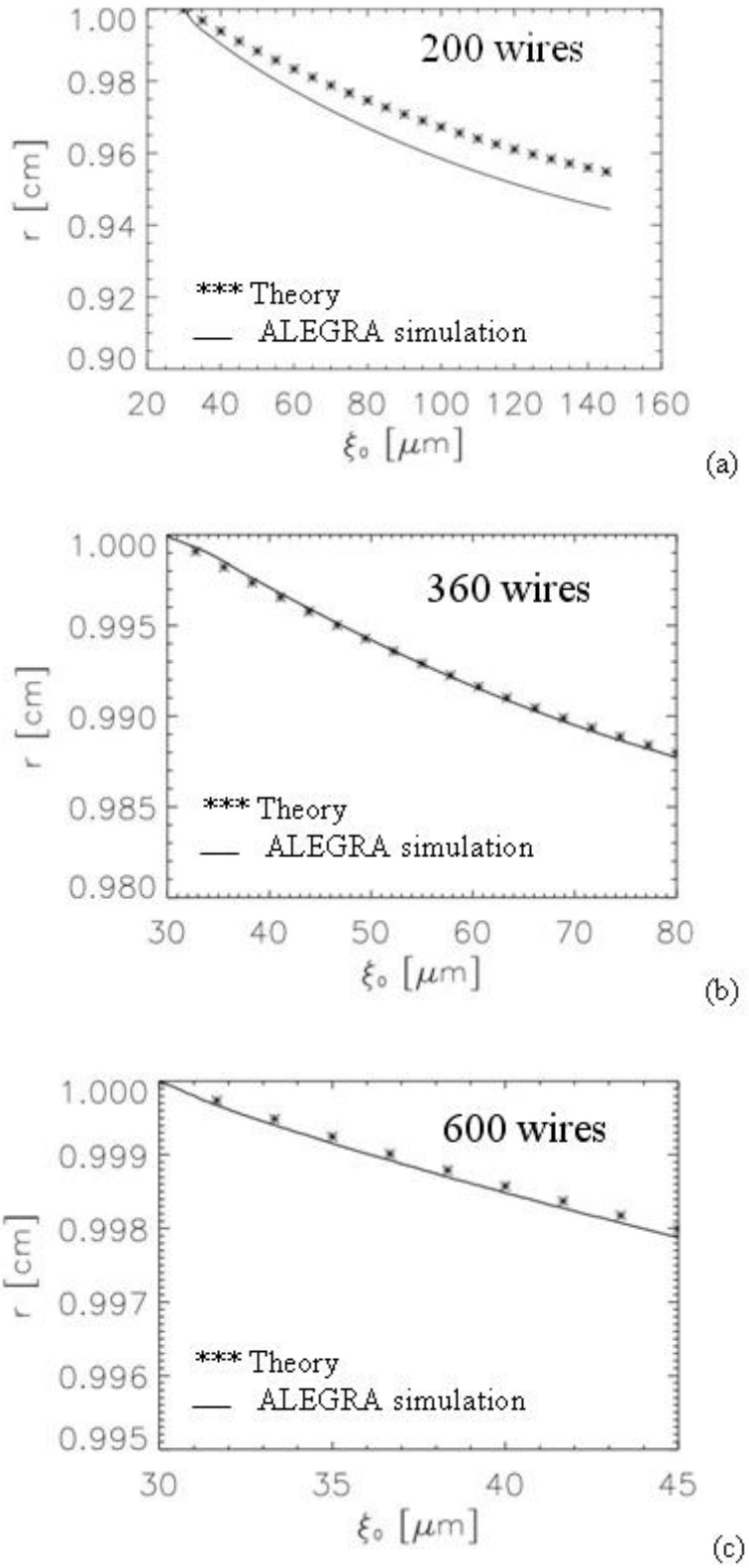

Fig. 2.9. r-θ trajectory for the π mode, with (a) N = 200, (b) N=360, and (c) N = 600.

2.2.2 Wire Impact Time Calculations (REIN simulation vs. Theory)

The resistive and inductive circuit code (REIN) developed by Strickler [Str03, Str06] is an extension, and a computationally more efficient version, of the model originally presented in Davis et al.[Dav97]. Temperature-dependent wire resistivity, arbitrary time-dependent voltage and current source terms have also been added to the model [Str06]. In this section, we compare the impact time of two wires from the simulation using the REIN code [Str03, Str06] with our theoretical model developed in Section 2.1, impact time is defined as the time it takes the two wires to collide with each other. The simulation geometry is shown in Fig. 2.10. The simulation was set up to increase the understanding of the experiments [Str06] that were conducted on the COBRA Z-pinch (1 MA, 100ns rise time [Kny97]) machine at Cornell University to study the dynamics of closely spaced pairs of parallel wires with center-to-center spacing of 244 μm and 456 μm in a cylindrical z-pinch array with a diameter of 16mm [Fig. 2.10].

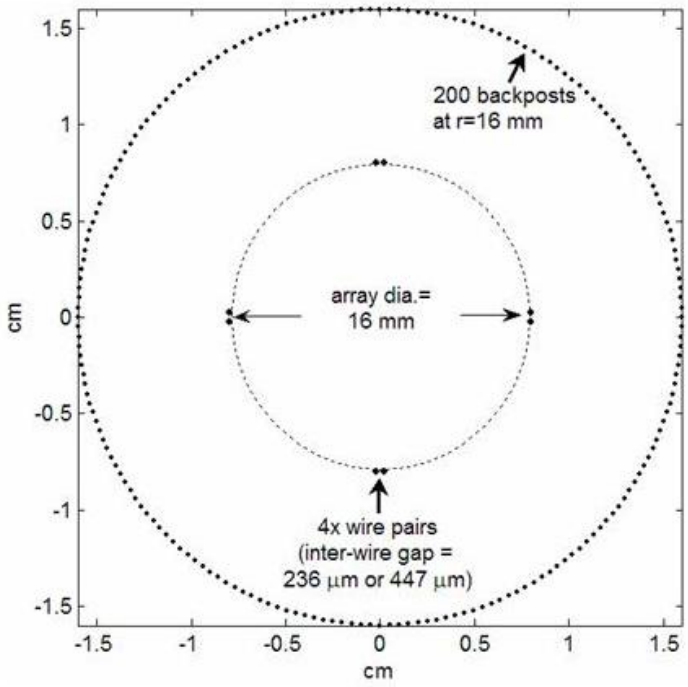

Fig. 2.10. Geometry used for the simulations of the Cornell paired wire experiments [from Str06].

First, simulations were set up by Strickler such that all the current (1 MA with 100 ns risetime) was assumed to flow in the wire cores. The results of these simulations and the resulting impact time are shown in Figs. 2.11(a) (236 μm spacing) and Fig. 2.11(b) (447 μm spacing) [Str06]. The simulations predicted that the wire cores would collide at 38 ns and 48 ns. The theoretical impact time can be calculated using Eq. 2.1, Eq. 2.5, and Eq. 2.12 in Section 2.1, by assuming a sinusoidal time-dependent current profile (dashed lines in Fig. 2.11a,b), the calculation was carried out with Mathematica [Appendix F]. The theoretical impact times are calculated to be 35.5 ns for the 236 μm case, and 44.46 ns for the 447 μm case, which reasonably matches the results given by the REIN simulations, 38 ns and 48 ns, respectively [see Table 2.1 below].

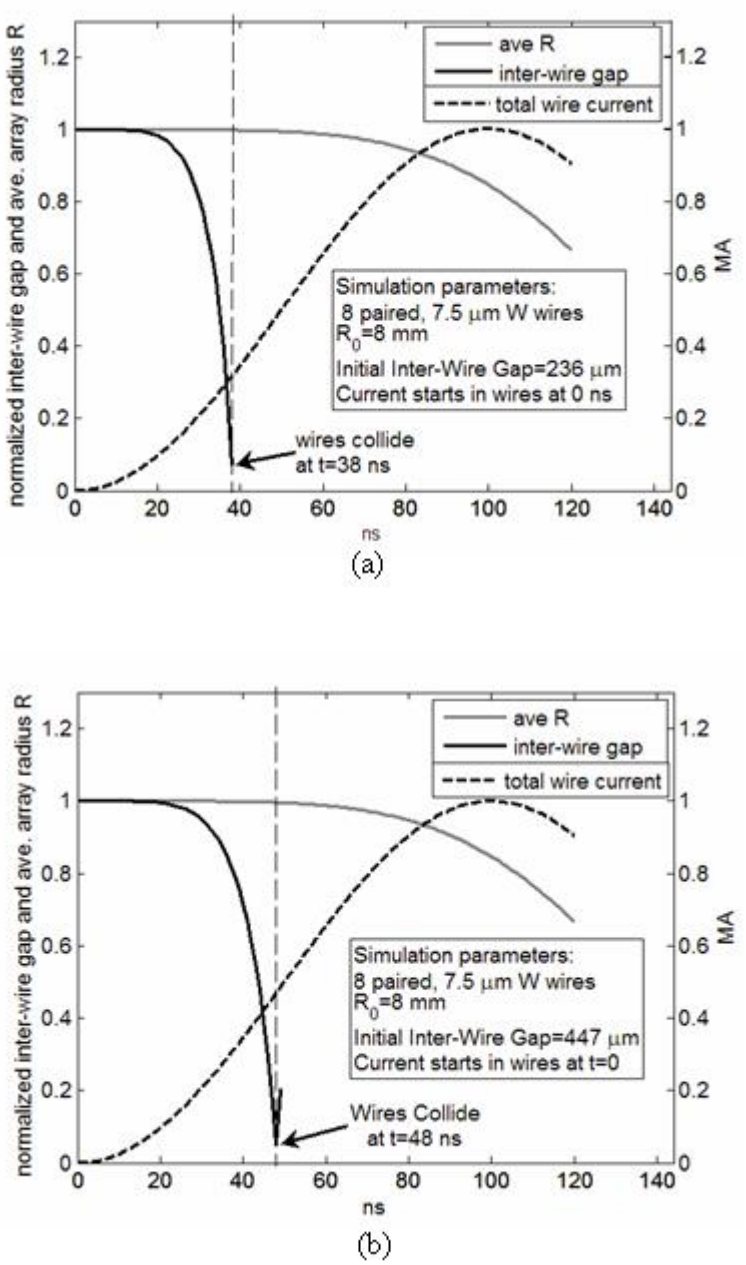

Fig. 2.11. Results of REIN simulations of the Cornell experiments, assuming all current flows in wire cores from t=0 ns. (a) shows the results of the wire colliding at 38ns for the 236 μm case, and (b) shows results of the wire colliding at 48ns for the 447 μm case [from Str06].

It is believed in the Z-pinch community that some or most of the current will be shunted by the ablation plasma for at least some part of the current pulse [Cun05a, Leb04, Sin05]. To simulate this effect, a set of simulations was performed by Strickler in which it was assumed that the current pulse (1 MA, 100 ns risetime) is "switched" to

the wire cores at some late time (t=60 ns) [Str06]. The results of these simulations and the corresponding impact time are shown in Figs. 2.12(a) and 2.12(b).

For both the 236 and 447 μm wire cases, the REIN simulations show the wires colliding rapidly after the current is switched to the cores, at 65 ns for the 236 μm case and at 69 ns for the 447 μm case. Again, the theoretical impact time can be calculated using Eq. 2.1, Eq. 2.5, and Eq. 2.12 in Section 2.1, by assuming that a constant current of magnitude 0.7 MA is present to the wire array at the time of "switched on" [Fig. 2.12], the calculation was carried out with Mathematica [Appendix G]. The theoretical impact times are calculated to be 64.94 ns for the 236 μm case, and 69.3 ns for the 447 μm case. The theoretical impact time again compares well with the results given by the REIN simulations, 65 ns and 69 ns, respectively [see Table 2.1 below].

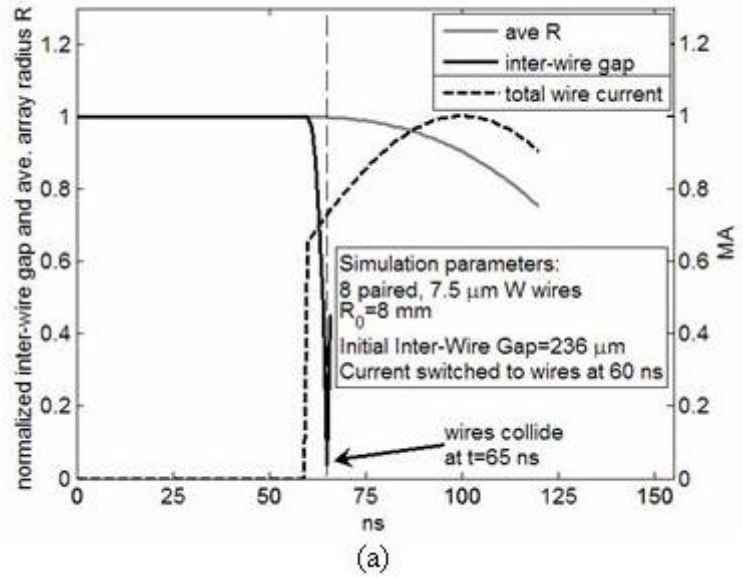

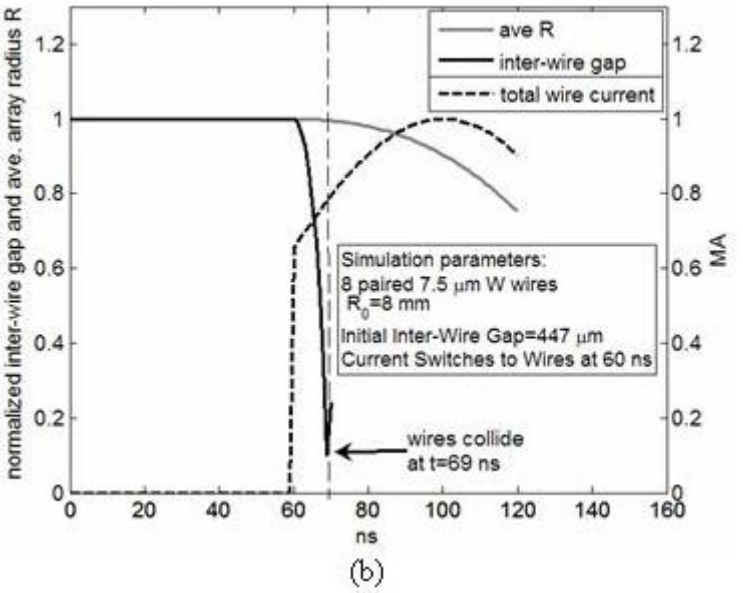

Fig. 2.12. Results of the REIN simulations of the Cornell Experiments, assuming current is "switched on" in the wires at t=60 ns into the current pulse. (a) shows the results of the wire colliding at 65ns for the 236 μm simulation, and (b) shows the results of the wire colliding at 69ns for the 447 μm simulation [from Str06].

Table 2.1: Impact time calculations: Non-linear theory in comparison with REIN simulation. (Collision time = Time of wire collides – Time of current starts)

	236 μm initial inter-wire gap		447 μm initial inter-wire gap	
	0 ns current start	60 ns current start	0 ns current start	60 ns current start
Collision time: Simulations	38 ns	5 ns	48 ns	9 ns
Collision time: Non-linear theory	35.5 ns	4.94 ns	44.46 ns	9.3 ns

2.2.3 Simulation Remarks

It is computationally difficult to resolve the azimuthal dependence in simulations if the number of wires, N, in the array runs into hundreds [Fig. 2.1]. For the azimuthal clumping instability, the most unstable mode is the π mode, which has the unique property that the azimuthal displacements of neighboring wires are exactly 180 degrees out of phase with each other [Fig. 2.2b]. From Fig. 2.2a, one sees that the π mode in a cylindrical array of N wires may be generated by just one wire, over a wedge of angle $2\pi/N$ radians that contains that wire, with a reflection condition applied to the boundaries of this wedge. We call this reduced, but equivalent, simulation of one wire over one wedge the "1-sector simulation". With a reflection condition on the boundary of this sector [See Fig. 2.2], it is clear that this 1-sector simulation exactly replicates the π mode in an N-wire cylindrical array. The 1-sector simulation automatically filters out all other azimuthal modes, so that it exclusively simulates the linear and nonlinear evolution of

the pure π mode, for all time. This 1-sector simulation, therefore, offers substantial saving in the simulation time to exclusively study the most unstable clumping mode, especially when N is in the hundreds. Note also the significant flexibility in this 1-sector simulation: changing the sector angle is equivalent to changing the number N in the array; thereby allowing a convenient study of the scaling with wire number against nonaxisymmetric perturbations.

We should stress that the 1-sector simulation applies even if the coronal plasma is present. This results in very significant flexibility in addition to substantial reduction in computational time. The linear and nonlinear theory for the pure π mode may readily be compared with the 1-sector simulation. Such a comparison may be considered as a benchmark for both theory and codes. The pure π mode, as represented by the 1-sector simulation, may also be subjected to experimental studies [Str06] by judiciously arranging the initial positions of the wires so that only the π mode is seeded [Figs. 2.2b and 2.10].

2.3 Conclusions

While the analytic theory was developed for a linear array of infinitesimally thin wire, it turns out that the theory provides a fairly accurate description when it is compared with ALEGRA simulations of a circular array of wires of finite wire radius. The theory also compares well (for the impact time calculations) with few-wire array in a circuit simulation model, REIN. The REIN code takes into account the inductance changes among the wires in the wire array as the wires azimuthally clump, the excellent agreement between the REIN simulation and theory developed implied that the inductance change is a negligible effect, as far as the azimuthal clumping instability is concerned. The general conclusion is that the π mode of discrete wires may undergo significant clumping before appreciable radial motion sets in. This trend should scale for

all current amplitudes and pulse timescales [Str06, Tan07]. Previously, the lack of radial motion of the wire core in experiments was used to infer that little current flows through the cores. Here, our theory and simulations show that azimuthal clumping of wires occurs on a faster time scale than the wires' radial motion, for most cases of experimental interest. Thus, azimuthal motion might serve as a more sensitive "diagnostic" to detect current in the cores than the radial motion. The lack of azimuthal clumping of the wires implies lack of current in the wire core. Indeed, Sinars [Sin05] already attributed the absence of azimuthal clumping mode, which was predicted by Hammer and Ryutov [Ham99b], to the shunting of the core current to the coronal plasma.

If the azimuthal clumping of wires is not observed in experiments, it admits a few possibilities: The majority of the current is not carried by the discrete wires, as already indicated, or much of the original wires lose their discrete properties. Unfortunately, these scenarios are difficult to quantify in experiments, and the analytic theory and simulation presented here have not included them either.

There is a general consensus that the plasma ablated from the wires could shunt the current from the wire cores at times throughout a wire array implosion. In the wire Z-pinch experiments, the axial current, at some stage, may be shared or even predominantly carried by the plasma corona surrounding the wires [Leb04]. When this happens, the metallic wires may be detached from the plasma corona as far as the Jeans (clumping) instability is concerned, and the cores would probably not move. Attention should then be shifted to the plasma corona. For instance, it may be possible to observe the merging of plasma "streams" coming off of the individual wires, rather than the merging of neighboring discrete wire cores. In Sanford's study of scaling with wire number [San01], a decisive criterion centered on the distinction between "plasma-wire"

(in which the plasma coronas from neighboring wires do not coalesce) and "plasma-shell" (in which the plasma coronas from neighboring wires coalesce). Interestingly, this idea may be re-examined critically with 1-sector simulation with reflection boundary condition [Fig. 2.2a], and such a simulation will have taken full consideration of the collective interaction of all discrete wires, "plasma-wires", and "plasma-shell", regardless of the wire number.

An attempt was made by the present author to investigate the clumping instability when the discrete wire is replaced by plasma. Two different ALEGRA simulation geometries were set up: (a) the plasma is circular in shape centered about the original wire, and (b) the plasma is radially elongated in shape, [the simulations were set up using similar parameters as given in Section 2.2.1, with discrete wire being replaced by plasma]. The simulation setup geometry, ALEGRA input deck, and preliminary results with a plasma circular in shape are given in Appendix E. Since the force between two infinitely long current planes is independent of the distance between them, we expect the elongated (radially spread-out) plasma geometry will be less susceptible to the azimuthal clumping instability compares to the circular plasma. In both cases, preliminary results show mitigation of clumping instability with the replacement of discrete wire with plasma. However, more simulations and studies need to be conducted in order to solidify such a claim.

CHAPTER 3

A HIGHER DIMENSIONAL THEORY OF ELECTRICAL CONTACT RESISTANCE

In this chapter, we focus on the higher dimensional theory of electrical contact resistance. In a wire-array Z-pinch, the contact between the wires with the anode and with the cathode has a strong influence on the energy deposition in the wire [Gom07, Gom08, Zie08]. The problem of contact resistance is also important to terahertz sources, due to small circuit size [Boo07, Ppe07].

Because of the surface roughness on a microscopic scale, true contact between two pieces of metal occurs only on the asperities of the two contacting surfaces. Current flows only through these asperities, which occupy a small fraction of the area of the nominal contacting surfaces. This gives rise to contact resistance [Hol67, Jan03, Nak93, Ros81, Tim99], as shown in Fig. 3.1.

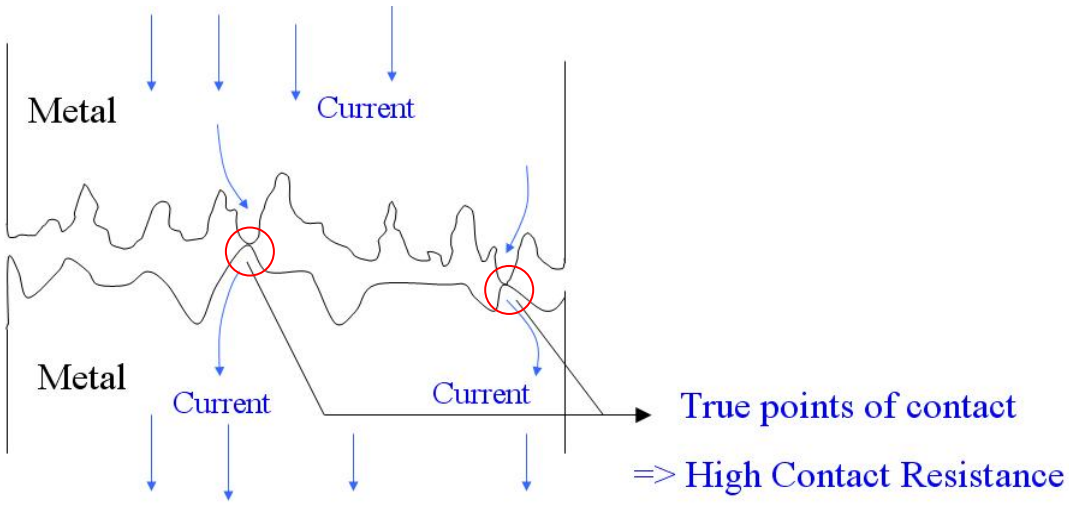

Fig. 3.1 **True points of contact occur only at the asperities of the contacting surface, leading to high contact resistance.**

It is clear that contact resistance is highly random, depending on the surface roughness, on the applied pressure, on the hardness of the materials, and perhaps most importantly, on the residing oxides and contaminants at the contact [Car95, Hol67, Tim99]. The basic model of electrical contact remains that of Holm [Hol67], who more than forty years ago considered two semi-infinite cylinders of radius b placed together. Current can flow through them only via a "bridge" in the form of a circular disk of radius $a << b$ [Fig. 3.2]. This disk has a zero thickness, and has been known as the "a-spot" in the literature; we called this configuration the zero-bridge length (ZBL) limit.

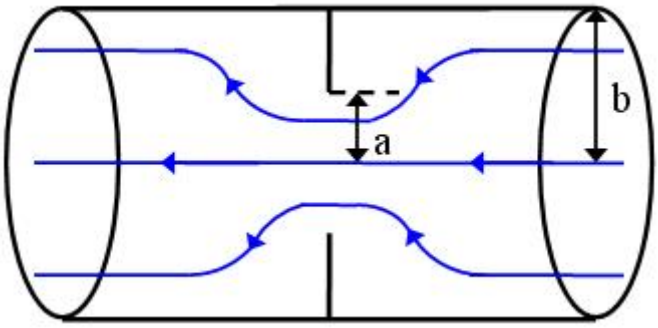

Fig. 3.2 Holm-Timsit model of a straight cylinder current channel of radius b joint by a zero thickness circular hole of radius a (a-spot).

While there are statistical treatments [Jan03] and extensions of the a-spot theory to other disk shapes [Nak93, Tim99], Holm's zero-thickness assumption is almost always used. Although it was not noted in Holm [Hol67] or Timsit [Tim99], Hall [Hal67] used conformal mapping for varieties of complex Cartesian geometries. The analog of the "a-spot" in Cartesian geometry is shown in Fig. 3.3, in which the connecting bridge also has a zero length in the direction of current flow.

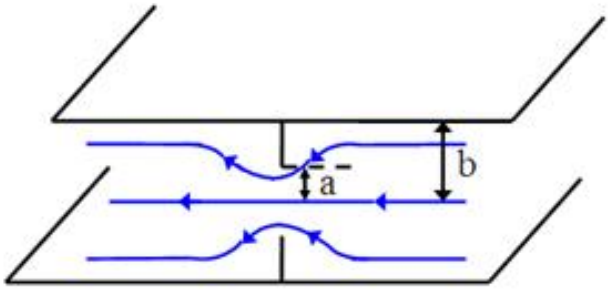

Fig. 3.3 **A rectangular current channel with a constriction of zero bridge length.**

In this chapter, we generalize the Holm-Timsit theory of a-spot [Hol67, Tim99] to include a finite axial length ($2h$) in the connecting bridge, i.e., the a-spot has a finite thickness in the direction of current flow. This is shown in Fig. 3.4 for a Cartesian geometry.

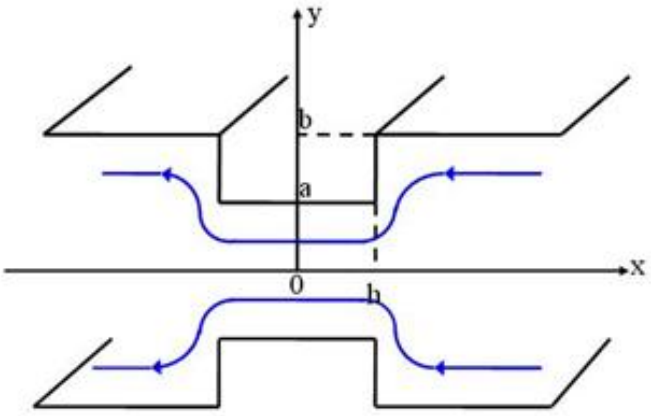

Fig. 3.4 **A rectangular current channel with a finite axial length of $2h$ in the direction of current flow.**

The mapping function for Fig. 3.4 is not displayed in, nor readily obtainable from Hall [Hal67]. We have obtained analytic result for a rectangular connecting bridge [Fig. 3.4], and we have used this result to propose the theory for cylindrical [Fig. 3.5] and funnel connecting bridge [Fig. 3.6].

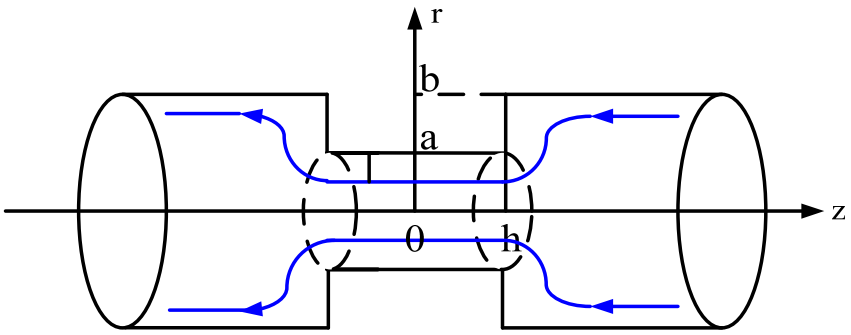

Fig. 3.5 **A connecting bridge in the form of a striaght cylinder of radius *a* and a finite axial of *2h* in the direction of current flow.**

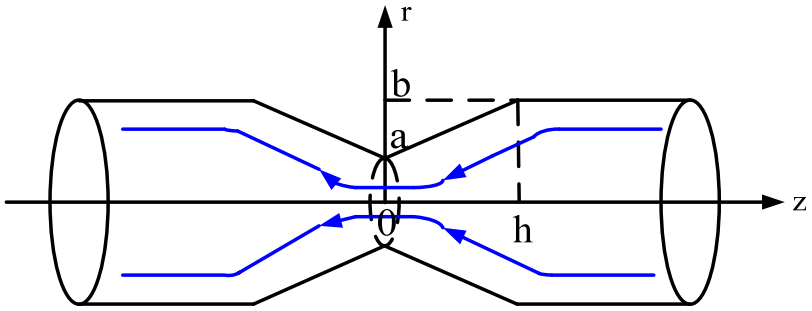

Fig. 3.6 **A funnel shape bridge with a finite axial length of 2*h* in the direction of current flow.**

We have verified that the proposed scaling laws are accurate to within one percent when compared with electrostatic code (MAXWELL 3D [Ans70]) results in spot checks. In addition, a statistical analysis of electrical contact resistance is developed in this chapter to analyze the randomness on the connecting bridge geometry. Lump parameters and radio frequency (*RF*) properties of the electrical contact are also studied. The final section gives a comparison of the theory with the UM Z-pinch experiments on contact resistance [Gom08].

3.1 Analytic Theory of Electrical Contact Resistance

The basic model of electrical contact resistance is due to Holm [Hol67]. In this section, we introduce the conformal mapping for a rectangular geometry, and analyze the ZBL theory for a rectangular [Fig. 3.3] and cylindrical channel [Fig. 3.2]. Higher dimensional theory for the rectangular [Fig. 3.4], cylindrical [Fig. 3.5] and funnel channel [Fig. 3.6] will follow. In all of the higher dimensional cases, we find good agreement between the electrostatic code (MAXWELL 3D [Ans70]) results and the analytic theory developed.

3.1.1 Conformal Mapping for Rectangular Geometry

We first consider a 2-dimensional rectangular current channel Fig.3.7a with top boundary ABCDEF and mid-plane GH (y=0). The main channel has half width b, and the bridge, or constriction, has half width $a < b$, and total length $2h$ (we will set $h=0$ to analyze the ZBL limit in the next section). The width is L_3 in the third, ignorable dimension. The two boundaries, ABCDEF and GH, are streamlines. The Cartesian geometry allows us to solve the current flow by conformal mapping between the complex z- and w-plane where $z = x + iy \equiv (x, y)$ and $w = u + iv \equiv [u, v]$.

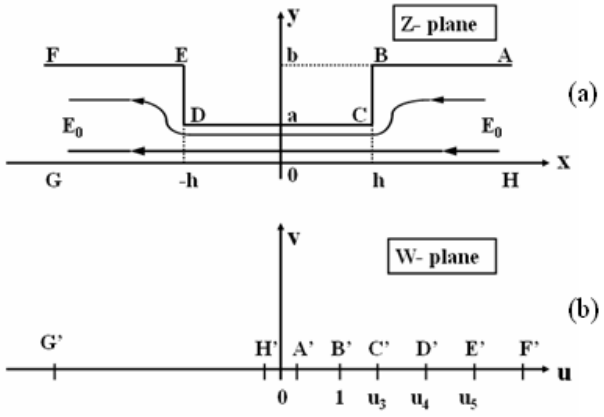

Fig. 3.7(a,b) (a) The half rectangular current channel in the $z \equiv (x, y)$ plane, and (b) its map onto the $w \equiv [u, v]$ plane.

This map is governed by the Schwarz-Christoffel transformation [Hil62]. The mapping function is given by Eq. (3.1), which maps ABCDEF and GH in the z-plane onto A'B'C'D'E'F' and G'H' of the w-plane, where *f(w)* is given by Eq. (3.2), and the aspect ratios *h/b* and *a/b* are given in terms of u_3 and u_4 [labeled in Fig. 3.7b] by Eqs. (3.3a,b). The detail of the mapping and the derivation of Eqs. (3.2) and (3.3a,b) will be given in Appendix H.

$$\frac{dz}{dw} = Kf(w), \quad K = -\frac{b}{\pi} \ . \tag{3.1}$$

$$f(w) = \frac{1}{w}\sqrt{\frac{(w-u_3)(w-u_4)}{(w-1)(w-u_5)}}; \qquad u_5 = u_3\, u_4 \, . \tag{3.2}$$

$$\frac{h}{b} = \frac{1}{2\pi}\int_{u_3}^{u_4} dw\left|f(w)\right|, \qquad \frac{a}{b} = 1 - \frac{1}{\pi}\int_{1}^{u_3} dw\left|f(w)\right| \, . \tag{3.3a,b}$$

Note that $u_5 = u_3 u_4$ in Eq. (3.2). Thus, once *h/b* and *a/b* are specified, u_3 and u_4 (and therefore $u_5 = u_3 u_4$) may be determined numerically from Eq. (3.3), and the entire mapping function of Eq. (3.2) is known.

To show that $u_5 = u_3 u_4$, consider the complex electrostatic potential, $\Phi(w) = KE_0 \log(w) = \phi + i\psi$, which represents the potential function and stream function of a source at the origin of the w-plane that produces a constant electric field ($-E_0$) far away from the constriction in the z-plane [Fig. 3.7]. The components E_x and E_y of the electrostatic field in the (x,y) plane may be expressed as [Hil62] ,

$$E_x - iE_y = -\frac{d\Phi}{dz} = -\frac{d\Phi/dw}{dz/dw} = -E_0\sqrt{\frac{(w-1)(w-u_5)}{(w-u_3)(w-u_4)}} \, . \tag{3.4}$$

Eq. (3.4) clearly shows a constant E_x at $w = \infty$ and at $w = 0$, e.g., at the downstream location F'(F) and the upstream location A'(A) in Fig. 3.7. For F and A to assume this

same electric field, -E_0, Eq. (3.4) yields $u_5 = u_3u_4$. In Appendix H, we show that the contact resistance of the 2-dimensional rectangular current channel is,

$$R_c = \frac{\rho}{2\pi L_3}\overline{R}_c, \qquad \overline{R}_c = \int_0^\infty \frac{du}{u}\left[1 - \sqrt{\frac{(u+u_3)(u+u_4)}{(u+1)(u+u_3u_4)}}\right]. \tag{3.5}$$

The contact resistance R_c is defined as the difference between R and R_u, where R is the resistance of the channel between points G and H in Fig. 3.7a (taking $G \to -\infty$ and $H \to \infty$ at the last stage), and R_u is the resistance between the same points G and H of the un-constricted channel, i.e. $a=b$ in Fig. 3.7a. The contact resistance R_c depends only on the aspect ratios, h/a and b/a, the specification of which determines the mapping parameters u_3 and u_4 from Eqs. (3.3a,b).

3.1.2 Zero-Bridge Length Theory

The contact resistance in the ZBL limit is presented in this subsection for the rectangular channel (Fig. 3.3) and cylindrical channel (Fig. 3.2). For the cylindrical channel, the ZBL theory is simply the Holm-Timsit theory of a-spot [Hol67, Tim99].

A. Rectangular Channel

For the zero bridge length (ZBL) limit, we set $u_3 = u_4$ in Eqs. (3.2), (3.3a,b), and (3.5) [Fig. 3.7a, $h=0$ for ZBL limit]. The channel width is L_3 in the third, ignorable dimension. The channel has a uniform electrical resistivity ρ. The contact resistance in this case reads,

$$R_c = \frac{\rho}{2\pi L_3}\overline{R}_{c0}, \quad \overline{R}_{c0} = \int_0^\infty \frac{du}{u}\left[1 - \frac{u+u_3}{\sqrt{(u+1)(u+u_3{}^2)}}\right] \tag{3.6}$$

where $\overline{R}_{c0}$ is a function of u_3, and u_3 is related to b/a by Eq. (I2) of Appendix I.

This normalized ZBL resistance $\overline{R}_{c0}$ is shown in Fig. 3.8 together with its asymptotic expansion for $b/a >> 1$,

$$\overline{R}_{c0} \cong 4\log[2b/(\pi a)], \qquad b/a >> 1 \ . \tag{3.7}$$

Equation (3.7) is derived in Appendix I. Given the aspect ratio b/a, u_3=u_4 needs to be solved numerically from Eq. (3.3b), and $\overline{R}_{c0}$ is then obtained numerically from Eq. (3.6). The numerical data in Fig. 3.8 show that $\overline{R}_{c0}$ is zero when b/a = 1, as expected for the rectangular channel without any restriction. The zero-bridge-length (ZBL) limit is shown in Fig. 3.8, together with the asymptotic formula [Eq. (3.7)]. Figure 3.8 shows its excellent agreement with the numerical values. The log(b/a) dependence in Eq. (3.7) for the rectangular channel for small a is very different from the 1/a dependence in the classical scaling of the a-spot theory for a cylindrical channel, to be discussed next.

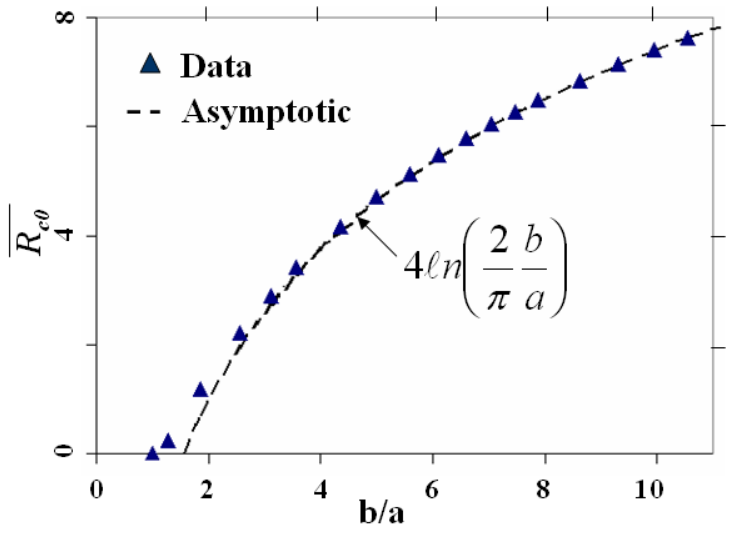

Fig. 3.8 **The normalized contact resistance of a rectangular current channel with zero bridge length. Also shown is the asymptotic formula for $b/a >> 1$ (dash curve).**

B. Cylindrical Channel – The Holm-Timsit a-spot Theory

Holm [Hol67], more than forty years ago considered two semi-infinite cylinders of radius b placed together (Fig. 3.2). Current can flow through them only via a bridge in the form of a circular disk of radius $a << b$, where b is the main channel radius (Fig.

3.2). This disk has a zero thickness (*h = 0* in Fig. 3.5), and has been known as the "a-spot" in the literature. Holm derived the contact resistance in the limit $b \to \infty$, *h=0*, yielding his celebrated formula [Hol67],

$$R_c(Holm) = \frac{\rho}{2a}, \text{ (Holm's a-spot theory)} \qquad \textbf{(3.8)}$$

Timsit [Tim99] extended Holm's a-spot theory to a finite value of main channel radius (*b*),

$$R_c = \frac{\rho}{2a}\overline{R}_{c0}, \qquad \textbf{(3.9)}$$

$$\overline{R}_{c0} = 1 - 1.41581(a/b) + 0.06322(a/b)^2 + 0.15261(a/b)^3 + 0.19998(a/b)^4, \qquad \textbf{(3.10)}$$

Equation (3.9) was synthesized by Timsit from his numerical results into this useful, accurate formula [Tim99], Eq. (3.10). Figure 3.9 displays $\overline{R}_{c0}$ (normalized to $\rho/(2a)$), showing that the contact resistance vanishes when *a = b*, as expected for the cylindrical channel without any constriction. Equation (3.9) reduces to Eq. (3.8) in the limit of $b \to \infty$.

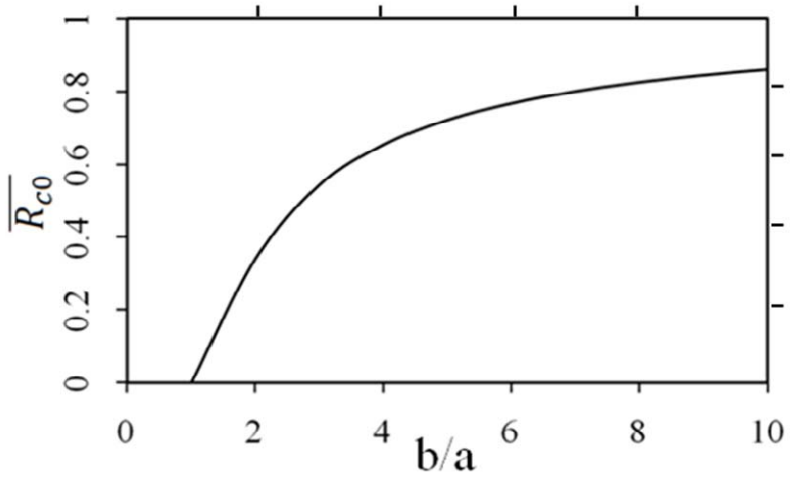

Fig. 3.9 **Timsit's normalized contact resistance for a straight cylinder current channel with zero bridge length. As $b/a \to \infty$, $\overline{R}_{c0} = 1$, the value of Holm's a-spot theory.**

3.1.3 Higher Dimensional Theory for Non-zero Bridge Length

When the bridge, or constriction, has a finite length, h, the analysis of contact resistance becomes significantly more complicated. The contact resistance depends on two dimensionless parameters, b/a and h/a. In this section, we consider three cases: (A) the rectangular channel with a rectangular bridge (Fig. 3.4), (B) the cylindrical channel in which the bridge is a cylinder of radius $a < b$ (Fig. 3.5), and (C) the cylindrical channel in which the bridge is a funnel whose radius increases linearly from a to b from the narrowest point (Fig. 3.6). In all three cases, the bridge has a total length of $2h$. The effect of finite h is found to increase the contact resistance linearly with h, by an amount that is expected from the increase in the current path length associated with finite h, and from the decrease in the cross-sectional area in the channel constriction. This physical appealing result was first hinted from the data for the rectangular channel, which we solved by conformal mapping. Conformal mapping is inapplicable to the cylindrical cases, (B) and (C), but we find the above effect of finite h is also consistent with the numerical results that we obtain from a 2-dimensional electrostatic code in our study of cases (B) and (C).

Specifically, we postulate that, as a result of finite h, $\overline{R}_{c0}$ in Eq. (3.6) [for case (A)] and in Eq. (3.9) [for cases (B) and (C)] are replaced by

$$\overline{R_c} = \overline{R_{c0}} + s(h/a). \qquad \textbf{(3.11)}$$

where s is a constant that depends only on b/a for the specific geometry. In the following subsections, we provide a simple derivation of s for all three cases and compare the prediction according to Eq. (3.11) with numerical data.

A. Rectangular Channel with Rectangular Constriction of Finite Length

Let us focus at the connecting bridge region in Fig. 3.4: $-h < x < h$, $-a < y < a$. If there were no constriction, $a = b$, the electrical resistance in that region would be,

$$R'_{cu} = \rho(2h)/(2b \times L_3), \tag{3.12}$$

where L_3 is the width of the rectangular channel in the third dimension. With the constriction, $a < b$, the resistance of that bridge becomes,

$$R'_c = \rho(2h)/(2a \times L_3), \tag{3.13}$$

Thus, the effect of the finite bridge length ($h > 0$) gives rise to an additional resistance,

$$R' = R'_c - R'_{cu} = (1 - a/b)\rho h/(aL_3). \tag{3.14}$$

Normalizing R' to $\rho/(2\pi L_3)$ and calling this normalized additional resistance $s(h/a)$, as suggested by Eqs. (3.5) and (3.11) we obtain the slope s for a rectangular connecting bridge channel,

$$s_R = 2\pi(1 - a/b), \tag{3.15}$$

The contact resistance for a rectangular current channel then reads,

$$R_c = \frac{\rho}{2\pi L_3}\left[\overline{R}_{c0} + s_R(h/a)\right] \equiv \frac{\rho}{2\pi L_3}\overline{R}_c, \tag{3.16}$$

where $\overline{R}_{c0}$ is given in Fig. 3.8 and s_R is given by Eq. (3.15). The straight lines in Fig. 3.10a represent the linear increase of the normalized contact resistance $\overline{R_c} = \overline{R}_{c0} + s_R(h/a)$ with h/a according to Eq. (3.15) for several values of b/a. The squares in Fig. 3.10a show the values of $\overline{R_c}$ according to Eq. (3.5), which is derived vigorously using conformal mapping as given in the last section. The spot checks on the analytic results against conformal mapping are also shown in different forms in Fig 3.10b. In Fig. 3.10b, we plot Eq. (3.16) as a function of b/a at various values of h/a, and check against the rigorous results using conformal mapping at a few random combinations of h/a and b/a. Furthermore, from the numerical data shown in Fig. 3.10 obtained from conformal mapping, we can infer what should be the value of s for each combination of b/a, and h/a. These values of s are marked as "data" in Fig. 3.11 and compared against the simple

analytic formula, Eq. (3.15), that we constructed from a simple physical argument. [Actually, it is the data from conformal mapping that led to the simple construction of *s* given in Eq. (3.15).] The curve for the *h/a=0* case, labeled as $\overline{R}_{c0}$ in Fig. 3.10b, corresponds to the zero-bridge length (ZBL) limit shown in Fig. 3.8.

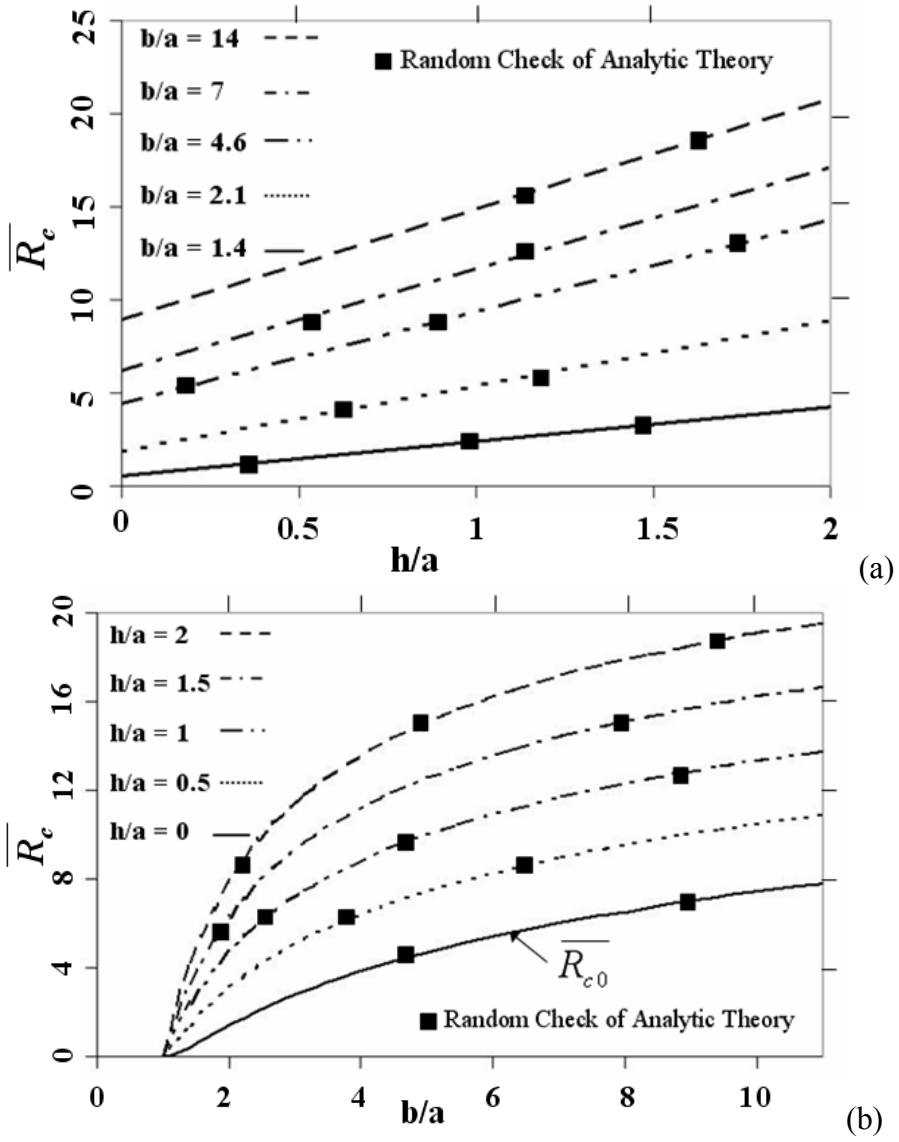

Fig. 3.10(a,b) The normalized contact resistance (a) as a function of *h/a* at various values of *b/a*, and (b) as a function of *b/a* at various values of *h/a* for a rectangular current channel. The squares show values according to the exact analytic theory, Eq. (3.5), at some random combinations of *h/a* and *b/a*.

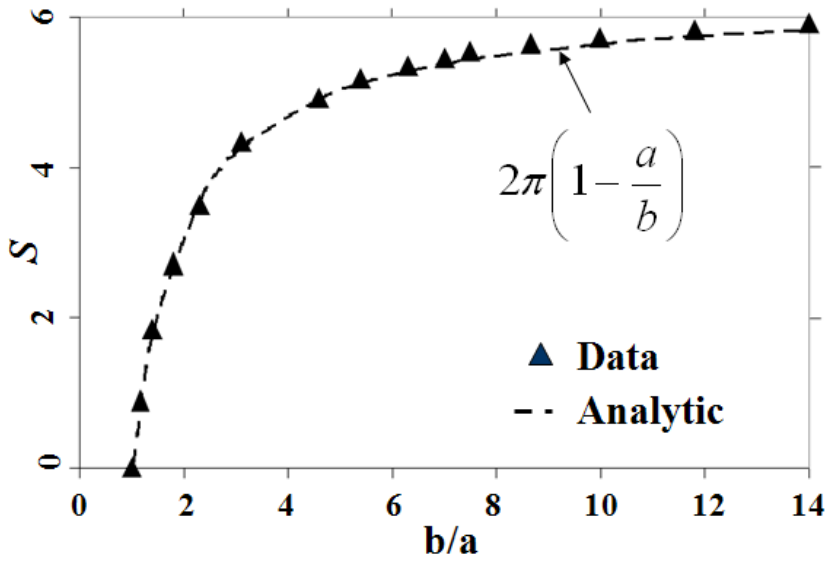

Fig. 3.11 **The normalized rate of increase of the contact resistance with respect to the bridge length, extracted from numerical data for a rectangular current channel. Also shown is the analytic formula (dash curve).**

B. Cylindrical Channel with Cylindrical Constriction of Finite Length

The great accuracy of the analytic theory displayed in Figs. 3.10 -3.11 prompted us to consider the cylindrical geometry next [Fig. 3.5]. The main cylindrical current channel has radius *b*, and the connecting bridge has radius *a (<b),* and total axial length *2h*. Let us focus at the connecting bridge region for the cylindrical case. This cylindrical geometry reduces to the circular a-spot of Holm in the *h = 0* limit. Using similar argument as given in the rectangular bridge, if there were no constriction, *a = b*, the electrical resistance in the cylindrical bridge would be,

$$R'_{cu} = \rho(2h)/(\pi b^2). \tag{3.17}$$

With the constriction, *a < b*, the resistance of the cylindrical bridge becomes,

$$R'_{c} = \rho(2h)/(\pi a^2). \tag{3.18}$$

Therefore, the effect of the finite bridge length (*h > 0*) gives rise to an additional resistance,

$$R' = R'_{c} - R'_{cu} = \left[1-(a/b)^2\right]\rho h(2/\pi a^2). \tag{3.19}$$

Normalizing R' to $\rho/(2a)$ and calling this normalized additional resistance *s(h/a)*, as suggested by Eqs. (3.9) and (3.11), we obtain the slope s for a cylindrical connecting bridge,

$$s_{sc} = (4/\pi)[1-(a/b)^2]. \quad \textbf{(3.20)}$$

The proposed contact resistance for the straight cylindrical bridge [Fig. 3.5] then reads,

$$R_c = [\rho/(2a)][\overline{R}_{c0} + s_{sc}(h/a)] \equiv \frac{\rho}{2a}\overline{R}_c, \quad \textbf{(3.21a)}$$

$$\overline{R}_{c0} = 1 - 1.41581(a/b) + 0.06322(a/b)^2 + 0.15261(a/b)^3 + 0.19998(a/b)^4, \quad \textbf{(3.21b)}$$

where s_{sc} is given by Eq. (3.20) and $\overline{R}_{c0}$ is simply the classical a-spot contact resistance of Holm and Timsit, Eq. (3.10). Equation (3.21a) is represented by the straight lines in Fig. 3.12 for several values of *b/a*.

To test the proposed scaling, Eq. (3.21a), we set up simulations using electrostatic codes with DC conduction, as the analytic calculation becomes very complicated, and conformal mapping can no longer be used for the cylindrical geometry. We applied an excitation voltage of 100V, we also assume a tungsten channel with a resistivity $\rho = 5.5\times10^{-8}\ \Omega m$, constriction radius *a = 1 mm*, channel radius *b* ranging from *1.5 mm* to *5 mm*, finite axial length 2*h* ranging from *0 mm* to *10 mm*, and axial total length of the geometry ranging from *20 mm* to *30 mm*. We have verified that Eqs. (3.21a) is accurate to within one percent when compared with the electrostatic code results in spot checks with *b/a* = 1.5, 2, 3, 4 and 5, and *h/a* from 0 to 5, as shown in Fig. 3.12. An example of the simulation setup using Maxwell 3D is shown in Fig. 3.13.

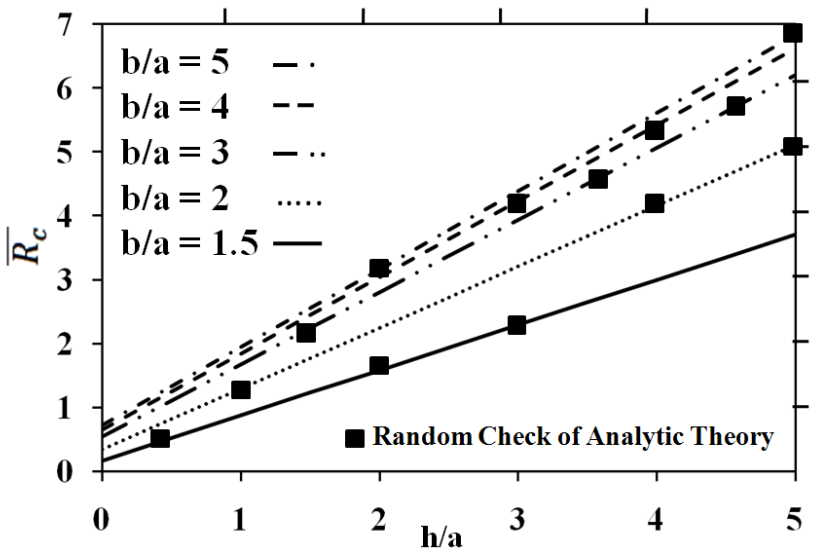

Fig. 3.12 **The normalized contact resistance as a function of h/a at various values of b/a for a straight cylinder connecting bridge. The squares show values according to spot checks with electrostatic code.**

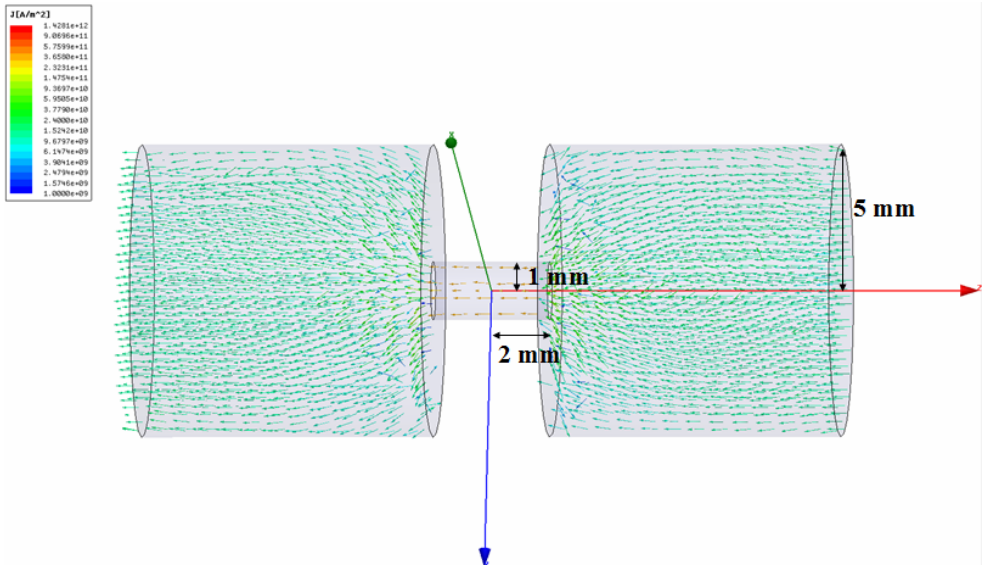

Fig. 3.13 **Maxwell 3D simulation geometry for a tungsten channel with b/a=5 and h/a=2 for a straight cylinder connecting bridge.**

C. Cylindrical channel with funnel constriction of finite length

Finally, we consider a cylindrical channel whose connecting bridge is in the shape of a funnel, as shown in Fig. 3.6. The main channel has a radius *b*. The funnel-shape constriction has a minimum radius $a < b$ and a total length $2h$. We assume that the funnel radius increases linearly with distance $|z|$ from the narrowest point (Fig. 3.6).

This funnel geometry also reduces to the circular a-spot of Holm[Fig. 3.2] in the $h = 0$ limit.

To evaluate the effect of finite axial length of the funnel analytically, we use similar arguments as given for cases (A) and (B) in this subsection. If there were no constriction, $a = b$, the electrical resistance in the region $-h < z < h$ would be the same as for the straight cylinder case, Eq. (3.17),

$$R'_{cu} = \rho \times 2h \Big/ \left(\pi b^2\right). \tag{3.22}$$

With the constriction, $a < b$, the incremental resistance over an axial length dz of the funnel is, $\rho dz \Big/ \left[\pi r^2(z)\right]$. The total resistance of the funnel connecting bridge becomes

$$R'_c = \int_{-h}^{h} dz \frac{\rho}{\pi r^2(z)} = \frac{\rho \times 2h}{\pi ab}, \tag{3.23}$$

where we have used the profile of the funnel radius, $r(z) = a + |z|(b-a)/h$, for $-h < z < h$, as shown in Fig. 3.6. Thus, the effect of the finite bridge length ($h>0$) gives rise to an additional resistance,

$$R' = R'_c - R'_{cu} = \left(1 - \frac{a}{b}\right)\frac{\rho \times 2h}{\pi ab}. \tag{3.24}$$

Normalizing R' to $\rho/2a$ and calling this normalized additional resistance $s(h/a)$, as suggested by Eqs. (3.9) and (3.11), we obtain the slope s for the funnel connecting bridge,

$$s_F = \frac{4}{\pi}\left(\frac{a}{b}\right)\left[1 - \frac{a}{b}\right], \tag{3.25}$$

The proposed contact resistance for the funnel shape constriction [Fig. 3.6] then reads,

$$R_c = [\rho/(2a)][\overline{R}_{c0} + s_F(h/a)], \tag{3.26a}$$

$$\overline{R}_{c0} = 1 - 1.41581(a/b) + 0.06322(a/b)^2 + 0.15261(a/b)^3 + 0.19998(a/b)^4 \tag{3.26b}$$

where s_F is given by Eq. (3.25) and $\overline{R}_{c0}$ is simply the classical a-spot contact resistance of Holm and Timsit, Eq. (3.10). Note that the slopes of these lines, measured S_F, are maximuized when b/a=2 according to Eq. (3.25). Thus, the straight lines for the b/a=3, 4, 5 cases crossed in Fig. 3.14. Eq. (3.25) shows that in the limit $b \to \infty$, $s_F \to 0$. This is expected since the geometry in the limit of infinite *b* (fixing *h* and *a* in Fig. 3.6) becomes the a-spot geometry of Holm, i.e., the effect of finite h vanishes. Equation (3.26a) is represented by the straight lines in Fig. 3.14 for several values of *b/a*.

To test the proposed scaling, Eq. (3.26a), we again use the electrostatic codes for the funnel constriction. We have verified that Eq. (3.26a) and (3.26b) are accurate to within one percent when compared with electrostatic code results in spot checks with *b/a* = 1.5, 2, 3, 4 and 5, and h/a from 0 to 5, as shown in Fig. 3.14. An example of the simulation setup using Maxwell 3D is shown in Fig. 3.15.

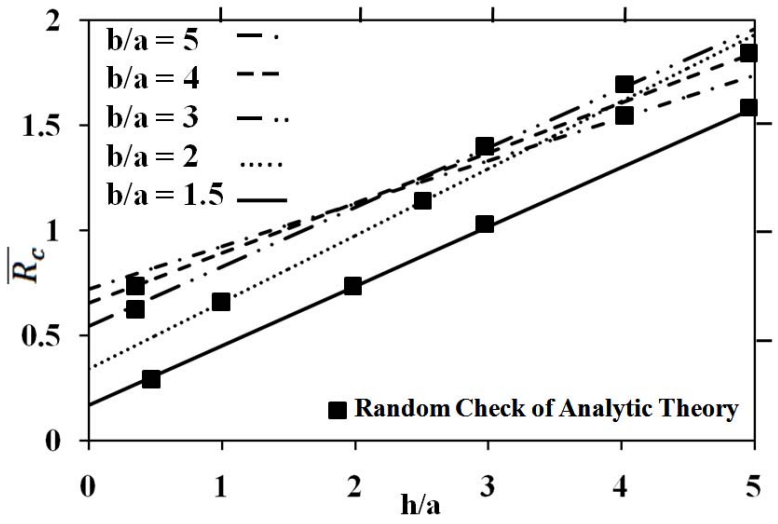

Fig. 3.14 **The normalized contact resistance as a function of h/a, at various values of b/a for a funnel shaped constriction. The squares show values in spot checks using an electrostatic code.**

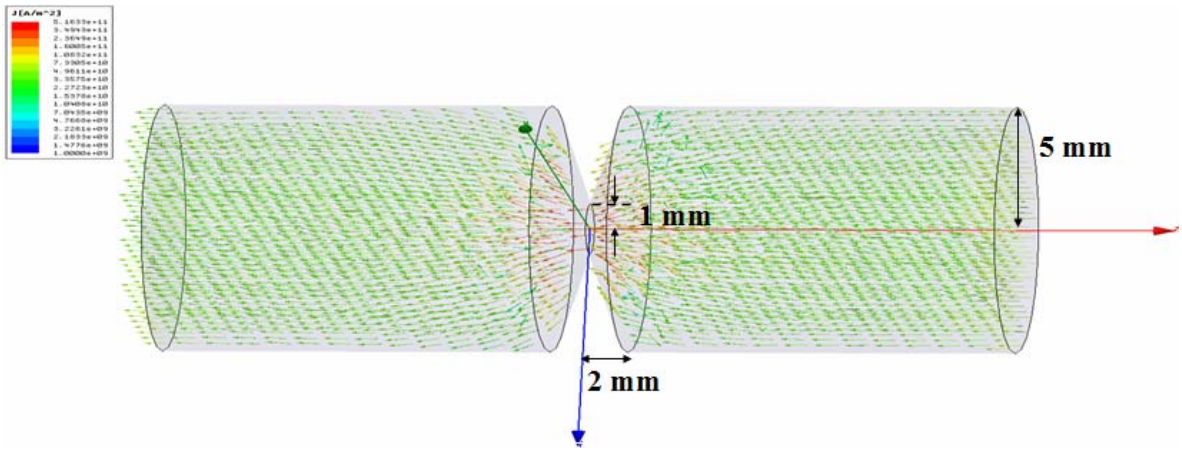

Fig. 3.15 **Maxwell 3D simulation geometry for a tungsten channel with b/a=5 and h/a=2 for a funnel connecting bridge.**

3.2 Lumped Element of Electrical Contact

The theoretical model developed in Section 3.1 concentrated on the electrostatic behavior of a single contact with rectangular, cylindrical, and funnel connecting bridge. In this section, we develop an analytic theory for the circuit lumped element parameter (*R, L, C*) for a single and multiple contacts, each with a cylindrical connecting bridge. In addition to the resistance, we will also consider the capacitance and the inductance generated by the contact. In this case, the radio frequency (RF) property of the contact can also be analyzed.

3.2.1 Theoretical Model (Single Contact Point)

To determine the lumped element circuit parameters of an electrical contact, we consider a contact with a cylindrical connecting bridge as depicted in Fig. 3.5. Due to the current, a magnetic field is generated around the contact. The resulting magnetic field produces magnetic flux, thereby generates an inductance across the contact. According to Ampere's Law [Gri99], $\oint \vec{B} \bullet d\vec{\ell} = \mu_0 I$,where I is the current enclosed by

the amperian loop, and μ_0 is the permeability of free space. The resulting magnetic field surrounding the contact is,

$$B_\theta = \frac{\mu_0 I}{2\pi r}. \tag{3.27}$$

The magnetic flux produces is,

$$\Phi = \iint \vec{B} \bullet d\vec{A} = \int_a^b B_\theta dr \int_{-h}^{h} dz = h\frac{\mu_0 I}{\pi} \ell n\left(\frac{b}{a}\right). \tag{3.28}$$

The ratio of the magnetic flux to the current give rise to an inductance ($L_c = \Phi / I$) across the connecting bridge,

$$L_c = h\frac{\mu_0}{\pi} \ell n\left(\frac{b}{a}\right). \tag{3.29}$$

In addition to the resistance and inductance, a capacitance also exists across the contact. The capacitance is $C_c = C_b + C_v$ where,

$$C_b = \varepsilon \frac{\pi a^2}{2h}, \tag{3.30a}$$

$$C_v = \varepsilon \frac{\pi(b^2 - a^2)}{2h}. \tag{3.30b}$$

C_b is the capacitance of the bridge, and C_v is the capacitance in the non-contact region [Fig. 3.16]. ε is the permittivity of the material in consideration, in our case, we take $\varepsilon = \varepsilon_0$, which represents the permittivity of free space, and a non-dielectric bridge.

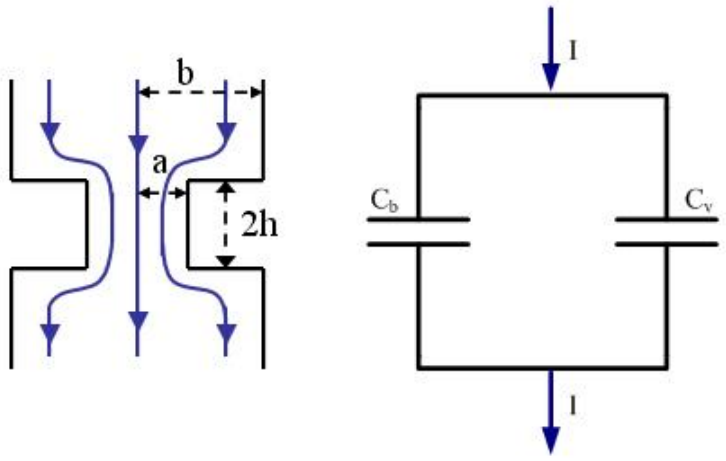

(a) **(b)**

Fig. 3.16 **Model of the capacitance of contact. (a) Cylindrical connecting bridge with channel radius *b*, constriction radius *a*, and finite axial length *2h*. (b) Circuit diagram showing the capacitance (C_b and C_v) of the electrical contact.**

The resistance, inductance and capacitance components of the contact forms a microscopic resonant parallel *RLC* circuit [Fig. 3.17], with a resonant frequency (ω_0), characteristic impedance (Z_c), and quality factor (Q) given by

$$\omega_0 = \frac{1}{\sqrt{L_c C_c}} = \frac{\sqrt{2}}{\sqrt{\varepsilon_0 \mu_0}} \frac{1}{b\sqrt{\left[1-\left(\frac{a}{b}\right)^2\right]\ell n\left(\frac{b}{a}\right)}}, \tag{3.31}$$

$$Z_c = \sqrt{\frac{L_c}{C_c}} = (377\Omega)\sqrt{\frac{2}{\pi}}\frac{h}{b}\sqrt{\frac{\ell n\left(\frac{b}{a}\right)}{1-\left(\frac{a}{b}\right)^2}}, \tag{3.32}$$

$$Q = \omega_0 R_c C_c = \frac{R_c}{Z_c}, \tag{3.33}$$

where R_c, L_c, C_c are given by Eqs. (3.21a,b), (3.29), and (3.30a,b) respectively. For the case of tungsten conducting surfaces assuming a single connecting bridge, the resulting

resistance, inductance, capacitance along with its resonant frequency, characteristic impedance, and the quality factor are given in Table 3.1.

Table 3.1: Example values of resistance, inductance, capacitance, characteristic impedance, and the quality factor of a single connecting bridge.

Tungsten resistivity	$5.6\times10^{-8}\,\Omega m$
Constriction radius (a)	$1\times10^{-6}\,m$
Channel radius (b)	$10\times10^{-6}\,m$
Constriction half-axial length (h)	$10\times10^{-6}\,m$
Resistance (R_c)	0.377Ω
Inductance (L_c)	$9.21\times10^{-12}\,H$
Capacitance (C_c)	$1.39\times10^{-16}\,F$
Resonant frequency (ω_0)	$2.79\times10^{+13}\,radian/s$
Impedance (Z_c)	$2.57\times10^{2}\,\Omega$
Quality factor (Q)	1.46×10^{-3}

Such low value of quality factor (Q) represents a non-resonant structure. The resonant frequency is in the terahertz regime [Table 3.1], therefore these asperities are extremely important for terahertz source development [Boo07].

3.2.2 Theoretical Model (Multiple Contact Points)

The theoretical model developed in the previous section represents a single contact bridge connecting two conducting channels. In this section, we develop a simple *RLC* circuit model for analyzing the *RF* contact resistance for multiple contact points.

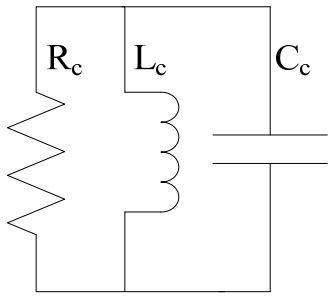

Fig. 3.17 ***RLC* circuit model of *RF* contact resistance for a single connecting bridge.**

For multiple contacting points [Fig. 3.1], we connect Fig. 3.17 in parallel as shown in Fig. 3.18,

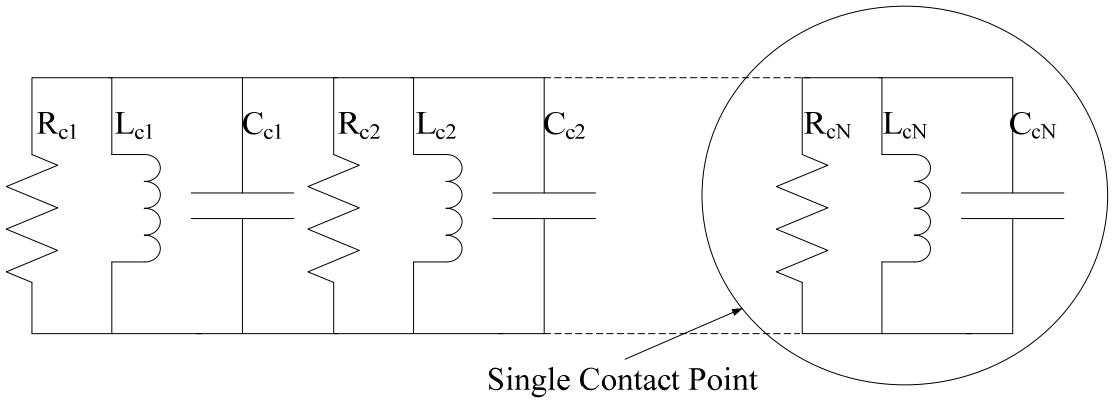

Fig. 3.18 ***RLC* circuit model of *RF* contact resistance for multiple connecting bridges.**

The circled region of Fig. 3.18 corresponds to the *RLC* circuit model of a single contact point. Therefore, the total resistance (R_{Total}), capacitance (C_{Total}), and inductance (L_{Total}) for multiple contact points is given by,

$$R_{Total} = \frac{1}{\frac{1}{R_{c1}} + \frac{1}{R_{c2}} + \cdots + \frac{1}{R_{cN}}} \approx \frac{R_{c1}}{N}, \tag{3.34}$$

$$C_{Total} = C_{c1} + C_{c2} + \cdots + C_{cN} \approx NC_{c1}, \tag{3.35}$$

$$L_{Total} = \frac{1}{\frac{1}{L_{c1}} + \frac{1}{L_{c2}} + \cdots + \frac{1}{L_{cN}}} \approx \frac{L_{c1}}{N}, \qquad \textbf{(3.36)}$$

where R_c, L_c, C_c are given by Eqs. (3.21a,b), (3.29), and (3.30) respectively. Equations (3.34) to (3.36) implies Q_{Total} and $\omega_{0_{Total}}$ are independent of N, where as $Z_{c_{Total}}$ is proportional to $1/N$.

3.2.3 RF Contact Resistance Remarks

The RF contact resistance for a single and multiple contact points has been modeled by *RLC* circuit. In general, the resistance, capacitance, and the inductance of the contacting points depend only on the radius of the constriction (*a*), radius of the channel (*b*), and the half-axial length of the constriction (*h*). In reality the exact dimensions of *a*, *b,* and *h* cannot be readily obtained experimentally, since the contact points are randomly distributed with a microscale. The resulting resistance, capacitance, and inductance are small values, and compared to experiments will be challenging. Nevertheless, the model developed allows us to determine lump parameters and the *RF* behavior of a single and multiple contacts with a cylindrical connecting bridge of the same material. The *RF* behavior of different shaped connecting bridge (for example, rectangular or funnel) can be analyzed using the procedures outlined in this section.

3.3 Statistical Analysis of Electrical Contact Resistance

The theoretical model developed in Section 3.1 represents a single contact point between two conducting surfaces. In this section, we develop a statistical analysis of electrical contact resistance with random aspect ratios of a connecting bridge.

3.3.1 Theoretical Model

We only consider contacts with cylindrical connecting bridges as shown in Fig. 3.5. The analysis assumed that the normalized distribution function for the radius of the constrictions (a), the radius of the conducting channels (b), and the half-axial length of the constrictions (h) is given by Eqs. (3.37), (3.38) and (3.39) respectively,

$$f(a) = \frac{4}{\bar{a}\sqrt{\pi}}\left(\frac{a}{\bar{a}}\right)^2 \exp\left[-\left(\frac{a}{\bar{a}}\right)^2\right], \tag{3.37}$$

$$f(b) = \frac{4}{\bar{b}\sqrt{\pi}}\left(\frac{b}{\bar{b}}\right)^2 \exp\left[-\left(\frac{b}{\bar{b}}\right)^2\right], \tag{3.38}$$

$$f(h) = \frac{4}{\bar{h}\sqrt{\pi}}\left(\frac{h}{\bar{h}}\right)^2 \exp\left[-\left(\frac{h}{\bar{h}}\right)^2\right], \tag{3.39}$$

where $\bar{a}$ is the most likely radius of the constriction, $\bar{b}$ is the most likely radius of the channel, and $\bar{h}$ is the most likely half-axial length of the constriction, and $\int_0^\infty f(a)da = 1$, $\int_0^\infty f(b)db = 1$, and $\int_0^\infty f(h)dh = 1$. The distribution function for a is shown in Fig. 3.19.

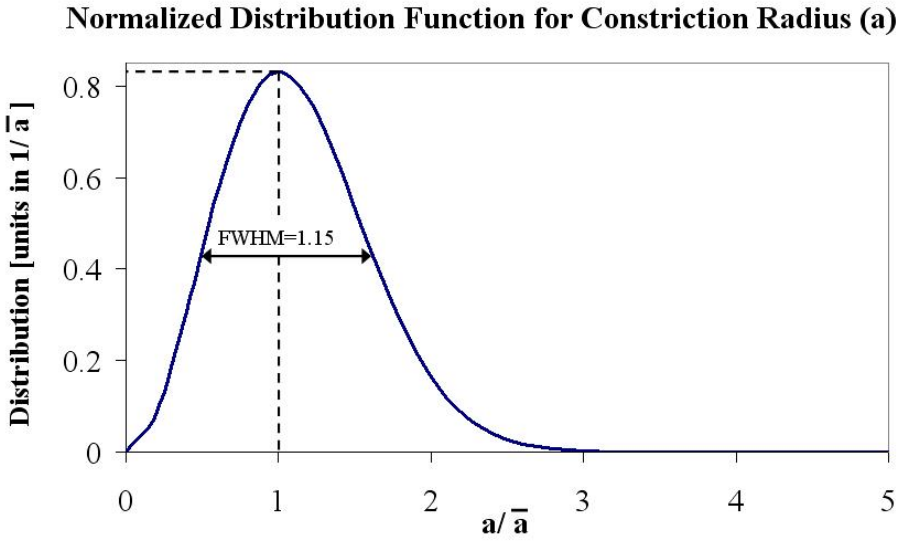

Fig. 3.19 Normalized distribution function for constriction radius (a).

The distribution functions are chosen arbitrarily, to assure convergence of the integrals as a, b approach zero [c.f. Eq. (3.25), (3.26a)]. With these distribution functions, the expectation values for resistance, inductance, and capacitance become,

$$\langle R_c \rangle = \int_0^\infty dh \int_0^\infty db \int_0^b da \left[R_c f(h) f(b) f(a) \right], \tag{3.40}$$

$$\langle L_c \rangle = \int_0^\infty dh \int_0^\infty db \int_0^b da \left[L_c f(h) f(b) f(a) \right], \tag{3.41}$$

$$\langle C_c \rangle = \int_0^\infty dh \int_0^\infty db \int_0^b da \left[C_c f(h) f(b) f(a) \right], \tag{3.42}$$

where R_c, L_c, and C_c are the resistance, inductance and capacitance for a single contact point as derived in the previous sections. Note that the integration limit for a is from 0 to b, since by definition, a (the radius of the constriction) $\leq b$ (the radius of the channel). Figure 3.20 shows the expected value of resistance, $\langle R_c \rangle$, as a function of $\bar{a}$, assuming the conducting surface is tungsten with a resistivity $\rho = 5.6 \times 10^{-8} \Omega m$, a most likely conducting channel radius $\bar{b} = 10 \times 10^{-6} m$, and the most likely half-axial length of the constriction $\bar{h} = 10 \times 10^{-6} m$. Figure 3.21 shows $\langle R_c \rangle$ as a function of $\bar{b}$, assuming a most likely constriction radius $\bar{a} = 1 \times 10^{-6} m$, with the same ρ and $\bar{h}$.

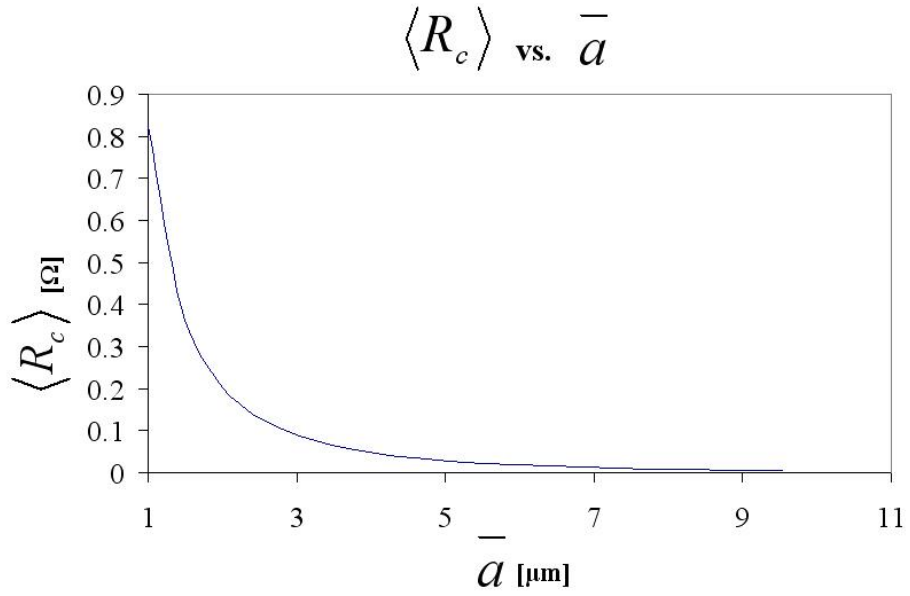

Fig. 3.20 **Expected values of contact resistance ($\langle R_c \rangle$) with different values of the most likely constriction radius ($\bar{a}$). Here $\bar{h} = 10\mu m$, $\bar{b} = 10\mu m$.**

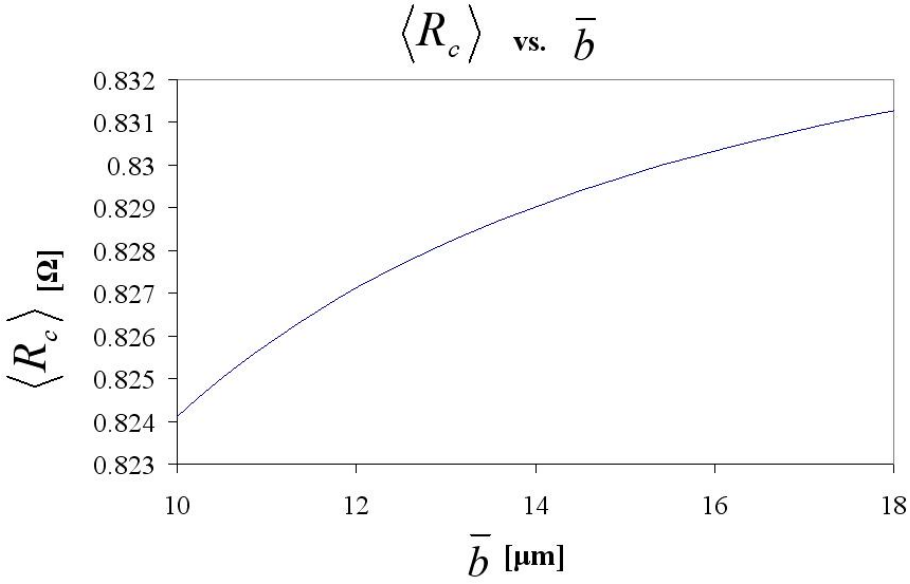

Fig. 3.21 **Expected values of contact resistance ($\langle R_c \rangle$) with different values of the most likely channel radius ($\bar{b}$). Here $\bar{h} = 10\mu m$, $\bar{a} = 1\mu m$.**

The expected value of inductance $\langle L_c \rangle$, and capacitance $\langle C_c \rangle$ for the corresponding cases are shown in Fig. 3.22 and 3.23 and Fig. 3.24 and 3.25 .

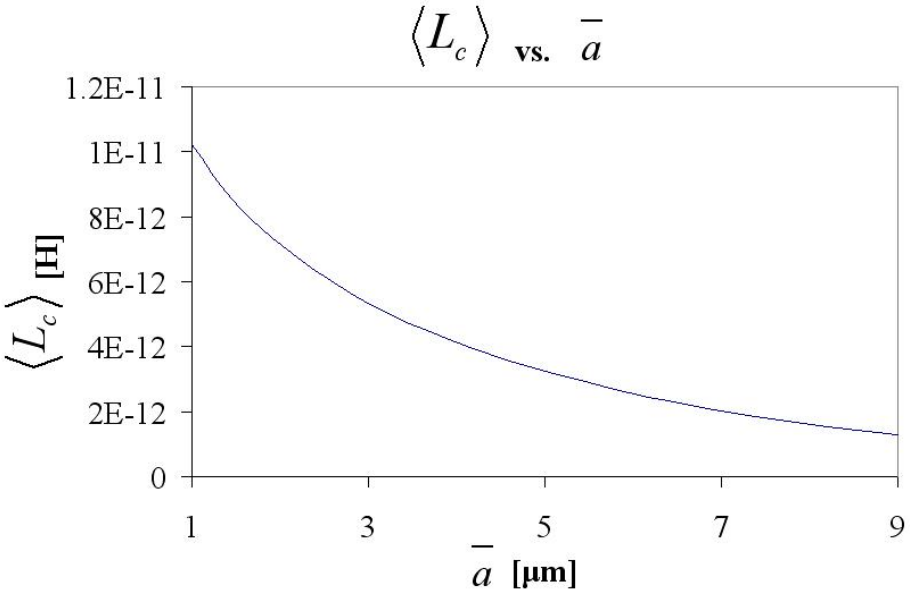

Fig. 3.22 **Expected value of inductance ($\langle L_c \rangle$) with different values of the most likely constriction radius ($\bar{a}$). Here $\bar{h} = 10\mu m$, $\bar{b} = 10\mu m$.**

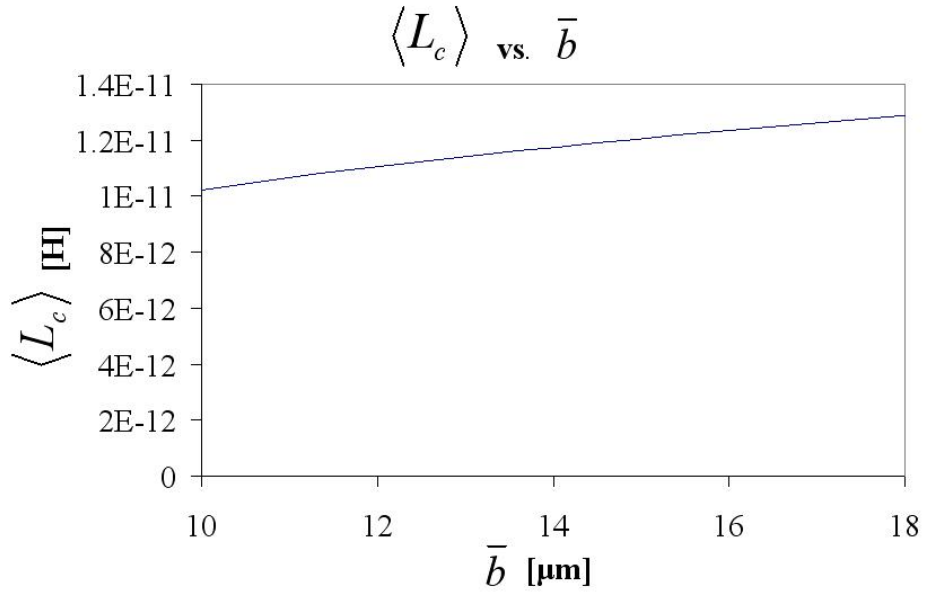

Fig. 3.23 **Expected value of inductance ($\langle L_c \rangle$) with different values of the most likely channel radius ($\bar{b}$). Here $\bar{h} = 10\mu m$, $\bar{a} = 1\mu m$.**

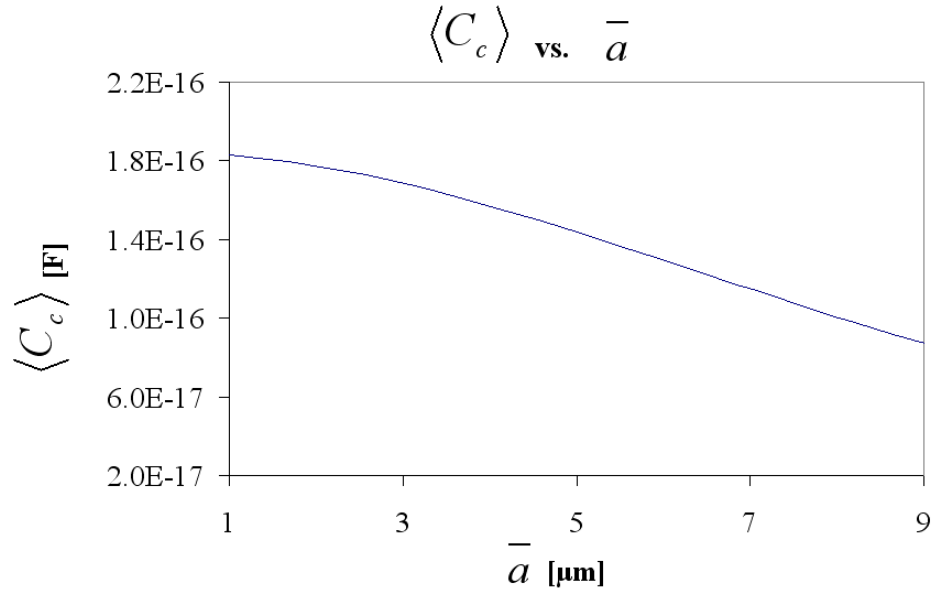

Fig. 3.24 **Expected values of capacitance ($\langle C_c \rangle$) with different values of the most likely constriction radius ($\bar{a}$). Here $\bar{h} = 10\mu m$, $\bar{b} = 10\mu m$.**

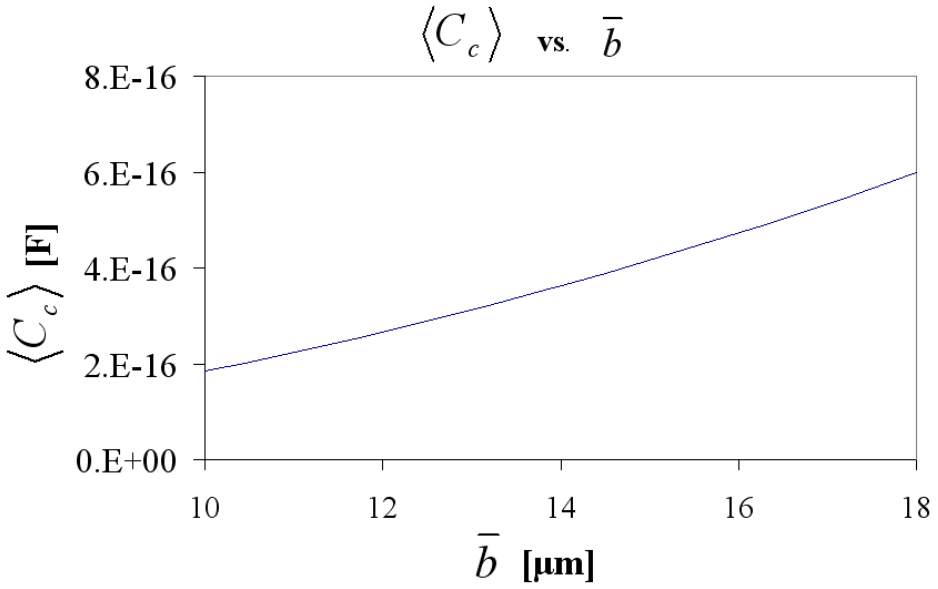

Fig. 3.25 **Expected values of capacitance ($\langle C_c \rangle$) with different values of the most likely channel radius ($\bar{b}$). Here $\bar{h} = 10\mu m$, $\bar{a} = 1\mu m$.**

3.4 Comparison with UM Z-pinch Experiment

An experiment was performed by Gomez, Zier, and French [Gom08] from the University of Michigan Plasma, Pulsed Power, and Microwave Laboratory to investigate the effect of contact resistance on the energy deposition, and plasma expansion profile in a wire array Z pinch. The experimental configuration is shown in Fig. 3.26.

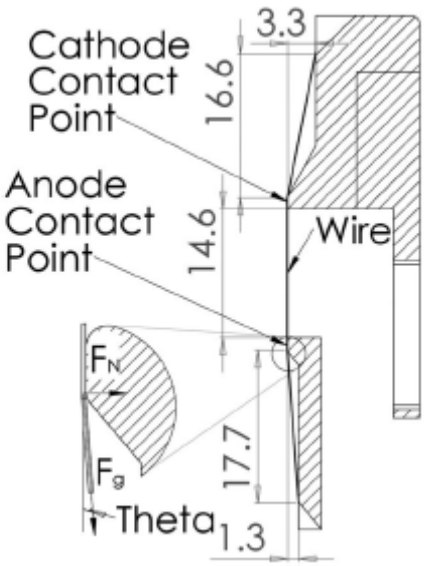

Fig. 3.26 **Wire holder for the Z-pinch experiment. Wire material is aluminum. F_N is the normal force pressing the wire against the electrode. The angle θ (theta) is 4.2° for the anode and 11.2° for the cathode [from Gom08].**

The wire material is Aluminum (*Al*) 5056 of 13 μm in diameter. The same weight is used on the anode and cathode end to maintain the wire tension and the contact between the wire and the electrodes. However, due to the difference in θ, the normal force at the cathode is approximately three times that at the anode. The electrode contact area was sanded with 1500 grit sandpaper and cleaned with acetone. Electrical tape was used to insulate all points of contact, except at the intended contact region [Gom08].

The calculated resistance of the *Al* 5056 wire is 6.5 Ω based on the resistivity, length, and diameter of the wire. The contact resistance was found by subtracting the

wire resistance from each of the measured load resistance. The average contact resistance depends on the weight used. For the 0.4 g and the 0.89 g wire weight case, the average contact resistance is found to be 3420 Ω and 896 Ω respectively. Increasing the wire weight mass to 1.34 g reduced the contact resistance to 86 Ω [Gom08]. Therefore, on average the contact resistance from experiment was found to be in the range of 10s to 1000s ohms.

In order to compare the theory with the experiment, we assume the contact point between the wire and electrode has cylindrical geometry. We first calculate the contact resistance assuming a single contact point. Thus, we can apply Eqs. 3.20 and 3.21 to estimate the theoretical value of the contact resistance. Typically value of b/a = 10 to 100, and value of h/a also has similar range. The typical value of constriction dimension is in the range of microns [Rin99]. In this case, we assume the constriction dimension $a = 1\mu m$, and the resistivity of aluminum is $\rho = 2.8 \times 10^{-8} \Omega m$. The resulting contact resistance of a single contact point is calculated to be in the range of 0.377 Ω to 3.6 Ω according to Eqs. 3.20 and 3.21, which is substantially lower than the experimental measured values of 10s to 1000s ohms. In order to obtain the range of measured contact resistance, we have to assume the constriction dimension a in the nanometer scale. By assuming $a = 10nm$ (which is substantially smaller than what we expect), with a typically value of b/a =10 to 100, and h/a with similar range. The resulting contact resistance is calculated to be in the range of 37 Ω to 360 Ω, which falls in the range of the measured values. But then there is only one contact point to give rise to this large resistance. The theory developed thus fails to explain the measured values of contact resistance. The high values of contact resistance measured experimentally are likely due to the oxide effect that exists in the real contact, which our theory ignored.

3.5 Conclusion

In this chapter, we extended Holm's contact resistance theory to include a finite axial length in the direction of current flow. We derive the analytic result of contact resistance in a rectangular connecting bridge, and extend our theory to include a straight cylinder and funnel shape connecting bridge. Our results for the latter cases are accurate to within one percent when compared with electrostatic code. Effects of finite bridge length for other geometries, e.g., non-circular and ring a-spot [Nak93, Tim99], may similarly be constructed following our procedures as discussed in Section 3.1. In addition, we have developed a theoretical model to determine the lumped element, and to analyze the *RF* effect on the electrical contact. The *RF* contact resistance of single contact point can be modeled as a *RLC* circuit [Fig. 3.17]. In reality, the exact dimensions (for example a, b, and h) of a single contacting site cannot be easily determined experimentally. The statistical treatment gives an educated estimate of the resulting contact resistance, inductance and capacitance. The UM Z-pinch experiment conducted by Gomez, Zier and French concluded that the contact resistance is in the range of 10s to 1000s of ohms [Gom08]. Oxide effect (which our theory ignores) may be playing an important role in the experiment that increases the contact resistance to much higher values than the theory predicted.

CHAPTER 4

CONCLUSIONS

In this thesis, we investigate two contemporary issues of Z-pinches. These issues are motivated by both simulations and on-going experiments. They concern the azimuthal clumping instability in a discrete wire array, and the electrical contact resistance. In the following sections, we will summarize our novel results. Suggestions for future works will also be given.

4.1 On the Linear and Nonlinear Evolution of the Azimuthal Clumping Instability

4.1.1 Novel Results

We concentrate on the linear and nonlinear evolution of the most unstable azimuthal clumping mode, the π mode, in an array of N discrete wires. It is recognized that the simulation of this mode may be achieved by simulation of only one wire, over a wedge with reflection conditions imposed on the wedge boundaries. In Chapter 2, the linear and nonlinear growth was analytically computed, displaying the regimes where collective interactions and single wire interactions become dominant. While the analytic theory was developed for a linear array of infinitesimally thin wire, it turns out that the theory provides a fairly accurate description when it is compared with ALEGRA simulations of a circular array of wires of finite wire radius. The theory also compares well (impact time calculation) with few-wire array in a circuit simulation model, REIN. The general conclusion is that the π mode of discrete wires may undergo significant

clumping before appreciable radial motion sets in. Thus, absence of azimuthal clumping of wires in comparison with the wires' radial motion may imply substantial lack of wire currents. While the present theory and simulations have ignored the plasma corona and axial variations, it is argued that their effects, and the complete account of the three-dimensional feature of the pi-mode, together with a scaling study of the wire number, may be expediently simulated by using only one single wire in an annular wedge with a reflection condition imposed on the wedge's boundary [Fig. 2.2].

4.1.2 Suggestions for Future Work

Interesting areas of future work include investigation of whether the plasma corona is subject to the clumping instability. Intuitively, a plasma corona may be considered as a collection of minute current-carrying filaments lumped together in some continuum limit, and this scenario suggests that tendency toward clumping should prevail. This intuition is partially supported by Hu's recent experiments at Cornell University [Hu05], where few-wire (typically four) linear arrays were studied in great detail. She found that the plasma coronas from the four wires did converge, in spite of the action of a single return current post, whose magnetic field would push the plasma coronas from each wire further *apart*. (The return current post was located behind the wire array). This may then be taken as evidence that the plasma coronas were carrying substantial current and their mutual attractions led to their convergence. However, the situation is more complicated. For example, there also exists experimental evidence [Str06] that the pressure of coronal plasmas from two neighboring wires may force the two coronal plasmas apart, in spite of the mutual attraction of the currents which these two coronal plasmas presumably carry. These effects may be assessed with the 1-sector simulation of the π mode as illustrated in Fig. 2.2, by including the effects of the coronal

plasma, as such a 1-sector simulation also covers the single-wire interaction when the wires in a pair are close to each other.

The clumping (Jeans) instability may acquire rather different characteristics in the flowing coronal plasma. For example, the substantial thickness of the plasma corona (compared with the original wire size) is expected to have a stabilizing influence according to the concept of "plasma reduction factor" in the dynamics of electron sheets [Cho64] and of self-gravitating disks [Shu68]. Without an explicit specification of the current profile in the plasma corona, one can no longer identify the azimuthal mode number (and possibly the radial mode number) of the most unstable mode. The radial Rayleigh-Taylor instability, which is absent in the *metallic wire* array, but which might occur in the radially imploding *plasma* corona, may also mask or couple to the azimuthal instability that is studied in this paper. Once more, the state of the core material, how much current is returned to the cores, and when the current returns, is much in debate. If there are discrete, current-carrying elements to be found in the original core positions at some late time, and if the current in these elements is high enough to move the mass onto the array axis, then some azimuthal clumping motion should be detectable. However, even in this case, observing the clumping may be very difficult, as there is usually much dense plasma present late in wire array implosions that tends to obscure individual wires in radiograph images [Sin05]), and the wire cores themselves are usually significantly expanded [Leb05, Sin05], in addition to the various dynamical roles that the plasma corona would have played. Nevertheless, the simulation of all of these features may still be analyzed using the 1-sector simulation of a single wire with reflection boundary condition, even if the corona plasmas and axial perturbations are present.

The present author has attempted a 1-section simulation using ALEGRA trying to sort out the effect of the clumping instability on plasma. Two different ALEGRA

simulation geometries were set up: (a) the plasma is circular in shape, and (b) the plasma is elongated in shape. In both cases, preliminary results show mitigation of clumping instability with the replacement of discrete wire with plasma. However, more simulations and studies need to be conducted in order to solidify such a claim, as a simulation which includes plasma becomes more complicated, for example, the inclusion of radiation hydrodynamics become necessary for the simulation to be meaningful.

4.2 On A Higher Dimensional Theory of Electrical Contact Resistance

4.2.1 Novel Results

In Chapter 3 of this thesis, we extended Holm's classical contact resistance theory to include a finite axial length in the direction of current flow. The contact resistance depends on two dimensionless geometric parameters, *b/a* and *h/a*, measuring the cross-sectional size of the connecting bridge and its axial length. We derive the analytic result of contact resistance in a rectangular connecting bridge, and extend our theory to include a straight cylinder and funnel shape connecting bridge. In all three cases, the bridge has a total length of *2h*. The effect of finite *h* is found to increase the contact resistance linearly with *h*, by an amount that is expected from the increase in the current path length associated with finite *h*, and from the decrease in the cross-sectional area in the channel constriction. Our results for the latter cases are accurate to within one percent when compared with electrostatic code.

One of the main advantages of our work is that we have decoupled the problem of change of the contact resistance in response to an applied pressure. Once we know how the geometrical dimension changes with pressure, e.g., how h/a and b/a changes with a given pressure, the resulting contact resistance can easily be determined using the results that we have obtained.

A statistical theory accounting for distributions of size and axial length of the connecting bridges have been developed. The equivalent circuit elements (R, L, C) characterizing the electrical contact have also been computed.

The present theory, while appealing, fails to explain the high values of contact resistance measured at the U of M Z-pinch experiments [Gom08].

4.2.2 Suggestions for Future Work

Interesting areas of future work include extensions of the theory to include: (a) channels and bridges of dissimilar materials, especially to account for the role of oxide, (b) ohmic heating at such contacts, and (c) contact resistance in terms of the deformations in response to pressure. In addition, it is interesting to note that the results obtained in this thesis may be applied to many different areas, one such area include using the theory developed to assess the additional pressure required to maintain a laminar fluid flow that encounters a local constriction of various geometries, e.g., blood flow in a partially blocked artery.

APPENDICES

Appendix A

Most Unstable Clumping Mode in an Infinite Linear Wire Array

In this Appendix, we outline the proof to show that the most unstable clumping mode in an infinite linear wire array is also the π mode, where neighboring wires are 180 degrees out of phase with each other. Consider an infinite linear wire array [Fig. 2.3a]. In the Cartesian model, since the x-directed (radial) motion is stable and is decoupled from the y-directed (azimuthal) motion, we concentrate only on the y-directed (azimuthal) displacement of the zeroth wire, $\xi_0(t)$ [Fig. 2.3b]. The (x,y) coordinates of the n-th wire is (0, nd) in equilibrium, and is (0, nd+ ξ_n) with perturbation from its equilibrium position. In a periodic structure, $\xi_{n+1} = \xi_n e^{-j\theta}$ according to the Floquet theorem, where θ is an arbitrary constant. Therefore ξ_n is related to ξ_0 as follows,

$$\xi_n = \xi_o e^{-jn\theta}, \quad n = \pm 1, \pm 2. \cdots \qquad \textbf{(A1)}$$

The distance from the n-th wire to the 0-th wire is,

$$dn = \left| nd + \xi_n - \xi_0 \right|. \qquad \textbf{(A2)}$$

The force per unit length on the zeroth wire, by the parallel current on the n-th wire at a distance d_n [Fig. 2.3b], is easily shown to be $\mu_0 {I_w}^2 / (2\pi d_n)$ in magnitude by the Biot-

Savart law, where d_n is given by Eq. (A2). The force on the zeroth wire is the sum of the attractive forces from all other wires, each carrying a current in the same direction. This resultant force leads to the following equation of motion for $\xi_0(t)$,

$$\ddot{\xi}_0 = \frac{\mu_o I_w^{\,2}}{2\pi m_L}\left[\sum_{n=1}^{\infty}\frac{1}{\left|nd+\xi_n-\xi_0\right|}-\sum_{n=-1}^{-\infty}\frac{1}{\left|nd+\xi_n-\xi_0\right|}\right], \qquad \textbf{(A3)}$$

where ξ_n is given by Eq. (A1) and a dot ($\bullet$)denotes d/dt. I_w is the wire current, and m_L is the mass per unite length of each wire. The first (second) infinite sum represents the force due to the $n > 0$ ($n < 0$) wires. Linearize to first order in ξ_0, Eq. (A3) becomes, upon using Eq. (A1),

$$\ddot{\xi}_0 \cong \frac{\mu_o I_w^{\,2}}{2\pi m_L}\sum_{n=1}^{\infty}\frac{2\xi_0\left[1-\cos(n\theta)\right]}{(nd)^2} \equiv \gamma^2\xi_0\,, \qquad \textbf{(A4)}$$

where γ represents the linear growth rate of the azimuthal clumping instability in an infinite linear array:

$$\gamma = \gamma(\theta) = \sqrt{\frac{\mu_o I_w^{\,2}}{2\pi m_L}\sum_{n=1}^{\infty}\frac{2\left[1-\cos(n\theta)\right]}{(nd)^2}} = C\sqrt{\sum_{n=1}^{\infty}\frac{\left[1-\cos(n\theta)\right]}{n^2}} = C\sqrt{\frac{\pi\theta}{2}\left(1-\frac{\theta}{2\pi}\right)}\,. \qquad \textbf{(A5)}$$

$$C = \sqrt{\frac{\mu_o I_w^{\,2}}{\pi m_L d^2}}\,, \qquad \textbf{(A6)}$$

where we have used the following identities [Gra00].

$$\sum_{n=1}^{\infty}\frac{1}{n^2} = \frac{\pi^2}{6}\,, \qquad \textbf{(A7)}$$

$$\sum_{n=1}^{\infty}\frac{\cos(n\theta)}{n^2} = \frac{\pi^2}{6}-\frac{\pi\theta}{2}+\frac{\theta^2}{4}\,. \qquad \textbf{(A8)}$$

It is easy to show from Eq. (A5) that γ is maximized at $\theta = \pi$, at which $\gamma(\pi) = C\frac{\pi}{2}$, and

$$\frac{\gamma(\theta)}{\gamma(\pi)} = \sqrt{\frac{2\theta}{\pi}\left(1 - \frac{\theta}{2\pi}\right)}. \qquad \textbf{(A9)}$$

Appendix B

Derivation of the Governing Eqs. (2.4) and (2.8)

This Appendix outlines the derivation of the governing Eq. (2.4), and shows that its normalized form, Eq. (2.8), is approximately valid even if the wire current (I_w) is time-varying.

The force per unit length on the zeroth wire, by the parallel current on the n-th wire at a distance d_n [Fig. 2.3b], is easily shown to be $\mu_0 I_w^2/(2\pi d_n)$ in magnitude by the Biot-Savart law, where $d_n = |nd + \xi_n - \xi_0|$. The force law Eq. (A3) for the zeroth wire then reads, for the π-mode,

$$\ddot{\xi}_0 = \frac{\mu_0 I_w^2}{2\pi m_L}\left[\sum_{n=1}^{\infty}\frac{1}{|nd+(-1)^n\xi_0-\xi_0|}-\sum_{n=-1}^{-\infty}\frac{1}{|nd+(-1)^n\xi_0-\xi_0|}\right], \qquad \textbf{(B1)}$$

where the first (second) infinite sum represents the force due to the $n > 0$ ($n < 0$) wires and we have used Eq. (2.3). From Eq. (B1), it is clear that the even terms of n do not contribute. Retaining only the odd terms in n, Eq. (B1) becomes,

$$\ddot{\xi}_0 = \left(\frac{2\mu_0 I_w^2}{\pi m_L d^2}\xi_0\right)\sum_{n=1,odd}^{\infty}\frac{1}{n^2-(2\xi_0/d)^2} = \left(\frac{2\mu_0 I_w^2}{\pi m_L d^2}\xi_0\right)\left(\frac{\pi^2}{8}\right)\frac{\tan(\pi\xi_0/d)}{(\pi\xi_0/d)}, \qquad |2\xi_0/d|<1, \qquad \textbf{(B2)}$$

which is Eq. (2.4). The last equality in Eq. (B2) is easily established.

If the wire current is time-varying, so is γ_p in Eq. (2.4), which may be written as

$$\frac{d^2 f}{dt^2} = \gamma_p^2(t) \tan f \quad , \tag{B3}$$

where $f = \pi\xi_0/d$. If we make the transformation from t to τ,

$$\tau = \int_0^t dt \gamma_p(t) \quad , \tag{B4}$$

and assume that γ_p changes slowly over the time scale of $1/\gamma_p$, then under the eikonal approximation, Eq. (B3) reads

$$\frac{d^2 f}{d\tau^2} = \tan f \quad , \tag{B5}$$

which is Eq. (2.8) of the main text. To see this, consider the $f << 1$ limit, where $\tan(f) \sim f$. The independent solutions to Eq. (B5) are e^{τ} and $e^{-\tau}$, which are indeed the eikonal solution to Eq. (B3) in this $f << 1$ limit.

Multiply Eq. (B5) by $df/d\tau$, and integrate from $\tau = 0$. This readily yields

$$\frac{df}{d\tau} = \sqrt{u_i^2 - 2\ell n\left(\frac{\cos f}{\cos f_i}\right)} \quad , \tag{B7}$$

where the constant of integration is adjusted so that at $\tau = 0$, $f = f_i$ and $df/d\tau = u_i$. Integration of Eq. (B7) immediately yields Eq. (2.10) of the main text, which is the exact solution to Eq. (2.8) subject to the initial condition Eq. (2.9).

Appendix C

Approximate solution of the wire trajectory in the π mode

In this appendix, we derive the approximate trajectory of the zeroth wire in the π mode, together with the approximate impact time for a wire pair to coalesce from the initial position.

Let Δr be the change in the zeroth wire's radius from its initial position in a cylindrical array. Since the radial motion is stable, the radial force law is simply,

$$\frac{d^2\Delta r}{dt^2} = -g = -\frac{2d}{\pi}\gamma_p^2(t) \ , \qquad \textbf{(C1)}$$

where we have used Eqs. (2.1) and (2.5). In terms of the normalized radial displacement, $\Delta\rho = \pi\Delta r/d$ and the normalized time τ defined by Eq. (B4), Eq. (C1) may be rewritten in the eikonal approximation,

$$\frac{d^2\Delta\rho}{d\tau^2} = -2 \ , \qquad \textbf{(C2)}$$

whose solution is simply $\Delta\rho = -\tau^2$ for zero initial radial displacement and zero initial radial velocity. Since τ is related to the normalized azimuthal displacement, $f = \pi\xi_0/d$, by Eq. (2.10), the r–θ trajectory of the zeroth wire then reads,

$$\Delta\rho = -\tau^2(f) \ , \qquad \textbf{(C3)}$$

which is Eq. (2.15).

The wire pair merges when $f = \pi/2$, at the normalized time $\tau_m = \tau(\pi/2)$, and at the normalized radial displacement $\Delta\rho_m = -\tau_m^2$, where from Eq. (2.12),

$$\tau_m = \int_{f_i}^{\pi/2} dy \left[u_i^2 - 2\ell n\left(\frac{\cos y}{\cos f_i} \right) \right]^{-1/2} . \qquad \textbf{(C4)}$$

Let us now set $u_i = 0$ and change the variable, $x = \cos y/\cos f_i$, to write Eq. (C4) as,

$$\tau_m = (\cos f_i) \int_0^1 \frac{dx}{\sqrt{-2\ell n(x)}\sqrt{1 - x^2 \cos^2 f_i}} . \qquad \textbf{(C5)}$$

As $f_i \to \pi/2, \quad \cos f_i \approx (\pi/2 - f_i) \to 0$ and we may set the factor $x^2\cos^2 f_i$ in Eq. (C5) equal to zero to first order in $\cos f_i$. The reduced integral in (C5) may then be easily evaluated with a change of variable $z = \sqrt{-2\ell n(x)}$, and that reduced integral in z has the value $(\pi/2)^{1/2}$. Thus, we arrive at the asymptotic formula,

$$\tau_m \cong \sqrt{\frac{\pi}{2}} \left(\frac{\pi}{2} - f_i \right), \quad f_i \to \frac{\pi}{2} , \qquad \textbf{(C6)}$$

which is Eq. (2.14) of the main text.

As $f_i \to 0, \quad \cos f_i \approx 1 - f_i^2/2$, and the integral (C5) diverges at the upper limit of integration, $x = 1$. To see this, we may use the following formulas in Eq. (C5),

$$-\ell n(x) \approx 1 - x, \quad x \to 1 , \qquad \textbf{(C7)}$$

$$1 - x^2 \cos^2 f_i \approx 1 - x^2 + x^2 f_i^2 \approx 2(1-x) + f_i^2, \quad x \to 1, f_i \to 0 . \qquad \textbf{(C8)}$$

The integral (C5) then readily shows divergence at the upper limit, $x = 1$, if f_i vanishes. This integral converges at the lower limit, $x = 0$, however. Therefore, to find the rate at which the integral (C5) diverges for $f_i << 1$, we focus on the upper limit. Upon substituting (C7) and (C8) into (C5), we approximate (C5) as,

$$\tau_m \sim \frac{1}{2}\int_0^1 \frac{dx}{\sqrt{1-x}\sqrt{1-x+f_i^2/2}} \quad . \tag{C9}$$

Let $z = (1-x)/\varepsilon$, where $\varepsilon = f_i^2/2$. Equation (C9) reads, upon expanding its integrand for large z,

$$\tau_m \sim \frac{1}{2}\int_0^{1/\varepsilon} \frac{dz}{\sqrt{z}\sqrt{1+z}} \sim \frac{1}{2}\int^{1/\varepsilon} \frac{dz}{z}\left[1+O\left(\frac{1}{z}\right)\right] \sim \frac{1}{2}\left[\ell n\left(\frac{1}{\varepsilon}\right)+C+O(\varepsilon)\right], \tag{C10}$$

where C is the constant arising from the lower limit of integration in (C10), which we shall determine by matching Eq. (C10) with the numerical integration of Eq. (C5). Using this constant, and the definition of ε, Eq. (C10) becomes

$$\tau_m \cong \ell n\left(\frac{1}{f_i}\right)+1.04+O\left(f_i^2\right), \qquad f_i << 1, \tag{C11}$$

which is Eq. (2.13) of the main text.

Appendix D

Input deck for ALEGRA simulation

Input deck for 200 wires

```
$ Aprepro ($Revision: 1.71 $) Mon Apr 14 11:33:03 2003
$$$$$$$$$$$$$$$$$$$$$$$$$$$  PROBLEM COMMENTS
$$$$$$$$$$$$$$$$$$$$$$$$$$$$
$
$ NAME:           Wire clumping instability (eulerian)
$
$ PHYSICS:  MAGNETOHYDRODYNAMICS
$
$ BOUND. COND:    PERIODIC BOUNDARIES FOR WEDGE FACES
$
$ AUTHORS:  E. Yu, Christopher Garasi (SNL; 9231) & Bryan Oliver (MRC)
$           modified by W.W. Tang
$ DATE:           3/4/2006
$
$ APREPRO definitions:
$ units are assumed to be in microns
$
$ ___________________constants ____________________________
$ { one_ev} = 1.16e4}
$ { unit_conv = 1.0e-6}

$ { tmax = 55.0e-9}
$ { yoffset = 3.0e-5}
$ _____________________USER VARIABLES_____________________

title: 2D XY periodic-wire sweep problem

units, si
$start time = 2.368e-6
double precision exodus

$termination time 2.65e-6
termination time {tmax}
$termination cycle 2
$read restart dump, -1

$$$$$$$$$$$$$$$$$$$$$$$$$  physics options
$$$$$$$$$$$$$$$$$$$$$$$$$$$$
$
$          MHD parameters
$

magnetohydrodynamics

  detailed energy tallies
```

```
$  max vol change 0.05

  dynamics
    material fraction force limit,  0.6, power 1.0
  end

  transient magnetics
$ outer boundary
$ for 60 kA per wire, total current should be 21.6 MA
    xy cylindrical radial slot bc, sideset 300, function 1, scale 1.0,
    X 0.0, Y 0.0

    void conductivity 1.0e-4
     ztec set, 1
    JOULE HEAT, NOHEAT
    MAGNETIC FORCE, TENSOR
    A REZONE, CT VAN LEER
    ALFVEN VELOCITY MAX, 1.0e6
    include “3_8MA.dat”
  end

  hydrodynamics
    no displacement, nodeset 100 NORMAL, X -1.570731731e-2 Y
9.998766325e-1
    no displacement, nodeset 200 NORMAL, X -1.570731731e-2 Y -
9.998766325e-1
    no displacement, nodeset 400, X
    no displacement, nodeset 400, Y
  end

  gradual startup factor, 0.3
  time step scale, 0.9

  $$ DIATOM INSERTION COMMANDS
  diatoms
   package ‘wire_mat’
    material =  11
    density 2700.0
    temperature 300.
    Numsub = 10
    insert circle
     center 0.01 {yoffset}
     radius 10.0e-06
    endinsert
   endpackage

  enddiatoms

$$ BLOCK INPUT
  block 1   $ square containing wire
   eulerian mesh
   add diom input
  end
  block 2   $ between square and innermost block
    eulerian mesh
  end
  block 3   $ innermost block
    eulerian mesh
  end
  block 4   $ outer void
    eulerian mesh
```

```
end


$$ TRACERS
  tracer points
   lag tracer 1, x = 0.01, y = {yoffset}         $ core center
  end

end


$$$$$$$$$$$$$$$$$$$$$$$$  execution control
$$$$$$$$$$$$$$$$$$$$$$$$$$


emit output: time  = 1.0E-9, from 0. to 1.
$emit plot: time interval   = 1.0e-10, from 0. to 2.372e-6
$emit plot: time interval   = 1.0e-9, from 2.372e-6 to 2.7e-6
emit plot: time interval = 1.0e-9
emit screen: cycle  = 50
$emit hisplt: time interval 1.0e-9
emit hisplt: cycle interval = 5
emit restart: time interval = 1.0e-9

Plot variable
  AZ
  JZ
  B
$ avg is needed for multimaterial calculations
  density, avg
  temperature, avg
  pressure, avg
  sound speed, avg
  velocity
  econ
  ZBAR
  specific_heat_vol, avg
  energy, avg
end

$$$$$$$$$$$$$$$$$$$$$$$$  algorithm control
$$$$$$$$$$$$$$$$$$$$$$$$$$

$$ ML setup
 ztec 1     $ mag control
   solver,    cg          $ default = cg
   scaling,   sym_diag    $ default = sym_diag
   conv norm, rhs         $ default = r0
   tol,       1.e-13       $ default = 1.e-5
   output, none
   multilevel
     fine sweeps = 5
     fine smoother = GAUSS SEIDEL
     coarse sweeps = 1
     coarse smoother = lu
     multigrid levels = 10
     interpolation algorithm = AGGREGATION
   end
end
```

```
$$$$$$$$$$$$$$$$$$$$$$  material models
$$$$$$$$$$$$$$$$$$$$$$$$$$$$$$
material 11       WIRE
  model = 11          $ EOS                            (KERLEY ANEOS)
  model = 12          $ electrical conductivity        (EC/TC LMD)
  model = 13          $ elastic plastic
end


$ ----------------- Al models ------------------------------

 model 11 keos sesame          $ al eos data
   feos  = 'sesame'
   neos  = 3700
   clip = 200.0                  $ temperature cutoff T+/- clip at EOS
boundary
 end

 model 12 lmd                  $ al electrical/thermal conductivity
   tuned aluminum
   z = 13.00
   a = 26.98
   rho solid = 2.70e+3         $ kg/m**3
   ec mult = 1.0
   tc mult = 1.0
   temp cutoff = 10.0          $ temperature in Kelvin
 end

 model 13 elastic plastic        $ elastic plastic parameters (manual)
   youngs modulus = 73.00e+13     $ pascals (1 pascal = 10 dyne/cm**2)
   poissons ratio = 0.3225
   yield stress   = 2.76e+08     $ pascals
   hardening modulus = 1.24e+08  $ pascals
   beta              = 1.
 End


exit
```

Input deck for 360 wires

```
$ Aprepro ($Revision: 1.71 $) Mon Apr 14 11:33:03 2003
$$$$$$$$$$$$$$$$$$$$$$$$$$$$  PROBLEM COMMENTS
$$$$$$$$$$$$$$$$$$$$$$$$$$$$$$
$
$ NAME:           Wire clumping instability (eulerian)
$
$ PHYSICS:  MAGNETOHYDRODYNAMICS
$
$ BOUND. COND:    PERIODIC BOUNDARIES FOR WEDGE FACES
$
$ AUTHORS:  E. Yu, Christopher Garasi (SNL; 9231) & Bryan Oliver (MRC)
$           modified by W.W. Tang
$ DATE:           3/4/2006
$
$ APREPRO definitions:
$ units are assumed to be in microns
$
$ ___________________constants ________________________________
```

```
$ { one_ev} = 1.16e4}
$ { unit_conv = 1.0e-6}

$ { tmax = 40.0e-9}
$ { yoffset = 3.0e-5}
$ _____________________USER VARIABLES_____________________

title: 2D XY periodic-wire sweep problem

units, si
$start time = 2.368e-6
double precision exodus

$termination time 2.65e-6
termination time {tmax}
$termination cycle 2
$read restart dump, -1

$$$$$$$$$$$$$$$$$$$$$$$$  physics options
$$$$$$$$$$$$$$$$$$$$$$$$$$$$$
$
$          MHD parameters
$

magnetohydrodynamics

  detailed energy tallies

$  max vol change 0.05

  dynamics
    material fraction force limit,  0.6, power 1.0
  end

  transient magnetics
$ outer boundary
$ for 60 kA per wire, total current should be 21.6 MA
    xy cylindrical radial slot bc, sideset 300, function 1, scale 1.0,
    X 0.0, Y 0.0

    void conductivity 1.0e-4
    aztec set, 1
    JOULE HEAT, NOHEAT
    MAGNETIC FORCE, TENSOR
    A REZONE, CT VAN LEER
    ALFVEN VELOCITY MAX, 1.0e6
    include "7MA.dat"
  end

  hydrodynamics
    no displacement, nodeset 100 NORMAL, X -8.726535e-3 Y  9.999619e-1
    no displacement, nodeset 200 NORMAL, X -8.726535e-3 Y -9.999619e-1
    no displacement, nodeset 400, X
    no displacement, nodeset 400, Y
  end

  gradual startup factor, 0.3
  time step scale, 0.9

  $$ DIATOM INSERTION COMMANDS
  diatoms
```

```
   package 'wire_mat'
    material =  11
    density 2700.0
    temperature 300.
    numsub = 10
    insert circle
     center 0.01 {yoffset}
     radius 10.0e-06
    endinsert
   endpackage

  enddiatoms

$$ BLOCK INPUT
  block 1   $ square containing wire
   eulerian mesh
   add diom input
  end
  block 2   $ between square and innermost block
    eulerian mesh
  end
  block 3   $ innermost block
    eulerian mesh
  end
  block 4   $ outer void
    eulerian mesh
  end


$$ TRACERS
  tracer points
   lag tracer 1, x = 0.01, y = {yoffset}         $ core center
  end

end


$$$$$$$$$$$$$$$$$$$$$$$$  execution control
$$$$$$$$$$$$$$$$$$$$$$$$$$$


emit output: time  = 1.0E-9, from 0. to 1.
$emit plot: time interval   = 1.0e-10, from 0. to 2.372e-6
$emit plot: time interval   = 1.0e-9, from 2.372e-6 to 2.7e-6
emit plot: time interval = 1.0e-9
emit screen: cycle  = 50
$emit hisplt: time interval 1.0e-9
emit hisplt: cycle interval = 5
emit restart: time interval = 1.0e-9

Plot variable
  AZ
  JZ
  B
$ avg is needed for multimaterial calculations
  density, avg
  temperature, avg
  pressure, avg
  sound speed, avg
  velocity
  econ
```

```
  ZBAR
  specific_heat_vol, avg
  energy, avg
end

$$$$$$$$$$$$$$$$$$$$$$$  algorithm control
$$$$$$$$$$$$$$$$$$$$$$$$$$$

$$ ML setup
aztec 1     $ mag control
   solver,    cg          $ default = cg
   scaling,   sym_diag    $ default = sym_diag
   conv norm, rhs         $ default = r0
   tol,       1.e-13       $ default = 1.e-5
   output, none
   multilevel
     fine sweeps = 5
     fine smoother = GAUSS SEIDEL
     coarse sweeps = 1
     coarse smoother = lu
     multigrid levels = 10
     interpolation algorithm = AGGREGATION
   end
end


$$$$$$$$$$$$$$$$$$$$$$$$  material models
$$$$$$$$$$$$$$$$$$$$$$$$$$$$$
material 11       WIRE
  model = 11          $ EOS                           (KERLEY ANEOS)
  model = 12          $ electrical conductivity       (EC/TC LMD)
  model = 13          $ elastic plastic
end


$ ----------------- Al models -------------------------------

 model 11 keos sesame          $ al eos data
   feos  = 'sesame'
   neos  = 3700
   clip = 200.0                  $ temperature cutoff T+/- clip at EOS
boundary
 end

 model 12 lmd                  $ al electrical/thermal conductivity
   tuned aluminum
   z = 13.00
   a = 26.98
   rho solid = 2.70e+3         $ kg/m**3
   ec mult = 1.0
   tc mult = 1.0
   temp cutoff = 10.0          $ temperature in Kelvin
 end

 model 13 elastic plastic        $ elastic plastic parameters (manual)
   youngs modulus = 73.00e+13     $ pascals (1 pascal = 10 dyne/cm**2)
   poissons ratio = 0.3225
   yield stress   = 2.76e+08     $ pascals
   hardening modulus = 1.24e+08  $ pascals
   beta              = 1.
 end
```

```
exit
```

Input deck for 600 wires

```
$ Aprepro ($Revision: 1.71 $) Mon Apr 14 11:33:03 2003
$$$$$$$$$$$$$$$$$$$$$$$$$$$  PROBLEM COMMENTS
$$$$$$$$$$$$$$$$$$$$$$$$$$$$
$
$ NAME:           Wire clumping instability (eulerian)
$
$ PHYSICS:  MAGNETOHYDRODYNAMICS
$
$ BOUND. COND:    PERIODIC BOUNDARIES FOR WEDGE FACES
$
$ AUTHORS:  E. Yu, Christopher Garasi (SNL; 9231) & Bryan Oliver (MRC)
$           modified by W.W. Tang
$ DATE:           3/4/2006
$
$ APREPRO definitions:
$ units are assumed to be in microns
$
$ ___________________constants _____________________________
$ { one_ev} = 1.16e4}
$ { unit_conv = 1.0e-6}

$ { tmax = 40.0e-9}
$ { yoffset = 3.0e-5}
$ ____________________USER VARIABLES____________________

title: 2D XY periodic-wire sweep problem

units, si
$start time = 2.368e-6
double precision exodus

$termination time 2.65e-6
termination time {tmax}
$termination cycle 2
$read restart dump, -1

$$$$$$$$$$$$$$$$$$$$$$$$  physics options
$$$$$$$$$$$$$$$$$$$$$$$$$$$$
$
$          MHD parameters
$

magnetohydrodynamics

  detailed energy tallies

$  max vol change 0.05

  dynamics
    material fraction force limit,  0.6, power 1.0
  end

  transient magnetics
$ outer boundary
$ for 60 kA per wire, total current should be 21.6 MA
    xy cylindrical radial slot bc, sideset 300, function 1, scale 1.0,
```

```
    X 0.0, Y 0.0

    void conductivity 1.0e-4
    aztec set, 1
    JOULE HEAT, NOHEAT
    MAGNETIC FORCE, TENSOR
    A REZONE, CT VAN LEER
    ALFVEN VELOCITY MAX, 1.0e6
    include "11MA.dat"
  end

  hydrodynamics
    no displacement, nodeset 100 NORMAL, X -5.235963831e-3 Y
9.999862922e-1
    no displacement, nodeset 200 NORMAL, X -5.235963831e-3 Y -
9.999862922e-1
    no displacement, nodeset 400, X
    no displacement, nodeset 400, Y
  end

  gradual startup factor, 0.3
  time step scale, 0.9

  $$ DIATOM INSERTION COMMANDS
  diatoms
   package 'wire_mat'
    material =  11
    density 2700.0
    temperature 300.
    numsub = 10
    insert circle
     center 0.01 {yoffset}
     radius 10.0e-06
    endinsert
   endpackage

  enddiatoms

$$ BLOCK INPUT
  block 1   $ square containing wire
   eulerian mesh
   add diom input
  end
  block 2   $ between square and innermost block
    eulerian mesh
  end
  block 3   $ innermost block
    eulerian mesh
  end
  block 4   $ outer void
    eulerian mesh
  end


$$ TRACERS
  tracer points
   lag tracer 1, x = 0.01, y = {yoffset}         $ core center
  end

end
```

```
$$$$$$$$$$$$$$$$$$$$$$$  execution control
$$$$$$$$$$$$$$$$$$$$$$$$$$

emit output: time  = 1.0E-9, from 0. to 1.
$emit plot: time interval   = 1.0e-10, from 0. to 2.372e-6
$emit plot: time interval   = 1.0e-9, from 2.372e-6 to 2.7e-6
emit plot: time interval = 1.0e-9
emit screen: cycle  = 50
$emit hisplt: time interval 1.0e-9
emit hisplt: cycle interval = 5
emit restart: time interval = 1.0e-9

Plot variable
  AZ
  JZ
  B
$ avg is needed for multimaterial calculations
  density, avg
  temperature, avg
  pressure, avg
  sound speed, avg
  velocity
  econ
  ZBAR
  specific_heat_vol, avg
  energy, avg
end

$$$$$$$$$$$$$$$$$$$$$$$$  algorithm control
$$$$$$$$$$$$$$$$$$$$$$$$$$

$$ ML setup
aztec 1     $ mag control
   solver,    cg          $ default = cg
   scaling,   sym_diag    $ default = sym_diag
   conv norm, rhs         $ default = r0
   tol,       1.e-13       $ default = 1.e-5
   output, none
   multilevel
     fine sweeps = 5
     fine smoother = GAUSS SEIDEL
     coarse sweeps = 1
     coarse smoother = lu
     multigrid levels = 10
     interpolation algorithm = AGGREGATION
   end
end


$$$$$$$$$$$$$$$$$$$$$$$$  material models
$$$$$$$$$$$$$$$$$$$$$$$$$$$$$
material 11       WIRE
  model = 11          $ EOS                           (KERLEY ANEOS)
  model = 12          $ electrical conductivity       (EC/TC LMD)
  model = 13          $ elastic plastic
end


$ ----------------- Al models ------------------------------
```

```
 model 11 keos sesame          $ al eos data
   feos  = 'sesame'
   neos  = 3700
   clip = 200.0                  $ temperature cutoff T+/- clip at EOS
boundary
 end

 model 12 lmd                  $ al electrical/thermal conductivity
   tuned aluminum
   z = 13.00
   a = 26.98
   rho solid = 2.70e+3         $ kg/m**3
   ec mult = 1.0
   tc mult = 1.0
   temp cutoff = 10.0          $ temperature in Kelvin
 end

 model 13 elastic plastic        $ elastic plastic parameters (manual)
   youngs modulus = 73.00e+13     $ pascals (1 pascal = 10 dyne/cm**2)
   poissons ratio = 0.3225
   yield stress   = 2.76e+08     $ pascals
   hardening modulus = 1.24e+08  $ pascals
   beta              = 1.
 end


exit
```

Appendix E

Preliminary study of the effect of coronal plasma

In this preliminary study, the effect of coronal plasma was investigated by using ALEGRA [Gra04]. For the simulations of the π mode clumping instability, an Eulerian mesh is used. A wedge shape domain is used with reflective boundary condition in the azimuth [Fig. 2.2a]. The reflective boundary condition automatically filters out all other modes except the π mode. Changing the angle of the wedge is equivalent to changing the number of wire in the array. A 2D-xy simulation, with coronal plasmas, including joule heating, radiation transport and thermal conduction is set up [Fig. E1]. Aluminum plasma circular in shape with a diameter of 50 μm centered about the original wire with a diameter of 20 μm in a 1 cm radius cylindrical array are simulated with an initial perturbation of 30 μm off the bisector of the wedge. The aluminum plasma has a temperature of approximately 1.16×10^5 K (approximately 10 eV). The ALEGRA simulation geometry with coronal plasma is shown in Fig. E1.

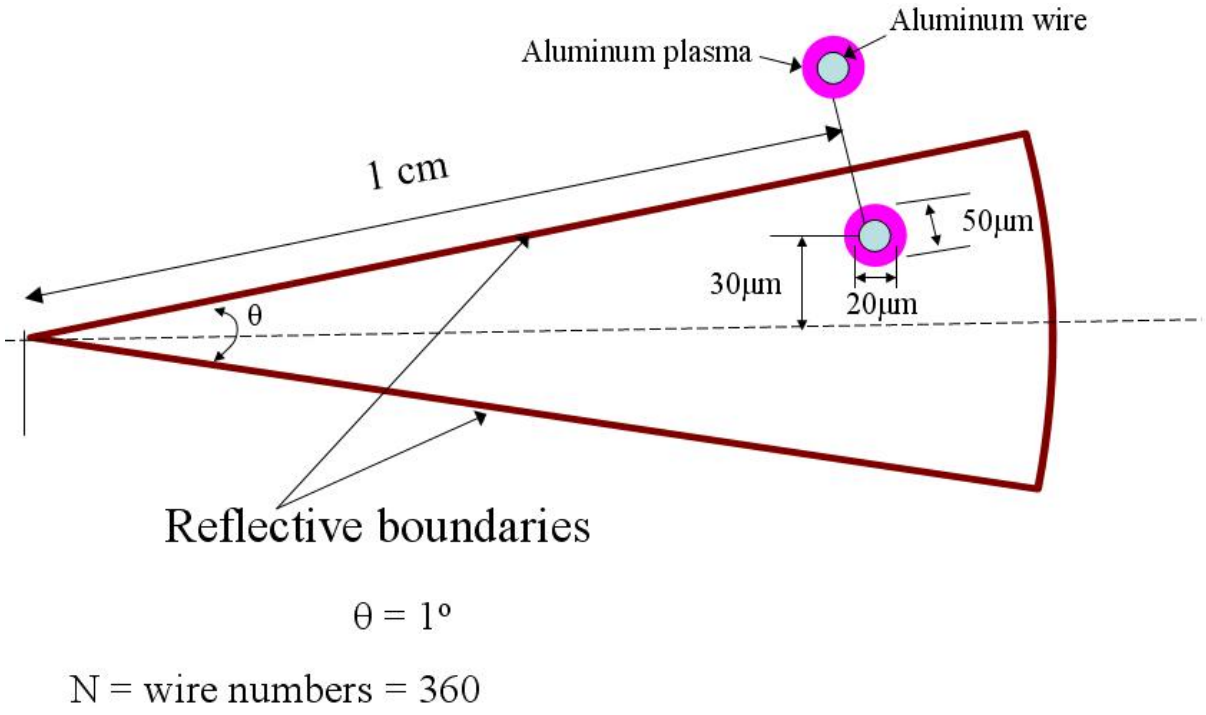

Fig. E1 ALEGRA simulation geometry with aluminum plasma.

In order to study the effect of the coronal plasma, we reduce the conductivity of the wire core by a factor of 100 for 15 ns to force the current to run in the coronal plasma. This is a practice that was employed in [Sin04, Yu07]. After 15 ns, the wire core conductivity is returned to its normal value to investigate how much current is returned back to the wire core. The preliminary results are presented in Fig. E2, which shows the fraction of the total current in the wire (top figure). Figure E2 (middle) shows the total current profile, and Fig. E2 (bottom) shows the current in the wire, in units of amp.

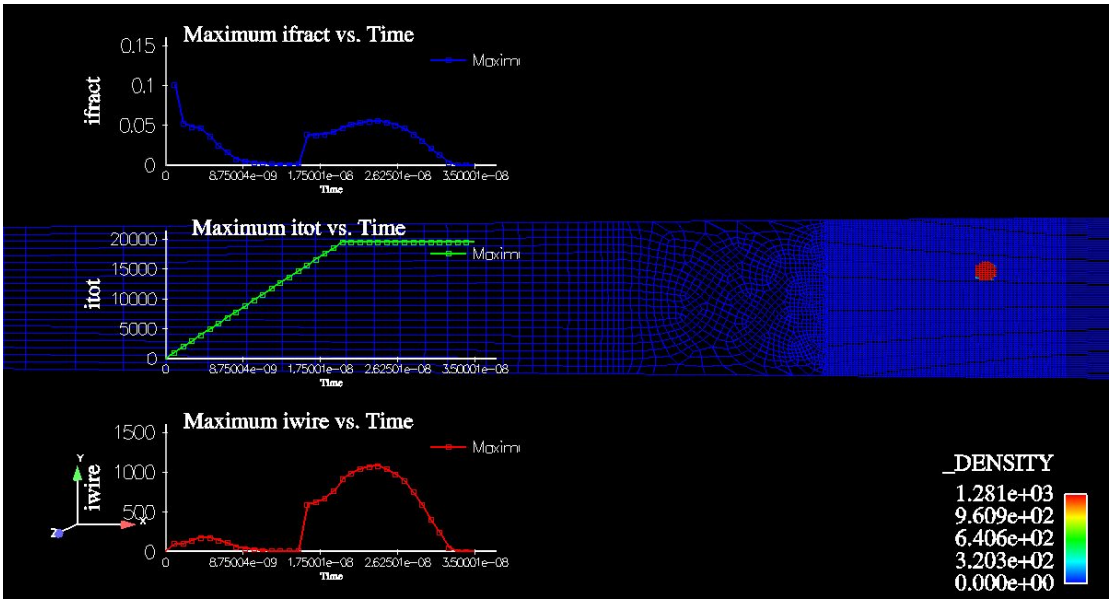

Fig. E2 ALEGRA simulation result with aluminum coronal plasma. The core conductivity is reduced by a factor of 100 for 15 ns.

These simulation results show that at most 5 – 10% of the current is switched back to the wire core after 15 ns, which implies the π mode clumping instability growth rate will be reduced by a factor of 10 (in the best case), since the π mode growth rate is linearily proportional to the amount of current presence in the wire [c.f. Eq. (2.1) and (2.5)]. These preliminary results show mitigation of clumping instability by the presence of a plasma corona that shunts the currents in the wires [Cun05a, Leb04, Sin05].

ALEGRA simulation input deck with aluminum coronal plasma for 360 wires.

```
$ Aprepro ($Revision: 1.71 $) Mon Apr 14 11:33:03 2003
$$$$$$$$$$$$$$$$$$$$$$$$$$$$  PROBLEM COMMENTS
$$$$$$$$$$$$$$$$$$$$$$$$$$$$$$
$
$ NAME:           Wire clumping instability (eulerian)
$
$ PHYSICS:  MAGNETOHYDRODYNAMICS
$
$ BOUND. COND:    PERIODIC BOUNDARIES FOR WEDGE FACES
$
$ AUTHORS:  E. Yu, Christopher Garasi (SNL; 9231) & Bryan Oliver (MRC)
$           modified by W.W. Tang
$ DATE:           3/4/2006
$
$ APREPRO definitions:
```

```
$ units are assumed to be in microns
$
$ ___________________constants _____________________________
$ { one_ev} = 1.16e4}
$ { unit_conv = 1.0e-6}

$ { tmax = 70.0e-9}
$ { yoffset = 3.0e-5}
$ ____________________USER VARIABLES_____________________

title: 2D XY periodic-wire sweep problem

$ to start off, set tmax=5ns and 'econ mult=0.01' and comment out
$ 'read restart dump, -1'
$ let the simulation run to completion, then change tmax to desired
value,
$ change 'econ mult=1.0', and put back in 'read restart dump, -1'

units, si
$start time = 2.368e-6
double precision exodus

termination time {tmax}
$termination cycle 2
read restart dump, -1

$$$$$$$$$$$$$$$$$$$$$$$$  physics options
$$$$$$$$$$$$$$$$$$$$$$$$$$$$
$
$          MHD parameters
$

radiation magnetohydrodynamics conduction

  detailed energy tallies

  max vol change 0.1

  dynamics
    material fraction force limit,  0.8, power 3.0
  end

  transient magnetics
$ outer boundary
$ for 60 kA per wire, total current should be 21.6 MA
    xy cylindrical radial slot bc, sideset 300, function 1, scale 1.0,
    X 0.0, Y 0.0

    void conductivity 1.0e-4
    aztec set, 1
$    JOULE HEAT, NOHEAT
    MAGNETIC FORCE, TENSOR
    A REZONE, CT VAN LEER
    ALFVEN VELOCITY MAX, 1.0e6
    ALFVEN DENSITY FLOOR, 0.001
    include "7MA.dat"
  end

  hydrodynamics
    no displacement, nodeset 100 NORMAL, X -8.726535e-3 Y  9.999619e-1
    no displacement, nodeset 200 NORMAL, X -8.726535e-3 Y -9.999619e-1
```

```
  no displacement, nodeset 400, X
  no displacement, nodeset 400, Y

end

thermal conduction
  aztec set, 2
  scale, 1.0e20
  minimum temperature, 1.e20
end

cell doctor
 discard 1
 time range, min 0.0 max {tmax}
 minimum position, x=-1.0 y=-1.0
 maximum position, x=1.0 y=1.0
 trigger, temperature, minimum 1.0e6 maximum 1.0e10
 frequency 1
 end
end
gradual startup factor, 1.0
time step scale, 1.0

radiation

  linearized diffusion

   group bounds   $ keV
     log 0.001 [eV] to 10. [keV] by 1
   end

   vacuum boundary, sideset 300   $outer boundary
   reflective boundary, sideset 100
   reflective boundary, sideset 200
   reflective boundary, sideset 400

   flux limiter = simplified levermore pomraning

   steady state initialization
   aztec set, 3

   maximum energy density change = 0.15
  end
end

$$ DIATOM INSERTION COMMANDS
diatoms
 package 'wire_mat'
  material =  1
  density 19300.0
  temperature 300.
  numsub = 10
  insert circle
   center 0.01 {yoffset}
   radius 10.0e-06
  endinsert

 endpackage

 package 'corona_mat'
  material =  1
```

```
    numsub = 10
    density 1.9
    temperature 1.16e5.
    insert circle
     center 0.01 {yoffset}
     radius 25.0e-06
    endinsert
   endpackage

  enddiatoms

$$ BLOCK INPUT
  block 1   $ square containing wire
   eulerian mesh
   add diom input
  end
  block 2   $ between square and innermost block
    eulerian mesh
  end
  block 3   $ innermost block
    eulerian mesh
  end
  block 4   $ outer void
    eulerian mesh
  end


$$ TRACERS
  tracer points
   lag tracer 1, x = 0.01, y = {yoffset}         $ core center
  end

end


$$$$$$$$$$$$$$$$$$$$$$$$$  execution control
$$$$$$$$$$$$$$$$$$$$$$$$$$

emit output: time  = 1.0E-9, from 0. to 1.
$emit plot: time interval   = 1.0e-10, from 0. to 2.372e-6
$emit plot: time interval   = 1.0e-9, from 2.372e-6 to 2.7e-6
emit plot: time interval = 1.0e-9
emit screen: cycle  = 50
$emit hisplt: time interval 1.0e-9
emit hisplt: cycle interval = 5
emit restart: time interval = 1.0e-9

Plot variable
  AZ
  JZ
  B
$ avg is needed for multimaterial calculations
  density, avg
  temperature, avg
  pressure, avg
  sound speed, avg
  velocity
  econ
  opacity_a
  opacity_r
  thermal_con
```

```
  rad temperature, as "RAD_T"
  rad energy density, as "RAD_E"
  ZBAR
  specific_heat_vol, avg
  energy, avg
end

$$$$$$$$$$$$$$$$$$$$$$$$  algorithm control
$$$$$$$$$$$$$$$$$$$$$$$$$$$$

$$ ML setup
aztec 1     $ mag control
   solver,    cg          $ default = cg
   scaling,   sym_diag    $ default = sym_diag
   conv norm, rhs         $ default = r0
   tol,       1.e-13       $ default = 1.e-5
   output, none
   multilevel
     fine sweeps = 5
     fine smoother = GAUSS SEIDEL
     coarse sweeps = 1
     coarse smoother = lu
     multigrid levels = 10
     interpolation algorithm = AGGREGATION
   end
end

aztec 2     $ thermal con  control
  solver,   cg
  scaling,  sym_diag
  conv norm, rhs
  precond,  none
  output,  none
  tol,      1.e-14
  max iter = 10000
end

aztec 3     $ radiation diffusion control
   solver,        cg
   scaling,   sym_row_sum
   conv norm, r0
   tol,           1.e-14
   max iter, 10000
   output, none
   multilevel
      fine sweeps = 5
      fine smoother = GAUSS SEIDEL
      coarse sweeps = 1
      coarse smoother = lu
      multigrid levels = 15
      interpolation algorithm = AGGREGATION
   end
end


$$$$$$$$$$$$$$$$$$$$$$$$  material models
$$$$$$$$$$$$$$$$$$$$$$$$$$$$$$$$
material 1       WIRE
  model = 100          $ EOS                            (KERLEY ANEOS)
  model = 105          $ electrical conductivity        (EC/TC LMD)
  model = 14           $ opacity
```

```
  number of elements 1
     element 74, mass 183.85, fraction 1.0
  end
end

$ ----------------- Al models -------------------------------

 model 100 lanl sesame          $ W eos data
   nmat = 3544
   table = 301
   clip = 300.0                 $ temperature cutoff T+/- clip at EOS
boundary
   $primary interp, 'linear'
   feos = 'W3544.ses'
 end

 model 105 lmd                  $ W electrical/thermal conductivity
   $tuned aluminum
   z = 74.00
   a = 183.85
   rho solid = 19300.0         $ kg/m**3
   temp cutoff = 10.0
$  this defines the (rho, T) box in which you want to change the
conductivity
   t0 = 0.0
   tf = 1.5e4
   r0 = 0.0
   rf = 30.0e3
$  this has to be set to 0.01 or 0.1 to begin with, to reduce
conductivity
$  in the core
   econ mult = 1.0
 end

  model 14 tabular opacity         $ W opacity
   dynamic integration            $ not valid for multi-group rad
   $minimum temperature = 300.0
  end

exit
```

Appendix F

Impact time calculation assuming all current flows in wire cores from t=0ns

Mathematica Input of Impact time for 236 μm center-to-center spacing

```
Itot = 1*10^6;
Iw = Itot/8;
muo = 4xπ*10^-7;
radius = 3.75*10^-6;
ml = 19300 * π*(radius)^2;
Ro = 8*10^-3;
d = 2*π*Ro/8;
Δ = 2.36*10^-4;
ξo = Ro * (22.5/180) *π - Δ/2;
gammap = Sqrt[π*muo*(Iw)^2/(4*ml*d^2)];
zin = π/d * ξo;
zfinal = π/d * Ro * 22.5/180 *π;
RHS = NIntegrate[1/Sqrt[-2*Log[Cos[z]/Cos[zin]]], {z, zin, zfinal}]
LHS = NIntegrate[Sqrt[π*muo*(Iw*(Sin[π*t/(200*10^-9)])^2)^2/(4*ml*d^2)], {t, 0, 35.5*10^-9}]
```

Mathematica Input of Impact time for 447 µm center-to-center spacing

```
Itot = 1*10^6;
Iw = Itot/8;
muo = 4xπ*10^-7;
radius = 3.75*10^-6;
ml = 19300 * π*(radius)^2;
Ro = 8*10^-3;
d = 2*π*Ro/8;
Δ = 2.36*10^-4;
ξo = Ro * (22.5/180) *π - Δ/2;
gammap = Sqrt[π*muo*(Iw)^2/(4*ml*d^2)];
zin = π/d * ξo;
zfinal = π/d * Ro * 22.5/180 *π;
RHS = NIntegrate[1/Sqrt[-2*Log[Cos[z]/Cos[zin]]], {z, zin, zfinal}]
LHS = NIntegrate[Sqrt[π*muo*(Iw*(Sin[π*t/(200*10^-9)])^2)^2/(4*ml*d^2)], {t, 0, 35.5*10^-9}]
```

Appendix G

Impact time calculation assuming current is "switched on" in the wires at t=60ns

Mathematica Input of Impact time for 236 μm center-to-center spacing

```
Itot = 0.7*10^6;
Iw = Itot/8;
muo = 4×π*10^-7;
radius = 3.75*10^-6;
ml = 19300 * π*(radius)^2;
Ro = 8*10^-3;
d = 2*π*Ro/8;
Δ = 2.36*10^-4;
ξo = Ro * (22.5/180) *π - Δ/2;
gammap = Sqrt[π*muo*(Iw)^2/(4*ml*d^2)];
zin = π/d * ξo;
zfinal = π/d * Ro * 22.5/180 *π;
tin = 0;
uin = 0;
tf = 1/gammap * NIntegrate[1/Sqrt[-2*Log[Cos[z]/Cos[zin]]], {z, zin, zfinal}] + 60*10^-9
```

$$6.49375\times10^{-8}$$

Mathematica Input of Impact time for 447 µm center-to-center spacing

```
Itot = 0.7*10^6;
Iw = Itot/8;
muo = 4*π*10^-7;
radius = 3.75*10^-6;
ml = 19300 * π*(radius)^2;
Ro = 8*10^-3;
d = 2*π*Ro/8;
Δ = 4.447*10^-4;
```

$$\xi o = Ro * \left(\frac{22.5}{180}\right) * \pi - \frac{\Delta}{2};$$

$$gammap = \sqrt{\frac{\pi * muo * (Iw)^2}{4 * ml * d^2}};$$

$$zin = \frac{\pi}{d} * \xi o;$$

$$zfinal = \frac{\pi}{d} * Ro * \frac{22.5}{180} * \pi;$$

$$tf = \frac{1}{gammap} * NIntegrate\left[\frac{1}{\sqrt{-2 * Log\left[\frac{Cos[z]}{Cos[zin]}\right]}}, \{z, zin, zfinal\}\right] + 60*10^{-9}$$

$$6.93139 \times 10^{-8}$$

Appendix H

Details of the mapping function and derivation of Eqs. (3.3a,b) and (3.5)

As stated in the main text, we consider a 2-dimensional rectangular current channel Fig.3.7a,b with top boundary *ABCDEF* and mid-plane *GH (y=0).* The main channel has half width *b*, and the bridge, or constriction, has half width $a < b$, and total length *2h*. The width is L_3 in the third, ignorable dimension. The two boundaries, *ABCDEF* and *GH*, are streamlines. We solve the current flow of this Cartesian geometry by conformal mapping between the complex z- and w-plane where $z = x + iy = (x, y)$, $w = u + iv = [u, v]$. In the notation of Lau [Mil07], this is denoted as $(x, y) \leftrightarrow [u, v]$. The maps of $AB \ldots GH$ in Figs. 3.7a and 3.7b are, sequentially, $(\infty$,b) $\leftrightarrow$ [0^+, 0], (h, b) $\leftrightarrow$ [1, 0], (h, a) $\leftrightarrow$[u_3, 0], (-h, a) $\leftrightarrow$ [u_4, 0], (-h, b) $\leftrightarrow$ [u_5, 0], $(-\infty$,b) $\leftrightarrow$ [∞, 0], $(-\infty,0) \leftrightarrow [-\infty, 0]$, and $(\infty,0) \leftrightarrow$ [0^-, 0]. In the maps *A'* and *H'*, 0^+ and 0^- denote values slightly greater and less than zero, respectively. This map is governed by the Schwarz-Christoffel transformation [Hil62],

$$z = z(w) = K\int_1^w dw f(w) + (h + ib); \qquad f(w) = \frac{1}{w}\sqrt{\frac{(w-u_3)(w-u_4)}{(w-1)(w-u_5)}}; \qquad u_5 = u_3 u_4, \quad \textbf{(H1a,b)}$$

where $K = -b/\pi$. The constants u_3, u_4 and u_5 are real and positive with $1 < u_3 < u_4 < u_5$ [Fig. 3.7b]. We showed that $u_5 = u_3u_4$. Branch cuts shown in Fig. H1 extending downwards from the four branch points, $w = 1, u_3, u_4$ and u_5, render $f(w)$ single-valued

in the upper half w-plane. Evaluating *z(w)* at the corners *C* and *D*, and subtracting, we obtain Eq. (3.3a).

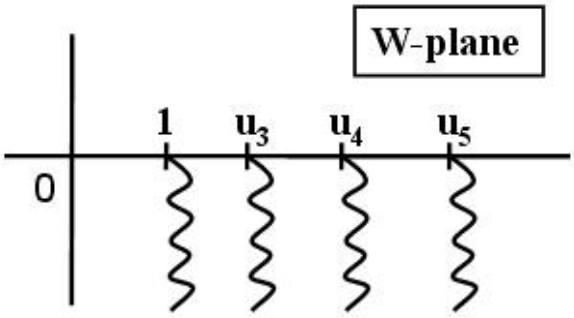

Fig. H1 **Appropriate branch cuts extending downwards from the four branch points, w = 1, u_3, u_4 and u_5, which render $f(w)$ single-valued in the upper half w-plane [Fig. 3.7a,b].**

Evaluating *z(w)* at corner *C*, we obtain Eq. (3.3b). Once u_3 and u_4 are specified (and therefore $u_5 = u_3u_4$ is also known), all aspect ratios *h/b*, *a/b* and therefore *h/a = (h/b)/(a/b)* may readily be computed.

To derive Eq. (3.5), let's consider the total current flowing through the channel. The total current flowing through the channel is $I = \sigma E_0 (2b \times L_3)$, where σ is the electrical conductivity of the channel. For the time being, let us consider points *G* and *H* to be finite in the *z*-plane [Fig. 3.7a], with the respective maps for *G*: $z_G = (x_G, 0) \leftrightarrow [u_G, 0]$, and for *H*: $z_H = (x_H, 0) \leftrightarrow [u_H, 0]$. The voltage drop from *H* to *G* is $V = -KE_0 \log(u_G/u_H)$ from the real part of the complex potential, $\Phi = KE_0 \log w$, as stated in the main text. The total electrical resistance between *G* and *H* is then $R = V/I = [\rho/(2\pi L_3)]\log(u_G/u_H)$, where $\rho = 1/\sigma$ is the electrical resistivity of the channel. We may next express this total resistance as $R = R_u + R_c$, where R_u is the resistance between *G* and *H* in a uniform channel (i.e., as if *a* = *b*) and R_c is the remainder that is solely due to the constriction of the channel. From this definition,

$R_u = \rho(z_H - z_G)/(2b \times L_3)$, where z_H and z_G are given in terms of the integral in Eq. (H1), evaluated respectively at $w = [u_H, 0]$ and at $w = [u_G, 0]$. Upon taking the limit $u_G \to -\infty$ and $u_H \to 0^-$, we obtain the real integral for contact resistance $R_c = R - R_u$, which is Eq. (3.5).

Appendix I

Derivation of the asymptotic formula for zero-bridge-length (ZBL) limit, Eq. (3.7)

This Appendix outlines the derivation of the asymptotic ZBL contact resistance formula, Eq. (3.7). Start with Eqs. (3.2) and (3.3b) and, set $u_3 = u_4$ (since we are considering the ZBL limit), Eq. (3.2) becomes,

$$f(w) = \frac{1}{w} \frac{(w - u_3)}{\sqrt{(w-1)(w - u_3{}^2)}} \tag{I1}$$

Substitute Eq. (I1) into Eq. (3.3b) gives,

$$\frac{b}{a} = \left(1 - \frac{1}{\pi} \int_1^{u_3} dw \left| \frac{(w - u_3)}{w\sqrt{(w-1)(w - u_3{}^2)}} \right| \right)^{-1} \tag{I2}$$

Evaluating Eq. (I2) by assuming $u_3 >> 1$ yields (a detail proof of Eq. (I3) is given in Appendix J),

$$\frac{b}{a} \cong \frac{\pi\sqrt{u_3}}{4} \tag{I3}$$

Again, setting $u_3 = u_4$ (>1) for the ZBL limit, Eq. (3.5) becomes,

$$\overline{R_{c0}} = \int_0^{\infty} \frac{dw}{w} \left[1 - \frac{(w + u_3)}{\sqrt{(w+1)(w + u_3{}^2)}} \right] \equiv \int_0^{\infty} p(w) dw \tag{I4a}$$

$$p(w) = \frac{1}{w} \left[1 - \frac{(w + u_3)}{\sqrt{(w+1)(w + u_3{}^2)}} \right] \tag{I4b}$$

A careful examination of Eq. (I4b) shows that the only singularities of p(w) are the two branch points at $w=-1$ and $w=-u_3{}^2$. Contour integral is used to evaluate Eq. (I4a). By carefully choosing the branch cut as shown in Fig. I1, Eq. (I4a) can be written as,

$$\int_0^{\infty} p(w)dw = \underbrace{\int_0^{-1} p(w)dw}_{C_1} + \underbrace{\int_{-1}^{-u_3{}^2} p(w)dw}_{C_2} + \underbrace{\int_{-u_3{}^2}^{\infty} p(w)dw}_{C_3} \qquad \textbf{(I5)}$$

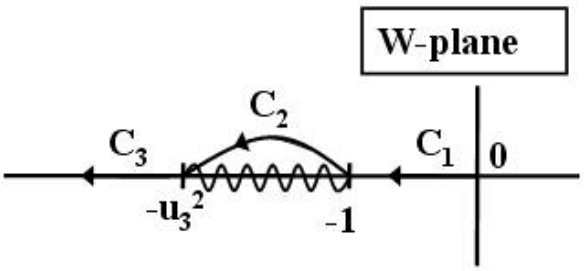

Fig. I1 Appropriate branch cuts for evaluating Eq. (I4).

Let us work on C_1, the first term on the R.H.S. of Eq. (I5),

$$\int_0^{-1} \frac{dw}{w}\left[1-\frac{w+u_3}{\sqrt{(w+1)(w+u_3{}^2)}}\right] = \int_0^{-1} \frac{dw}{w}\left[1-\frac{1}{\sqrt{w+1}}\left(1+\frac{w}{u_3}-\frac{w}{2u_3{}^2}+\cdots\right)\right] \qquad \textbf{(I6)}$$

The parenthesis is clearly on the order of $1/u_3$. Under the assumption $u_3 >> 1$, Eq. (I6) can be written as,

$$\int_0^{-1} p(w)dw = \int_0^{-1} \frac{dw}{w}\left[1-\frac{1}{\sqrt{w+1}}\right] + O\left(\frac{1}{u_3}\right) = -2\log 2 + O\left(\frac{1}{u_3}\right) \qquad \textbf{(I7)}$$

Next, let us work on C_2, the second term on the R.H.S. of Eq. (I5),

$$\int_{-1}^{-u_3{}^2} p(w)dw = \int_{-1}^{-u_3{}^2} \frac{dw}{w} - \int_{-1}^{-u_3{}^2} \frac{dw}{w}\frac{(w+u_3)}{\sqrt{(w+1)(w+u_3{}^2)}} \qquad \textbf{(I8)}$$

The second integral on the R.H.S. of Eq. (I8) evaluates to zero. To see this, we recognize first that for the contour C_A and C_R in Fig. I2, the integral $\oint_{C_A} p(w)dw = \oint_{C_R} p(w)dw = 0$,

since *p(w)* is analytic between C_A and C_R, by noting that $p(w) \propto w^2$ as $w \to 0$, and $p(w) \propto 1/w^2$ as $w \to \infty$.

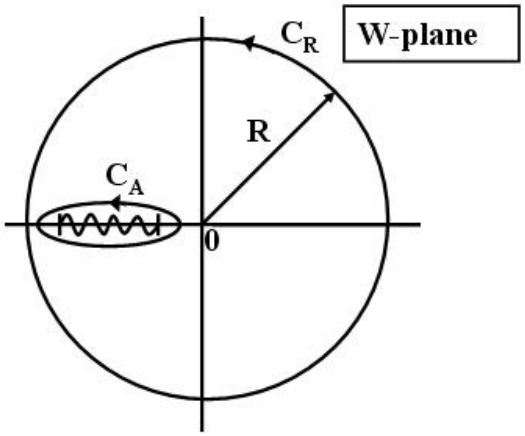

Fig. I2 **Chosen contours for evaluation of the second integral on the R.H.S. of Eq. (I8).**

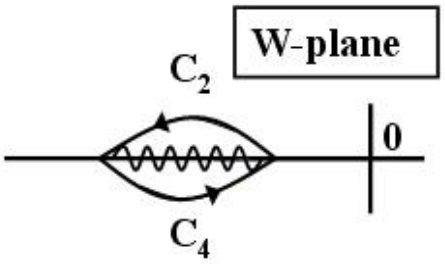

Fig. I3 **The contour c_A , separated into contour c_2 and c_4.**

The contour c_A can be separated into contour c_2 and c_4 [Fig. I3].

$$\oint_{c_A} p(w)dw = \oint_{c_A} \frac{dw}{w} - \left[\int_{c_2} dw \frac{w+u_3}{\sqrt{(w+1)(w+u_3{}^2)}} + \int_{c_4} dw \frac{w+u_3}{\sqrt{(w+1)(w+u_3{}^2)}} \right] \qquad \textbf{(I9)}$$

It can easily be seen that Term 1 on the R.H.S. of Eq. (I9) evaluate to zero, which implies,

$$\int_{c_2} dw \frac{w+u_3}{\sqrt{(w+1)(w+u_3{}^2)}} = -\int_{c_4} dw \frac{w+u_3}{\sqrt{(w+1)(w+u_3{}^2)}} \qquad \textbf{(I10)}$$

Because w lies on opposite sides of the branch cut [Fig. I3] on the two integrals of (I10), the arguments of these integrals are of opposite sign. Also, the direction of integration along C_2 and C_4 are opposite. Thus, Eq. (I10) can be true if and only if,

$$\int_{c_4} dw \frac{w+u_3}{\sqrt{(w+1)(w+u_3{}^2)}} = \int_{c_2} dw \frac{w+u_3}{\sqrt{(w+1)(w+u_3{}^2)}} = 0 \qquad \textbf{(I11)}$$

Therefore, the second term on the R.H.S. of Eq. (I8) evaluates to zero and,

$$\int_{-1}^{-u_3{}^2} p(w)dw = 2\log[u_3] \qquad \textbf{(I12)}$$

Lastly, let us work on C_3 [Fig. I1], the third term on the R.H.S. of Eq. (I5),

$$\int_{-u_3{}^2}^{-\infty} p(w)dw = \int_{-u_3{}^2}^{-\infty} \frac{dw}{w}\left[1 - \frac{\sqrt{w}}{\sqrt{w+u_3{}^2}}\right] - \int_{-u_3{}^2}^{-\infty} \frac{dw}{w}\left[\frac{\sqrt{w(u_3/w + 1/2w + \cdots)}}{\sqrt{w+u_3{}^2}}\right] \qquad \textbf{(I13)}$$

after expanding $\sqrt{w+u_3} = \sqrt{w}[1 + u_3/(2w) + \cdots]$ for $w > u_3$, and $\sqrt{w+1} = \sqrt{w}[1 - 1/(2w) + \cdots]$. Examining Eq. (I13) carefully, we can see that the last integral on the R.H.S. of Eq. (I13) is also on the order of $1/u_3$. Evaluating Eq. (I13) yields,

$$\int_{-u_3{}^2}^{-\infty} p(w)dw = -2\log 2 + O\left(\frac{1}{u_3}\right) \qquad \textbf{(I14)}$$

Combine Eqs. (I7), (I12) and (I14) yields the final result for Eq. (I4),

$$\overline{R_{c0}} = \int_0^{\infty} p(w)dw \cong \log\left(\frac{u_3{}^2}{16}\right) + O\left(\frac{1}{u_3}\right) \qquad \textbf{(I15)}$$

Substitute Eq. (I3) into Eq. (I15) yields the asymptotic formula of Eq. (3.7).

Appendix J

Proof of Equation (I3)

To prove Eq. (I3), we set $u_4 = u_3$ in the zero-bridge-length limit to write Eq. (3.2) as

$$\left|f(w)\right| = \frac{u_3 - w}{w}\sqrt{\frac{1}{(w-1)(u_3^2 - w)}}, \qquad 1 < w < u_3 \ . \tag{J1}$$

Equation (J1) is next used in the integral that appears in Eq. (3.3b), designated as $g(u_3)$,

$$g(u_3) = \int_1^{u_3} dw \left|f(w)\right| . \tag{J2}$$

For $u_3 >> 1$, we expand the factor $1/(u_3^2 - w)^{1/2} = 1/u_3 + O(w/u_3^3)$ in Eq. (J1) and write Eq. (J2) as

$$g(u_3) = \int_1^{u_3} dw \frac{u_3 - w}{u_3 w}\sqrt{\frac{1}{(w-1)}}\left[1 + O(\frac{w}{u_3^2})\right] = h(u_3) + O(\frac{1}{u_3^{3/2}}) , \tag{J3}$$

$$h(u_3) = \int_1^{u_3} dw \frac{u_3 - w}{u_3 w}\sqrt{\frac{1}{(w-1)}} \equiv h_1(u_3) + h_2(u_3) , \tag{J4}$$

$$h_1(u_3) = \int_1^{u_3} dw \frac{1}{w}\sqrt{\frac{1}{(w-1)}} = 2\tan^{-1}(\sqrt{u_3 - 1}) = \pi - \frac{2}{\sqrt{u_3}}\left[1 + O(1/u_3)\right], \tag{J5}$$

$$h_2(u_3) = -\int_1^{u_3} dw \frac{1}{u_3}\sqrt{\frac{1}{(w-1)}} = -\frac{2}{u_3}\sqrt{u_3 - 1} = -\frac{2}{\sqrt{u_3}}\left[1 + O(1/u_3)\right]. \tag{J6}$$

To obtain Eq. (J5), we have made a change of variable, w - 1 = y^2, in the integral, and used the asymptotic expansion of $\tan^{-1}(x)$ for large values of x. Upon using Eqs. (J5) and (J6) into Eq. (J4), we write Eq. (J3) as

$$g(u_3) = \pi - \frac{4}{\sqrt{u_3}}\left[1 + O(1/u_3)\right], \qquad u_3 >> 1. \tag{J7}$$

Equation (3.3b) is simply, $a/b = 1 - g(u_3)/\pi$, which yields upon using Eq. (J7),

$$u_3 = \left(\frac{4b}{\pi a}\right)^2 \left[1 + O(a^2/b^2)\right], \qquad b/a >> 1, \tag{J8}$$

which is Eq. (I3) of Appendix I. Equation (J8) implies that $u_3 >> 1$ if $b/a >> 1$, therefore justifying a'posteriori all asymptotic expansions for large u_3 in the regime $b/a >> 1$.

BIBLIOGRAPHY

BIBLIOGRAPHY

[And58] O.A. Anderson, W.R. Baker, S.A. Colgate, H.P. Furth, J.Ise, Jr., R.V. Pyle, and R.E. Wright, "Neutron production in linear deuterium pinches," Phys. Rev. **109**, 612 (1958).

[Ans70] MAXWELL®, ©1970-2009, Ansys, Inc.

[Bai00] J. E. Bailey, J. Asay, M. Bernard, A. L. Carlson, G. A. Chandler, C. A. Hall, D. Hanson, R. Johnson, P. Lake, and J. Lawrence, "Optical spectroscopy measurements of shock waves driven by intense z-pinch radiation," J. Quant. Spectrosc. Radiat. Transf. **65**, 31 (2000).

[Bai04] J. E. Bailey, G. A. Chandler, S. A. Slutz, I. Golovkin, P.W. Lake, J. J. MacFarlane, R. C. Manchini, T. J, Burris-Mog, G. Cooper, R. J. Leeper, T. A> Mehlhorn, T. C. Moore, T.J. Nash, D. S. Nielesn, C. L. Ruiz, D. G. Schoroen, and W. A. Varnum, "Hot dense capsule-implosion cores produced by z-pinch dynamic hohlraum radiation," Phys. Rev. Lett. **92**, 085002 (2004).

[Ben34] W.H. Bennett, "Magnetically self-focusing streams," Phys. Rev. **45**, 890 (1934).

[Bla03] S. N. Bland, S. V. Lebedev, J. P. Chittenden, C. Jennings, and M. G. Haines, "Nested wire array Z-pinch experiments operating in the current transfer mode," Phys. Plasmas **10**, 1100 (2003).

[Boo07] J. H. Booske, "Plasma physics challenges of mm-to-THz and high power microwave generation," Plenary Review Paper, American Physical Soceity, Plasma Physics Division Annual Meeting (Orlando, FL; November 14, 2007).

[Bra96] A. V. Branitskii, S. A. Dan'ko, A. V. Gerusov, E. V. Grabovskii, V. I. Zaitsev, S. V. Zakharov, M V. Zurin, D. V. Kuznetsov, S. F. Medovshikov, V. O. Mishenskii, S. L. Nedoseev, G. M. Oleinik, V. E. Pichugin, T. L. Razinkova, P. V. Sasorov, V. P. Smirnov, A. N. Starostin, S. V. Trofimov, I. N. Frolov, and M. V. Fedulov, "Penetration of azimuthal magnetic flux to the interior of an unstable liner," Plasma Phys. Rep. **22**, 277 (1996).

[Bur90] V.A. Burtsev, N.V. Kalinin, and A.V. Luchinsky, Electrical Explosion of Conductors (Energoatomizdat, Moscow, 1990).

[But58] E. D. Butt, R. Carruthers, J. J. D. Mitchell, et. al., Proceedings of the Second United National Conference on Peaceful Uses of Atomic Energy Vol. **32,** p. 42 (1958).

[Car95] J. L. Carbonero, G. Morin, and B. Cabon, "Comparison between beryllium-copper and tungsten high frequency air coplanar probes," IEEE Trans. Microwave Theory and Tech. **43**, 2786 (1995).

[Cha02] K. M. Chandler, D. A. Hammer, D. B. Sinars, S. A. Pikus, and T. A. Shelkovenko, "The relationship between exploding wire expansion rates and wire material properties near the boiling temperature," IEEE Trans. Plasma Sci. **30**, 577 (2002).

[Chi99] J. P. Chittenden, S. V. Lebedev, S. N. Bland, J. Ruiz- Camacho, F. N. Beg, and M. G. Haines, "Two and three dimensional modeling of the different phases of wire-array z-pinch evolution," Laser and Particle Beams, **19**, 323 (2001); Phys. Plasmas **8**, 2305 (2001); Phys. Rev. **E61**, 4370 (2000).

[Chi01] J. P. Chittenden, S. V. Lebedev, S. N. Bland, J. Ruiz- Camacho, F. N. Beg, and M. G. Haines, Laser and Particle Beams, **19**, 323 (2001); J. P. Chittenden, S. V. Lebedev, S. N. Bland, F. N. Beg, and M. G. Haines, "One, two, and three-dimensional modeling of the different phases of wire array Z-pinch evolution, Phys. Plasmas **8**, 2305 (2001); J. P. Chittenden, S. V. Lebedev, j. Ruiz-Camacho, F. N. Beg, S. N. Bland, C. A. Jennings, A. R. Bell, and M. G. Haines, "Plasma formation in metallic wire Z-pinch," Phys. Rev. **E61**, 4370 (2000).

[Cho64] M. Chodorow and C. Susskind, *Fundamentals of Microwave Electronics*, p. 99 (McGraw-Hill, New York, 1964).

[Cov01] C. A. Coverdale, C. Deeney, M.R. Douglas, J. P. Arpuzese, K. G. Whitney, J. W. Thornhill, J. Davis, "Optimal wire-number range for high x-ray power in long implosion time aluminum Z pinches," Phys. Rev. Lett., **88**, 065001-1 (2002); C. Denney, C. A. Coverdale, and M. R. Douglas, "A review of long implosion time z pinches as efficient and high power radiation sources," Laser and Particle Beams, **19**, 497 (2001).

[Cun01] M. E. Cuneo, R. A. Vesey, J. L. Porter, G. Chandler, D. Fehl, T. Gilliland, D. L. Hanson, J. S. McGurn, P. G. Reynolds, L. E. Ruggles, H. Seamen, R. B. Spielman, K. W. Struve, W. A. Stygar, W. W. Simpson, J. A> Torres, and D. F. Wenger, "Development and characterization of a Z-pinch-driven hohlraum high-yield inertial confinement fusion target concept," Phys. Plasmas **8**, 2257 (2001).

[Cun02] M. E. Cuneo, R. A. Vesey, J. L. Porter, G. R. Bennett, D. L. Hanson, L. E. Ruggles, W. W. Simpson, G. C. Idzorek, W. A. Stygar, J. H. Hammer, J. J. Seamen, J. A. Torres, J. S. McGurn, and R. M. Green, "Double Z-pinch hohlraum drive with excellent temperature balance for symmetric inertial confinement fusion capsule implosions," Phys. Rev. Lett **88**, 215004 (2002).

[Cun05a] M.E. Cuneo, E.M. Waisman, W. A. Stygar, G. A. Chandler, R. A. Vesey, E. P. Yu, T. J. Nash, D. E. Bliss, G. R. Bennett, D. B. Sinars, J. L. Porter, W. W. Simpson, L. E. Ruggles, D. F. Wenger, C. J. Garasi, R. A. Aragon, W. E. Fowler, D. Johnson, K. Keller, and J. S. McGurn, "Characteristics and scaling of tungsten-wire-array-z-pinch implosion dynamics at 20 MA," Phys. Rev. **E71**, 046406 (2005).

[Cun05b] M.E. Cuneo, D. B. Sinars, D. E. Bliss, E. M. Waisman, J. L Porter, W. A. Stygar, S. V. Lebedev, J. P. Chittenden, G. S. Sarkisov, and B. B. Afeyan, "Direct experimental evidence for current-transfer mode operation of nested tungsten wire arrays at 16-19 MA," Phys. Rev. Lett. **94**, 225003 (2005).

[Cun06] M.E. Cuneo, D. B. Sinars, E. M. Waisman, D. E. Bliss, W. A. Stygar, R. A. Vesey, R. W. Lemke, I. C. Smith, P. K. Rambo, J. L. Porter, G. A. Chandler, T. J. Nash, M. G. Mazarakis, R. G. Adams, E. P. Yu, K. W. Struve, and T. A. Mehlhorn, "Compact single and nested tungsten-wire-array dynamics at 14-19 MA and applications to inertial confinement fusion," Phys. Plasmas **13**, 056318 (2006).

[Dav97] J. Davis, N. A. Gondarenko, and A. L. Velikovich, "Fast communtation of high current in double wire array Z-pinch loads," Appl. Phys. Lett. **70**, 171 (1997).

[Dee97] C. Deeney, T.J. Nash, R.B. Spielman, J. F. Seaman, G. C. Chandler, K. W. Struve, J. L. Porter, W. A. Stygar, J. S. McGurn, D. O. Jobe, T. L. Gilliland, J. A. Torres, M. F. Vargas, L. E. Ruggles, S. Breeze, R. C. Mock, M. R. Douglas, D. L. Fehl, D. H. McDaniel, M. K. Matzen, "Power enhancement by increasing the initial array radius and wire number of tungsten Z pinches," Phys. Rev. E **56**, 5945 (1997).

[Dee98] C. Deeney, M.R. Douglas, R.B. Spielman, T. J. Nash, D. L. Peterson, P. L'Eplattenier, G. A. Chandler, J. F. Seamen, and K. W. Struve, "Enhancement of X-ray power from a Z-pinch using nested-wire arrays," Phys. Rev. Lett. **81**, 4883 (1998).

[DeM84] L. De Menna, "A z-pinch plasma lens for focusing high-energy particles in an accelerator," Report CERN/PS/84-13 (1984).

[Des99] M. P. Desjarlais and B. M. Marder, "Theory of wire number scaling in wire-array Z pinches," Phys. Plasmas **6**, 2057 (1999).

[Des01] M. P. Desjarlais, "Practical improvements to the Lee-More conductivity near the metal-insulator transition," Contrib. Plasma Phys. **41**, 267 (2001).

[Dus04] P. U. Duselis, J. A. Vaughan, and B. R. Kusse, "Factors affecting energy deposition and expansion in single wire low current experiments," Phys. Plasmas **11**, 4025 (2004).

[Fel81] F. S. Felber and N. Rostoker, "Kink and displacement instabilities in imploding wire arrays," Phys. Fluids **24**, 1049 (1981).

[Fel85] F. S. Felber, M. A. Liberman, and A. L. Velikovich, "Methods for producing ultrahigh magnetic fields," Appl. Phys. Lett. **46**, 1042 (1985).

[Fel88] F. S. Felber, M. M. Malley, F. J. Wessel, M. K. Matzen, M. A. Palmer, R. B. Spielman, M. A. Liberman, and A. L. Velikovich, "Compression of high magnetic fields in a gas-puff Z pinch," Phys. Fluids **31**, 22053 (1988).

[For65] E. B. Forsyth, L. M. Lederman, and J. Sunderland, "The brookhaven-columbina plasma lens," IEEE Trans. Nucl. Sci. 12, 872 (1965).

[Gar04] C. J. Garasi, D. E. Bliss, T. A. Mehlhorn, B. V. Oliver, A. C. Robinson, G. S. Sarkisov, "Multi-dimensional high energy density physics modeling and simulation of wire array Z-pinch physics," Phys. Plasmas **11**, 2729 (2004).

[Gil08] R. M. Gilgenbach, M. R. Gomez, J. Zier, W.W. Tang, D. French, B. W. Hoff, N. Jordan, E. Cruz, Y. Y. Lau, T. Fowler-Guzzardo, J. Meisei, M. G. Mazarakis, M. E. Cuneo, M. D. Johnson, T. A. Mehlhorn, A. A. Kim, V. A. Sinebryukhov"MAIZE: a 1 MA LTD-Driven Z-Pinch at The University of Michigan," 7th International Conference on Dense Z-pinches, Alexandria, Virginin (2008).

[Gom07] M. Gomez, J. Zier, W. Tang, D. M. French, R. M. Gilgenbach, Y. Y. Lau, M. E. Cuneo, M. D. Johnston, M. G. Mazarakis, and T. A. Mehlhorn, "Study of wire contact resistance in single and multi-wire Z-pinch experiments," Bull. Am. Phys. Soc. **52**, no. 16, p. 247 (2007).

[Gom08] M. R. Gomez, J.C. Zier, R.M. Gilgenbach, D. M. French, W. Tang, and Y. Y. Lau, "Effect of soft metal gasket contacts on contact resistance, energy deposition, and plasma expansion profile in a wire array Z pinch," Rev. Sci. Inst. **79**, 093512 (2008).

[Gra00] I.S. Gradshteyn and I.M. Ryzhik, *Table of Integrals, Series, and Products 6th edition* (Academic Press, San Diego, 2000), p.8 and p.45.

[Gri99] D. J. Griffiths, Introduction to Electrodynamics (Prentice-Hall, New Jersey, 1999).

[Hal67] P. M. Hall, "Resistance calculations for thin film patterns," Thin Solid Films **1**, 277 (1967).

[Ham99a] J. H. Hammer, M. Tabak, S. C. Wilks, J. D. Lindl, D. S. Bailey, P. W. Rambo, A. Toor, G. B. Zimmerman, "High yield inertial confinement fusion target design for a z-pinch-driven hohlraum," Phys. Plasmas, **6**, 2129 (1999).

[Ham99b] J.H. Hammer and D. D. Ryutov, "Linear stability of an accelerated current carrying wire array," Phys. Plasmas **6**, 3302 (1999).

[Haw07] M. D. Haworth, Private communications (2007, unpublished).

[Her85] F. Herlach and N. Miura, *Topics in Applied Physics, Vol. 57, Ch. 6* (Springer-Verlag, Berlin 1985).

[Her04] D. W. Hertzog and W. M. Morse, "The Brookhaven muon anomalous magnetic moment experiment," Annual Review of Nuclear and Particle Science, Vol. 54: 141-174 (2004).

[Hil62] F. B. Hilderbrand, *Advanced Calculus for Applications* (Prentice-Hall, New Jersey, 1962), p. 574.

[Hog99] G. E. Hogan, K. J. Adams, K. R. Alrick, et. al., "Proton Radiography," Proceedings of the 1999 Particle Accelerator Conference, Vol. 1, pp. 579-583 (1999).

[Hol67] R. Holm, *Electric Contact*, 4th Edition, (Springer-Verlag, Berlin, 1967).

[Hu05] M. Hu, "Study of linear wire arrays positioned near a return current conductor," Doctoral Dissertation, Cornell University, Ithaca, NY (2005).

[Jan03] Y. H. Jang and J. R. Barber, "Effect of contact statistics on electrical contact resistance," J. Appl. Phys. **94**, 7215 (2003).

[Joh03] M. D. Johnston, Y. Y. Lau, R. M. Gilgenbach, T. S. Strickler, M. C. Jones, M. E. Cuneo, and T. A. Mehlhorn, "Caterpillar structures in single-wire Z-pinch experiments," Appl. Phys. Lett. **83**, 4915 (2003).

[Jon08] M. Jones, "Wire Array Z-pinch Experiments on the Refurbished Z Machine," 7th International Conference on Dense Z-pinches, Alexandria, Virginia (2008).

[Jor07] N. M. Jordan, Y. Y. Lau, D. M. French, R. M. Gilgenbach, and P. Pengvanich, "Electric field and electron orbits near a triple point," *J. Appl. Phys.* **103**, 033301 (2007).

[Ker87] G. I. Kerley, "Theoretical equation of state for aluminum," Int. J. Impact Eng. 5, 441 (1987)

[Kny97] B. A. Knyazev, J. B. Greenly, D. A. Hammer, E. G. Krastelev, and M. E. Cuneo, "Telescopic refractive index gradient diagnostic of an ion diode anode plasma," Tech. Phys. Lett. **23**, 401 (1997).

[Kou00] J. P. Koutchouk, "Principle of a Correction of the Long-Range Beam-Beam Effect in LHK using Electromagnetic Lenses," LHC Project Note 223 (2000).

[Kow91] R. Kowalewicz, M. Lubrano di Scampamorete, S. Milner, J. Christiansen, K. Frank, M. Stetter, and R. Tkotz, "Performance of the CERN plasma lens in laboratory and beam tests at the antiproton source," Proceedings of 1991 IEEE PAC, San Francisco, CA (1991).

[Lau07] Y. Y. Lau, J. W. Luginsland, K. L. Cartwright, and M. D. Haworth, "Role of ions in a crossed-field diode," Phys. Rev. Lett. **98**, 015002 (2007).

[Leb00] S. V. Lebedev, F. N . Beg, S. N. Bland, *et al*., "Effect of core-corona plasma structure on seeding of instabilities in wire array Z pinches," Phys. Rev. Lett. **85**, 98 (2000).

[Leb04] S. V. Lebedev, D. J. Ampleford, S. N. Bland, S. C. Bott, J. P. Chittenden, C. Jennings, M. G. Haines, J. B. A. Plamer, and J. Rapley, "Implosion dynamics of wire array Z-pinches: experiments at Imperial College," Nucl. Fusion **44**, S215 (2004)

[Leb05] S. V. Lebedev, D. J. Ampleford, S. N. Bland, J. P. Chittenden, J. Goyer, C. Jennings, M. G. Haines, G. N. Hall, D. A. Hammer, J. B. A. Palmer, S. A. Pikuz, T. A. Shelkovenko, T. Christoudias, "Physics of wire array Z-pinch implosions: experiments at Imperial College," Plasma Phys. Control. Fusion **44**, A91 (2005).

[Lee84] Y. T. Lee and R. M. Moore, "An electron conductivity model for dense plasmas," Phys. Fluids **27**, 1273 (1984).

[Lev01] L. S. Levine, J. Banister, P. L. Coleman, B. H. Failor, A. Fisher, Y. Song, H. Sze, E. M. Waisman, J. P. Apruzese, J. Davis, D. Mosher, J. W. Thornhill, A. L., Velikovich, B. V. Weber, C. A. Coverdale, C. Deeney, T. Gilliland, J. Mcgurn, R., Spielman, K. Struve, W. Stygar, and D. Bell, "First results for an argon z-pinch at currents above 15 megaamps", IEEE Int. Conf. Plasma Sci., O2F6 (2001).

[Lev02] J. S. Levine, B. H. Failor, H. M. Sze, D. Bell, "Mixed gas Z pinch experiments using a shell-on-shell nozzle on Double-EAGLE," IEEE Trans. Plasmas. Sci. Vol. 30, Issue 2, 512-516.

[Mat97] M. K. Matzen, "Z pinches as intense x-ray sources for high-energy density physics applications," Phys. Plasmas **4**, 1519 (1997).

[Mat05] M.K. Matzen, M.A. Sweeney, R.G. Adams *et al*., "Pulsed-power-driven high energy density physics and inertial confinement fusion research," Phys. Plasmas **12**, 055503 (2005).

[Maz05] M. Mazarakis, C. Deeney, M. Douglas, W. A. Stygar, D. B. Sinars, M. E. Cuneo, J. P. Chittenden, G. A. Chandler, T. J. Nash, K. W. Struve, D. H. McDaniel, "Tungsten wire number dependence of the implosion dynamics at the Z accelerator," Plasma Devices and Operations, Volume 13, Number 2, pp. 157-161 (2005).

[McD02] D. H. McDaniel, M. G. Mazarakis, D. E. Bliss, *et. al*., "The ZR Refurbishment Project," Dense Z-Pinches, AIP Conf. Proceedings **651**, 23 (2002).

[Meh03] T. A. Mehlhorn, J. E. Bailey, G. Bennett, G. A. Chandler, G. Cooper, M. E. Cuneo, I. Golovkin, D. L. Hanson, R. J. Leeper, J. J. MacFarlane, R. C. Mancini, M. K. Matzen, T. J. Nash, C. L. Olson, J. L. Porter, C. L. Ruiz, D. G. Schroen, S. A. Slutz, W. Varnum, and R. A. Vesey, "Recent experimental results on ICF target implosions by Z-pinch radiation sources and their relevance to ICF ignition studies," Plasma Phys. Control Fusion **45**, A325 (2003).

[Mil81] A. R. Miller, Digest of Technical Papers-3rd IEEE Int. Pulsed Power Conf. 200 (1981).

[Mil07] R. Miller, Y. Y. Lau, and J. Booske, "Electric field distribution on knife-edge field emitters," Appl. Phys. Lett. **91**, 074105 (2007).

[Mos73] D. Mosher, S.J. Stephanakis, I.M. Vitkovitsky, "X radiation from high energy density exploded wire discharges," Appl. Phys. Lett **23**, 429 (1973).

[Mos94] D. Mosher, in BEAMS 94, "Pinch spot formation in high atomic number z discharges," Proc. 10th Int'l Conf. High Power Particle Beams, p. 159 (San Diego, CA June 1994). National Technical Information Services, NTIS PB95-144317, PO Box 1425, Springfield, VA 22151.

[Mot97] C. T. Mottershead, J. D. Zumbro, "Magnetic optics for proton radiography," Proceedings of the 1997 Particle Accelerator Conference, Vol. 2, pp. 1397-1399 (1997).

[Nak93] M. Nakamura, "Constriction resistance of conducting spots by the boundary element method," IEEE Trans. Comp., Hybrids Manufact. Technol. **16**, 339 (1993).

[Ols97] R. E. Olson, J. L. Porter, G. A. Chandler *et. al.,* "Inertial confinement fusion ablator physics experiments on Saturn and Nove," Phys. Plasmas **4**, 1818 (1997).

[Par06] M. Park, B. A. Cola, T. Siegmund, J. Xu, M. R. Maschmann, T. S. Fisher, and H. Kim, "Effects of a carbon nanotube layer on electricl contact resistance between copper substrates," Nanotechnolgy **17**, 2294 (2006).

[Pik99] S. A. Pikuz, T. A. Shelkovenko, A. R. Mingaleev, D. A. Hammer, and H. P. Neves, "Density measurements in exploding wire-initiated plasmas using tungsten wires," Phys. Plasmas **6**, 4272 (1999).

[Ppe07] Phongphaeth Pengvanich, "Theory of Injection Locking and Rapid Start-Up of Magnetrons, and the Effects of Manufacturing Errors in Terahertz Traveling Wave Tubes," Doctoral Dissertation, University of Michigan, Ann Arbor (2007).

[Rin99] Joshua I. Rintamaki, "Effects of RF Plasma on the Impedance and Electron Emission Characdteristics of a MV Beam Diode," Doctoral Dissertation, University of Michigan, Ann Arbor (1999).

[Ros56] M.N. Rosenbluth, *Stability of pinch*, Los Alamos Scientific Lab, Report LA-2030 (1956).

[Ros81] A. M. Rosenfeld and R. S. Timsit, "The potential distribution in a constricted cylinder: An exact solution," Quart. Appl. Math. **39,** 405 (1981).

[Rud03] L. I. Rudakov, A. Chuvatin, A L. Velikovich, and J. Davis, "Confinement and compression of magnetic flux by plasma shells," Phys. Plasmas **10**, 4435 (2003).

[Ryu00] D. D. Ryutov, M. S. Derzon, and M. K. Matzen, "The physics of fast Z pinches," Rev. Mod. Phys. **72**, 167 (2000).

[Sam88] A. A. Samokhin, "Stability of symmetrical compression of a cylindrical liner modeling a system of wires," J. Appl. Mech. Tech. Phys. **29**, 243 (1988).

[San96] T.W.L Sanford, G.O. Allshouse, B.M. Marder *et al*., "Improved symmetry greatly increases X-ray power from wire-array Z-pinch," Phys. Rev. Lett. **77**, 5063 (1996).

[San01] T. W. L. Sanford, "Wire number breakthrough for high-power annular z pinches and some characteristics at high wire number," Laser and Particle Beams **19**, 541 (2001).

[San02a] T. W. L. Sanford, N. F. Roderick, R. C. Mock, K. W. Struve, and D. L. Peterson, "Azimuthal structure in wire-array Z pinch Experiments," IEEE Trans. Plasma Sci. **30**, 538 (2002).

[San02b] T. W. L. Sanford, R. W. Lemke, R.C. Mock, G. A. Chandler, R. J. Leeper, C. L. Ruiz, D. L. Peterson, R. E. Chrien, G. C. Idzorek, R. G. Watt, J. P. Chittenden, "Dynamics and characteristics of a 215-eV dynamic hohlraum x-ray source on Z," Phys. Plasmas **9**, 3573 (2002).

[San05] T. W. L. Sanford, R. C. Mock, J. F. Seaman, M. R. Lopez, R. G. Watt, G. C. Idzorek, and D. L. Peterson, "Wire fixturing in high wire-number z pinches critical for high radiation power and reproducibility," Phys. Plasmas **12**, 122701 (2005).

[Shi76] J. Shiloh, A. Fisher, and N. Rostoker, "*Z* pinch of a gas jet", Phys. Rev. Lett. **40**,515 (1976).

[Shi05] D. Shiffler, T. K. Statum, T. W. Hussey, O. Zhou, and P. Mardahl, in *Modern Microwave and Millimeter Wave Power Electronics*, Eds.: R. J. Barker, J. H. Booske, N. C. Luhmann, and G. S. Nusinovich (IEEE Press, Piscataway, NJ, 2005); Ch. 13, p. 691.

[Shu68] F. H. Shu, "The Dynamics and Large Scale Structures of Spiral Galaxies", PhD thesis, Harvard University (1968).

[Sin04] D. B. Sinars, M. E. Cuneo, E. P. Yu, D. E. Bliss, T. J. Nash, J. L. Porter, C. Deeny, M. G. Mazarakis, G. S. Sarkisov, and D. F. Wenger, "Mass-profile and instability growth measurements for 300-wire Z-pinch implosions driven by 14-18 MA," Phys. Rev. Lett., **93**, 145002-1 (2004).

[Sin05] D. B. Sinars, M. E. Cuneo, B. Jones, C. A. Coverdale, T. J. Nash, M. G. Mazarakis, J. L. Porter, C. Deeney, D. F. Wenger, R. G. Adams, E. P. Yu, D. E. Bliss, and G. S. Sarkisov, "Measurements of the mass distribution and instability growth for wire array Z-pinch implosions driven by 14-20 MA," Phys. Plasmas **12**, 056303 (2005).

[Sin07] N. Singer, "Rapid-fire pulse brings Sandia Z method closer to goal of high-yield fusion reactor," retrieved in March 2009 from http://www.sandia.gov/news/resources/releases/2007/rapid-fire-pulse.html.

[Spi89] R. B. Spielman, P. Corcoran, J. Fockler, H. Kishi, P. W. Spence, "A double post-hole vacuum convolute diode for z-pinch experiments on Saturn," Proceeding of the 7th IEEE Pulsed Power Conf., **445** (1989).

[Spi96] R. B. Spielman, G. A. Chandler, C. Deeney, *et. al*.,Bull. Am. Phys. Soc. **41**, 1422 (1996).

[Spi97] R. B. Spielman, C. Deeney, G. A. Chandler, et. al., "PEFA Z: A 60-TV/5-MJ Z-pinch driver," AIP Conference Proceedings **409**, 101 (1997).

[Spi98] R.B. Spielman, C. Deeney, G.A. Chandler *et al*., "Tungsten wire-array Z-pinch experiments at 200 TW and 2 MJ," Phys. Plasmas, **5**, 2105 (1998).

[Spi01] R.B. Spielman, J.S. de Groot, "Z pinches – A historical view," Laser and Particle Beams, vol.19, Issue 04, 509 (2001).

[Str03] T. S. Strickler, R. M. Gilgenbach, M. D. Johnston, and Y. Y. Lau, IEEE Trans. Plasma Sci. **31**, 1384 (2003); also, unpublished (2003).

[Str05] T. S. Strickler, Y. Y. Lau, R. M. Gilgenbach, M. Cuneo, and T. Mehlhorn, "Azimuthal clumping instabilities in a Z-pinch wire array," Phys. of Plasmas **12**, 052701 (2005).

[Str06] T. S. Strickler, "Azimuthal wire motion and ablation dynamics in Z-pinches," Doctoral Dissertation, University of Michigan, Ann Arbor (2006).

[Sty07] W. A. Stygar, M. E. Cuneo, D. I Headley, H. C. Ives, R. J. Leeper, M. G. Mazarakis, C. L. Olson, J. L. Porter, T. C. Wagoner, and J. R. Woodworth, "Architecture of petawatt-class z-pinch accelerators," Phys. Rev. ST Accel. Beams **10**, 030401 (2007).

[Tan06] W. Tang, Y. Y. Lau, T. Strickler, R.M. Gilgenbach, J. Zier, M.R. Gomez, E. Yu, C. Garasi, M.E. Cuneo, and T.A. Mehlhorn, "Current distribution and the azimuthal clumping instabilities in a Z-pinch wire array," Conference Record, 33rd IEEE International Conference on Plasma Science, Traverse City, 2006 (IEEE, Piscataway, 2006), p. 312.

[Tan07] W. Tang, T. S. Strickler, Y. Y. Lau, R. M. Gilgenbach, J. Zier, M. Gomez, E. Yu, C. Garasi, M. E. Cuneo, and T. A. Mehlhorn, "Linear and nonlinear evolution of azimuthal clumping instabilities in a Z-pinch wire array," Phys. Plasmas **14**, 012706 (2007); also, Bull. Am. Phys. Soc. **52**, no. 16, p. 246 (2007).

[Ter99] R.E. Terry, J. Davis, C. Deeney, and A.L. Velikovich, "Current switching and mass interpenetration offer enhanced power from nested array Z pinches," Phys. Rev. Lett. **83**, 4305 (1999).

[Tim99] R. S. Timsit, "Electrical contact resistance: properties of stationary interfaces," IEEE Trans. Components Packaging Tech. **22**, 85 (1999).

[Too64] A. Toomre, "On the gravitational stability of a disk of stars," Astrophys. J. **139**, 1217 (1964).

[Tuc58] J. L. Tuck, "On the Inertial-Electrostatic Confinement of a Plasma," Proceedings of the Second United National Conference on Peaceful Uses of Atomic Energy Vol **32**, p.3 (1958)

[Tur75] G.L. Turner and T.H. Levere, *Maritus van Marum: Life and Work Vol. 4* (Noordhoff International Publishers, 1975).

[Wei07] E. A. Weinbrecht, D. D. Bloomquist, D. H. McDaniel, G. R. McKee, G. L. Donovan, J. W. Weed, T. V. Faturos, D. A. Tabor, and C. Moncayo, "Update of the Z Refurbishment project (ZR) at Sandia National Laboratories," 16th IEEE International Pulsed Power Conference, Vol. 2, pp.975-978 (2007).

[Yu07] E. P. Yu, B. V. Oliver, D. B. Sinars, T. A. Mehlhorn, M. E. Cuneo, P. V. Sasorov, M. G. Hines, and S. V. Lebedev, "Steady-state radiation ablation in the wire-array Z pinch," Phys. Plasmas **14**, 022705 (2007).

[Zie08] J. Zier, M. R. Gomez, D. M. French, R. M. Gilgenbach, Y. Y. Lau, W. W. Tang, M. E. Cuneo, T. A. Mehlhorn, M. D. Johnston, M. G. Mazarakis, "Wire-tension effects of plasma dynamics in a two-wire Z-pinch," IEEE Trans. Plasma Science, Vol. 36, Issue 4, pp. 1284-1285 (2008).